Toward Novel Remote-Center-of-Motion Manipulators and Wearable Hand-Grounded Kinesthetic Haptics for Robot-Assisted Surgery

Sajid Nisar

Abstract

This thesis aims to solve some of the critical limitations affecting kinematic and operational performance of the current surgical robotic and haptic technology by proposing new multi degrees of freedom (DoF) remote-center-of-motion (RCM) mechanisms and hand-grounded haptic devices. The goal is to provide superior kinematic and operational performance than the widely used existing planar surgical manipulators for applications in Robot-Assisted Minimally Invasive Surgery (RMIS). The concept of hand-grounded kinesthetic haptics is being introduced as a means to increase the operator's performance and haptic experience during the robotic teleoperation.

In this thesis, first we explain the need to design new robotic manipulators and haptic devices by highlighting the limitations and challenges faced by the state-of-the-art systems in both, robotic and haptic, domains. To overcome the limitations of existing planar surgical robots, such as, lack of ability to provide a proper tool-entry angle, limited DoFs, and bulkier distal ends, we propose three new surgical manipulator designs that help solve these issues and offer superior performance. To provide a proper tool-entry angle to the patient body in order to reduce the post-operative pain in the patient's skin-tissue, we propose a new surgical manipulator design. Contrary to the widely used manipulators, the proposed design does not need to rely on any extra hardware (referred to as the *pre-surgical setup device*) to perform surgical tasks. We demonstrate the manipulator capabilities by conducting experimental tasks, such as, RCM alignment, pick-and-place, and object manipulation in 3-D.

To address the issue of limited DoFs and heavier distal ends, we propose two novel multi-DoF RCM manipulator designs. The proposed designs achieve the two most important DoFs required for surgery — pitch and translation — through their mechanical design and offer a highly compact distal end. Contrary to the existing designs, the proposed designs do not need to employ extra mechanisms (referred to as the *external means*) to achieve the most-important surgical movement (tool translation), and, thus, offer increased kinematic and operational performance. We also demonstrate the proposed designs' ability to achieve the required workspace for RMIS. To make the manipulators further compatible with the surgical environment, we present an RCM mechanism design that offers same kinematic performance as of the above designs but with a significantly smaller footprint. To ensure maximum kinematic performance inside the required surgical workspace, we have carried out design optimization to determine the smallest possible size of the manipulator mechanism. Compact distal-end and smaller footprint make the proposed designs ideal for applications requiring multiple manipulators to operate in close proximity, such as the RMIS.

To improve the overall surgical performance and operator's experience, provision of intuitive and reliable, i.e. safe, haptic feedback has been a challenge for the past many years.

To solve this problem, in the second half of the thesis, we propose the use of hand-grounded kinesthetic haptics to achieve better wearability and larger workspace. Majority of the existing wearable haptic devices can only provide tactile stimulus only, which may not be sufficient to intuitively perform various surgical tasks, such as, suturing and tissue manipulation. To solve this problem, we propose three different modular designs of a hand-grounded haptic device that can provide kinesthetic feedback for a more compelling and realistic haptic experience. To analyze the potential of using hand-grounded kinesthetic feedback in robotic surgery, we have investigated three different ground locations on the user hand; (i) back of the hand, (ii) proximal phalanx, (iii) and middle phalanx of the index finger, respectively. Each of the devices can provide kinesthetic feedback to the user's index fingertip in two different directions; (a) along the index-finger axis, and (b) along its flexion-extension movement direction. Through experiments, it is shown that the hand-grounded kinesthetic feedback can be efficiently applied to perform surgical tasks such as exploration and stiffness discrimination (palpation). It is further concluded that the choice of a hand-grounding location has profound impact on the user haptic performance and experience. These findings provide important insights about the use of hand-grounded kinesthetic haptics and the role played by different hand-grounding locations on the user haptic perception.

In the last part, we propose a master-slave teleoperation system using the hand-grounded kinesthetic device and the proposed robotic manipulator to achieve superior surgical performance and user experience. Contrary to the existing teleoperation approaches employed in majority of the surgical systems where the control and haptic loops are implemented on same master device, we propose a separation of both loops by making use of wearable haptic device (to provide haptic feedback) and a master manipulator device (to track user-hand position and movement). Using the proposed separation between the control and haptic loops, we intend to circumvent the intrinsic instability issues present in the current surgical systems. Finally, a plan to experimentally evaluate the above proposed teleoperation scheme is discussed. Contributions from the perspective of robotics and haptics, and the subsequent findings as detailed in this thesis, are expected to play an important role to take the current surgical technology a step further where more powerful and safer surgical robots having fully-functional haptic feedback may be realized.

Acknowledgments

My most sincere and heartfelt thank you goes to my advisor, Professor Fumitoshi Matsuno. These last five years, first as a master's degree student and then as a Ph.D. candidate, have been very exciting for me to be part of his research laboratory. I feel tremendously fortunate to have had the opportunity and freedom to discuss my research and ideas with him at great lengths. It is indeed rewarding to have such a supportive, open-heart, and clear-minded mentor with whom to see my degree a finish. I will consider myself lucky to keep on benefiting from his experience and expertise in the years to follow. I hope that we will continue to know each other on ever better terms for the rest of our lives!

During my stay at Stanford University as a visiting Ph.D. scholar, I have had the privilege of working with Prof. Allison M. Okamura. To say the least, her to-the-point discussions and candid opinions have greatly contributed to enhance the depth of haptics-related part of this research. I am highly grateful for her mentorship and encouragement to explore novel ideas. I am also deeply thankful to Asst. Prof. Takahiro Endo; his kind and welcoming attitude always helped me to freely discuss even the weakest points of my research. I hope to keep on benefiting from his being in the coming years as well.

I would also like to thank Prof. Tetsuo Sawaragi and Prof. Masaharu Komori for being part of my defense committee. Their thought-provoking ideas and highly interesting discussions led me to improve this thesis on various places. I feel grateful for their time and support during the review process. I am also thankful to Kyoto University's Inter-Graduate School Program for Sustainable Development and Survivable Societies (GSS) and Japan Society for Promotion of Sciences (JSPS) for granting me their prestigious fellowship awards and extensive research support-funds. I also feel deeply obliged to Prof. Shinji Uemoto and Prof. Kaoru Koike, my GSS secondary supervisors, from Graduate School of Medicine, Kyoto University, for their valuable time and interactive discussions to help me understand the art of performing surgeries.

Finally, I would like to express special gratitude to my parents and family back in Pakistan, as they had to face for several years the agnoy of living without me. Their prayers and continued support certainly made things easier. Doubtlessly, the person to whom I owe most for these years is my wife. She has been a true solace through the thick and thin of life and it were countless hard hours for her to see the kids and manage home at her own. I feel lucky to have her and my charming kids — Ammar, Samara and Musa — whose presence around me completes the life beyond satisfaction.

THIS PAGE INTENTIONALLY LEFT BLANK

Contents

List of Figures

THIS PAGE INTENTIONALLY LEFT BLANK

List of Tables

THIS PAGE INTENTIONALLY LEFT BLANK

Chapter 1

Introduction

Use of robotic manipulators in surgery has made great progress in the last two decades or so. Several surgical manipulators and robotic tools have been designed and invented to assist surgeons in performing a wide variety of surgical interventions. In this regard, a special kind of surgery, called Minimally Invasive Surgery (MIS), has attracted a lot attention from the robotic community due to its highly challenging-to-perform and technical nature. MIS, as described in the following sections, is a highly useful surgical technique. It offers numerous therapeutic and cost related benefits over the traditional open method of performing surgery. Consequently, hundreds of surgical manipulators and robotic tools are being used to perform millions of surgical procedures annually around the globe [1].

However, certain issues and limitations of the current robotic manipulators, underlined in the course of this thesis, have constrained their use, growth, and performance in the field of robotic surgery. To count a few, for example, the current surgical robots partly owing to their traditional designs have limited kinematic and operational performance for the required needs. A specific tool-entry angle required by the surgical needs is difficult to achieve without sacrificing kinematic performance of the robotic manipulator. Their design complexity to achieve the needed surgical tool motions (technically referred to as degrees of freedom or DoFs) makes them extremely costly, and difficult to operate and maintain. More importantly, the current robotic technology lack the availability of fully-functional haptic feedback (sense of touch); the user (surgeon) can not feel the forces and nature of the tissues being operated. This is a well known problem to cause a reduce in the surgical performance.

Several robotic manipulator designs and haptic devices, as will be explained later, have been developed in the recent years to increase the features and performance of the surgical

manipulators. However, there has been a very little progress on the front of providing safe and functional haptic feedback to the user while doing robotic surgery. Similarly, the need of more efficient and powerful robotic manipulator designs, that can offer critical movements (DoFs) required for surgery with superior kinematic performance, is yet in need of address.

The aim of this thesis is to solve the above-mentioned critical limitations of existing surgical robotic and haptic technology for better surgical performance and outcomes. We address the problem of providing a natural tool-entry angle to the patient body by proposing a new manipulator design. We demonstrate that the proposed design achieves the desired tool-entry without compromising the manipulator workspace. To solve superior kinematic and operational performance, we propose two novel multi degrees of freedom (DoF) remote-center-of-motion (RCM) mechanism designs that offer superior kinematic performance than the widely used existing planar surgical manipulators. to increase the operator performance and haptic experience during robot-assisted teleoperation, we propose a hand-grounded kinesthetic device and study its effects on user performance using virtual reality experiments.

In the following sections, we first provide an introduction to the Minimally Invasive Surgery (MIS) and its procedural differences with respect to the traditional open surgery method. We highlight the advantages as well as the challenges posed by it. We explain why and how robotic systems can be useful to overcome these challenges and improve the surgical performance. In the end, we summarize the contribution of this research in solving some of the limitations faced by state-of-the-art robotic surgery systems, from two important aspects; robotics and haptics.

1.1 Minimally Invasive Surgery

Minimally Invasive Surgery (MIS) is a modern surgical technique originated in 1980s. Soon after its advent, it gained immense popularity in surgical community and became widely practiced in the late 90s and early 2000s. As a current practice, Minimally Invasive Surgery (MIS) is considered as a preferred alternative over open surgery both by surgeons and as well as patients. Though not applicable to every existing surgical procedure out there, Minimally Invasive Surgery has been successfully used for a significant number of surgical procedures conceived for various parts and organs of body. A detailed account of its advent, popularity and evolution is given in [2–4].

Minimally Invasive Surgery (MIS), contrary to the centuries-old method of open surgery, is a relatively more technical and innovative way to perform surgeries [5]. It makes use of

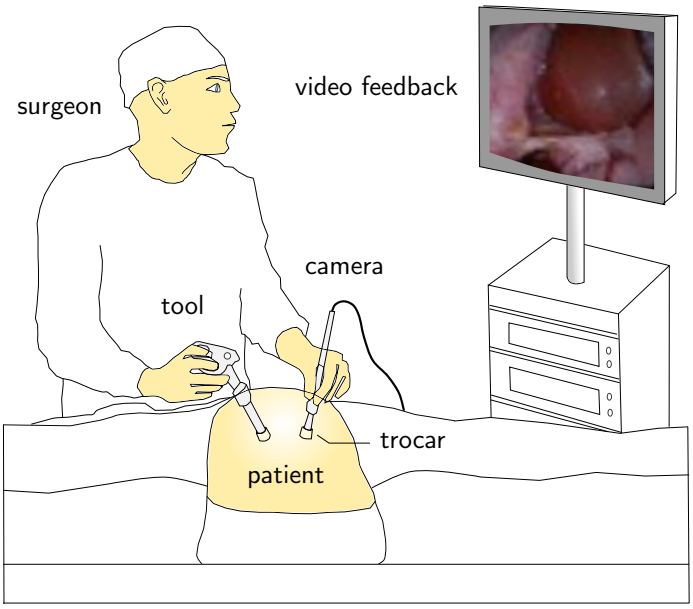

Figure 1-1: Illustration of a typical Minimally Invasive Surgery setup: The surgeon inserts long and thin surgical tool inside the patient body through small holes. The tools are used to operate inside the patient body by viewing the video feedback from an endoscopic camera inside the patient body.

long and thin surgical instruments, which are inserted inside the patient's body by piercing small holes in the outer skin-tissue. These instruments are called laparoscopic tools and their entry-port (hole) in the patient-body is referred to as the *incision*, as shown in Fig. 5-1.

1.2 MIS versus Open Surgery

In a typical open surgery, a larger cut is made in the outer skin tissue to access the internal organs of the body. For example, to operate any organ inside the abdominal cavity, a cut is made in the belly skin tissue. This provides surgeon an opportunity to leverage full control of the natural dexterity of human hand; with all available degrees of freedom (DoFs). However, open surgery often involves cuts to the surrounding tissues, which otherwise are totally unrelated to the surgery itself. These unrelated, yet essential, surgical incisions cause several negative affects. Problems like post-operative pain, therapeutic complications, and extended healing periods are some of the above-mentioned problems.

On the other hand, Minimally Invasive Surgery (MIS) is carried out through very small holes made in the skin tissue. These holes are called as *incisions* and their diameter varies between $5 - 12$mm [1, 6, 7]. In some cases, even bigger incision diameter of 15mm [8] and

beyond is used.

For a typical laparocsopic procedure, three or four surgial tools are inserted inside the body through incisions [7]. The tools, long and slender in shape, are called as *laparascopes*. One of the inserted tools carry an *endoscopic camera* which is used to get video feedback from the surgical site. Based on the video feedback, surgeon operates laparoscopic tools while holding them from the outer side and carries out surgical procedures. Fig. 1-1 illustrates a typical MIS setup. In laparoscopy, the abdominal cavity is filled with a pressurized gas (air, CO_2 or others [9]) in order to inflate the skin tissue for a better visibility. A device, called *trocar*, is used to puncture the outer skin tissue with help of a needle [10] . Other purposes of trocar include to provide a frictionless passage for surgical tools and to prevent gas leakage from the surgical site [11]. During tool insertion and other surgical movements, the surrounding skin tissue remains considerably safe due to the presence of such a cannulation.

1.3 Advantages of MIS

Minimally Invasive Surgery offers a number of advantages over the traditional centuries-old art of 'open surgery'. Less blood-loss, quicker post-operation recovery and shorter bed and hospital stays make it more efficacious and cost effective [1,12–14]. Being minimally invasive in nature, it leaves negligible scars on the body and, thus, offers better cosmetic results. Due to incisions, there remain fewer chances of getting any post-operative complications in outer skin tissues which, otherwise, remains a serious problem in case of open surgery.

Significantly reduced recovery time with Minimally Invasive Surgery procedures proves advantageous on multiple aspects. It reduces post-operative care costs [15–18] and enhances serviceability of medical organizations due to shorter bed-stays. Further details on these and many other MIS advantages can be found in [1, 12–14, 19]. Given its numerous advantages over open surgery, currently Minimally Invasive Surgery is being widely practiced in the operation theaters. Due to its multiple advantages over the open surgery [20], it is being widely practiced in the modern-day operation theaters [21–26].

1.4 Challenges of MIS

With its numerous advantages to the patients, MIS poses various challenges to the surgeons. They find it difficult to perform mainly due to its relatively technical nature. The unintuitive tool movements and the uncomfortable posture required to hold the surgical tools makes it

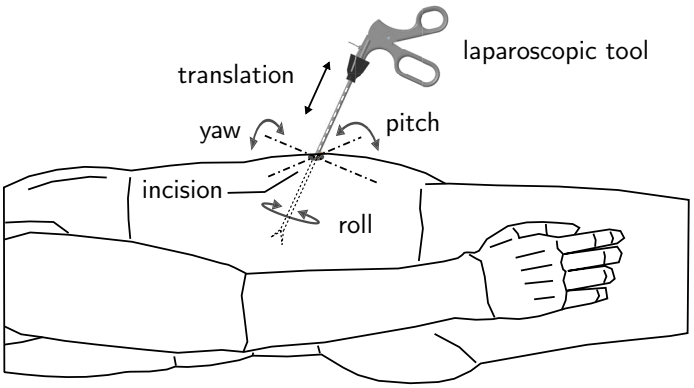

Figure 1-2: Surgical tool setup at the entry (incision) point in MIS: The surgeons are faced with a reduced dexterity, counter intuitive tool movements, and a complete lack of the sense of touch due to the presence of rigid surgical tools.

difficult to perform [27, 28].

The unituitive tool movements [29] are caused by the fact that the surgical tools remain constrained at the *incision* point during the operation. Keeping in view the incison point constraint (Fig. 1-2), the surgeon's hand movement and resulting end-effector movement are opposite in direction. For example, the force on the handle of the tool around the pitch axis in clockwise direction will result a corresponding tool tip movement in counter clockwise direction. Same can be visualized for the yaw degree-of-freedom as well. This is against the natural practice and needs training to familiarize with. Details of these and many other issues and challenges posed by Minimally Invasive Surgery can be found in [1, 15, 30–33].

Fig. 1-2 shows a general tool setup for MIS, specifically for laparoscopic surgery. If the open/close of the end-effector is excluded, a typical Minimally Invasive Surgery procedure (Fig. 1-2) requires four degrees-of-freedom, namely, pitch, yaw, (tool) roll and (tool) translation. Other than that, the surgical tool remains virtually hinged around the incision point during the operation.

Laparoscopic tool can rotate around and translate along the incision point only. From the technical view point, this virtual hing point is called as remote center of motion. Ae explained earlier, this kind of arrangement is not so intuitive for surgeons to operate and, therefore, requires extensively trained people with good surgical skills. Moreover, MIS is a tedious and tiresome technique [34], even for the well-trained and experienced surgeons it offers no easy going. The need to generate a smooth and highly controlled motion of surgical tools inside the patient body definitely takes its toll on the capacity of a surgeon to carry out long procedures.

Contrary to open surgery, the lack of sense of touch in Minimally Invasive Surgery is another big problem for surgeons. It affects their ability to realize the softness/hardness of the tissues under operation. The reason for this is the absence of direct contact between surgeons' hand and the patient tissues. In MIS, surgeons have to operate the surgical tools from outside of the patient's body [35], i.e., remotely. This makes it difficult to feel the nature (stiffness) of the patient tissues and correctly estimate the amount of forces being applied. Another difficulty arises due to the counter-intuitive motion of the surgical tool [29].

Likewise, depth perception becomes weaker in case of Minimally Invasive Surgery. The video feedback is generally 2D, and not sufficient to judge the depth of the surgical tool inside the body. Moreover, the laparoscopic tools have built-in mechanical advantage, which means a smaller force on the handle could result a bigger impact on the end-effectors. To add on that, different kinds of tools have different degree of mechanical advantage. So, it is quite a challenge for surgeons to familiarize themselves with the tools of varying mechanical design and shape.

1.5 Need of Robots?

Given the challenges discussed above, robotic manipulators can be a natural solution to MIS applications. Their precision performance is well demonstrated [36], and use of robotic manipulators have already helped to counter many similar challenges in industrial applications. Robots have better precision and accuracy than a normal human hand. They have high repeatabilty and can produce tremor-free tool motion. Given the tedious nature of MIS, robots become an ideal solution as they do not tire. Robots can significantly improve ergonomic aspects and provide greater control over surgical tool movements. Robots can be used to achieve scaled tool motion and, therefore, perform delicate and sophisticated minimally invasive procedures. Lack of sense of touch can be augmented by the use of haptics. Similarly, the issue of uncontrolled mechanical advanatge can also be solved by the use of surgical manipulators. Due to these very reasons, use of robots for MIS purposes have seen a tremendous growth in the last decade or so [15].

1.6 Problems addressed in this thesis

To help surgeons perform MIS with ease and greater control, robotic manipulators have already been used as a means to increase dexterity and ergonomics. Literature review shows that many of the existing surgical manipulator designs, such as [6, 37–43] are based on a special kind of planar Remote Center of Motion (RCM) mechanisms, called Doubel-Parallelogram (DP) RCM mechanism [44]. This includes the most widely used surgical robot; da Vinci, by the Intuitive Surgical, USA.

We will discuss the limitations and short-comings of the above-mentioned robotic manipulators in relevant chapters during the course of this thesis, however, a brief summary of the critical issues targeted in this thesis is described below. For sake of clarity and easier understanding, the issues affecting the kinematic and operational performance of the current surgical robotic systems, which are addressed in this thesis, pertain to two distinct areas; (1) robotic manipulator design, and (2) haptics.

1.6.1 Related to manipulator design

Tool-entry angle

In MIS, a proper (nearly vertical to the surrounding skin surface) tool entry is desirable to reduce post-operative pain in the skin-tissue. However, majority of the existing planar manipulators, including da Vinci surgical robot, face issues of reduced kinematic performance while doing so for the adversely located tool-entry ports.

Dependence on external means to achieve surgical tool translation

To achieve one of the most critical tool movements required for surgery (tool translation), the existing manipulator designs employ external means, such as, cable-pulleys or actuators mounted directly on the distal end of the manipulator. This affects their operational performance, reduces ability to achieve high forces and torque, and complicates maintenance.

Bulky distal end (manipulator head)

Use of external means described above, in some cases, results in heavier and bulkier distal end. This has adverse affects on the kinematic performance of the manipulator due to increased inertia. This also increase chances of mutual collision between surgical manipulators while performing MIS where multiple manipulators are required to operate in close proximity.

1.6.2 Related to haptic feedback

Lack of compatibility to surgical needs

For better surgical experience and performance, one natural demand for a haptic device is to be wearable. However, majority of the haptic devices that provide superior and compelling haptic (kinesthetic) feedback are either non-wearable or very difficult to donn and doff. This renders them non-compatible to the surgical needs where a more immersive haptic experience is desired.

Instability in the control loop

To have a fully natural haptic experience, the surgical teleoperation system (master and slave manipulators) need to be completely *transparent*. However, there is a well known trade-off between system *transparency* and *stability*. This, in other words, means that in order to realize a fully haptic-enabled experience, one needs to compromise on the system *stability*. This is, however, not possible in the safety-critical applications such as robotic surgery. Consequently, there is no practical surgical robotic system that can offer a functional haptic feedback to increase the surgical performance.

1.7 Contribution of this research

This research has tried to address the critical performance related issues present in the existing robotic and haptic technology, particularly related to the following two important aspects: (i) manipulator design, and (ii) haptics.

1.7.1 Contribution toward novel surgical robot design

To solve the issue of providing a proper tool-entry angle, we have proposed and realized a new surgical manipulator designs which offers a nearly vertical tool-entry even for the adversly located tool-entry ports. To overcome the limitations of existing planar surgical robots, such as, limited DoFs and bulkier distal ends, we have proposed two new mechanism designs that offer the two most important DoFs required for surgery through their mechanical design.

Contrary to the existing designs, they do not need external mechanisms to achieve an important surgical movement (tool translation), and thus, offers increased performance with a compact distal end. We have also demonstrated the proposed design's ability to achieve the required workspace for RMIS. For improved compatibility with the surgical environment,

we have presented another RCM mechanism design that offers same kinematic performance but with significantly smaller footprint. To ensure maximum kinematic performance inside the required surgical workspace, we have carried out design optimization to determine the smallest possible size of the manipulator mechanism. Compact distal-end and smaller footprint make the proposed designs ideal for applications requiring multiple manipulators to operate in close proximity, such as RMIS.

1.7.2 Contribution toward wearable haptics for robot-assisted surgery

To solve the problem of compatibility of haptic devices, we have proposed the use of hand-grounded kinesthetic haptics to achieve better wearability and increased workspace. Majority of the existing wearable haptic devices provide tactile feedback only, which may not be sufficient to intuitively perform a number of surgical tasks, such as, suturing. To solve this problem, we have proposed a hand-grounded haptic device that provides superior haptic (kinesthetic) feedback. These haptic devices are designed to be wearable to make them compatible with the surgical needs and, more importantly, they provide a reliable kinesthetic feedback to the user's fingertip to gain intuitive surgical experience.

As there has been no existing research to evaluate the effects of different hand-grounding locations on user haptic performance and experience, we conducted two user studies to experimentally evaluate the user performance for each of the feedback directions mentioned above. Using virtual reality experiments, it is shown that the hand-grounded kinesthetic feedback can be efficiently applied to perform certain tasks, such as surgical exploration and stiffness discrimination. It is further concluded that the choice of grounding-locations has profound impact on the user haptic performance and experience. These findings provide important insights about the use of hand-grounded haptic feedback and the impact of grounding location on the user haptic experience.

To overcome the problem of control instability, we have proposed a separation between the control and haptic loops; by making use of wearable haptic device (to provide haptic feedback) and a master manipulator device (to track user-hand position and movement). Using this separation between the control and haptic loop, we intend to circumvent the intrinsic instability issues present in the current surgical systems.

1.8 Organization of this thesis

This thesis is organized as follows: In Chap. 2, the background information required to understand the surgical manipulator design, haptic devices and surgical needs is discussed. In Chap. 3, the design of a proposed surgical manipulator, its kinematic analysis and realization is described. It is shown that the proposed design offers a propoer tool-entry angle even for the adversly located tool-entry ports. Chapter 4 describes the design of a 2-DoF planar RCM based surgical manipulator mechanism. Its kinematic analysis and suitability for robotic is carried out. We show that proposed design offers superior kinematic performance than the state-of-the-art 2-DoF designs. Chapter 5 presents an improved design of the 2-DoF RCM manipulator described in previous chapter. The improved design is shown to have significantly smaller footprint and size than the previously proposed design without sacrificing the kinematic performance. Chap. 6 is devoted to the explanation of the hand-grounded haptic device design, its control, and experimental evaluation. Chap. 7 discusses the proposed master-slave teleoperation system and outlines the proposal to circumvent the problem of *instability* in the control loop. Finally, Chap. 8 concludes the thesis.

Chapter 2

Background

Previous chapter gives a brief introduction, advantages and challenges posed by Minimally Invasive Surgery (MIS). We briefly explained the problems addressed and a potential contribution of the research presented in this thesis. In this chapter, we discuss MIS kinematic requirements and other critical factors that play important role to carry out Minimally Invasive Surgery, especially in the case of *Laparoscopy*. This discussion is meant to develop necessary background knowledge in order to understand the problem and solutions proposed in the coming chapters.

2.1 MIS Requirements

As discussed in sec. 1.4, for Minimally Invasive Surgery a surgical tool requires four degrees-of-freedom (DoFs) named as pitch, yaw, translation and roll (shown in Fig. 1-2). Other than that, the surgical tool is hinged over the incision point. It can translate in and out from the incision point but can not make any lateral movement. The incision point constraint can be technically expressed as a combination of pin-and-cylinder joint. Pin joint defines the pitch and yaw motion of the surgical tool, whereas roll and translation degrees-of-freedom can be represented by a cylinder joint. From engineering point of view, this virtual hinge point - center point of incision - is termed as Remote Center of Motion or RCM.

2.1.1 Remote Center of Motion

Remote Center of Motion (RCM) is a fundamental requirement for MIS [1]. RCM is defined as a point around which a mechanism, or a part of a mechanism, rotates. Being not a

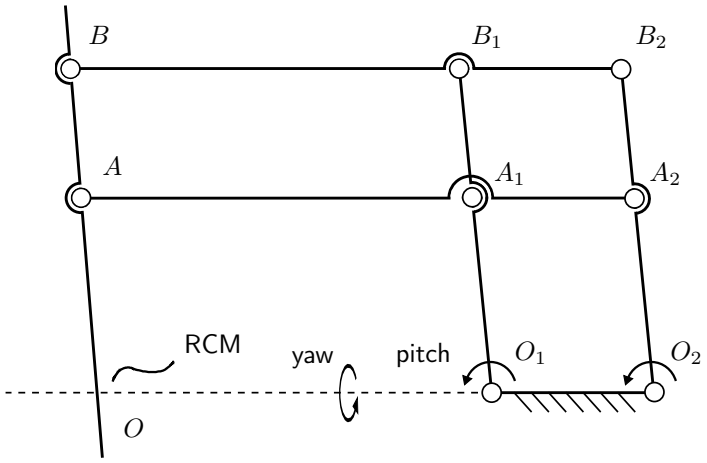

Figure 2-1: A typical and widely-used planar remote center of motion (RCM) mechanism, called double-parallelogram (DP) RCM mechanism. When the mechanism is made to rotate around the joints O_1 and O_2, the point O (RCM) along the distal link remains stationary.

physical part of the mechanism, the point is called remote center of motion. And, the mechanism used to achieve remote center of motion is called RCM mechanism. Fig. 2-1 shows a typical RCM mechanism called Double-parallelogram RCM mechanism. Such a mechanism was first used by [45] and then further explored by Taylor et al. [46, 47]. When joint O_1 or O_2 is actuated, the distal end of mechanism always rotates along the virtual pivot point depicted as RCM. In actual surgery, remote center of motion point coincides with the incision point.

2.1.2 Workspace Requirements

Through *in-vivo* experiments [48, 49] and observations presented in [6, 38], workspace requirements for Minimally Invasive Surgery (mainly *laparoscopy*) have been extracted and summarized. These requirements can be described in terms of tool translation, dexterous workspace and extended dexterous workspace.

Tool Translation

A typical Minimally Invasive Surgery (*laparoscopic*) procedure requires $200 - 220$mm [6] as maximum tool translation below the remote center of motion point inside the patient body. This range of motion largely depends on the physique of a patient and should vary from small to large values for patients with different body sizes and height parameters.

Design presented in [38] has used 300mm for tool translation degree-of-freedom which is quite a big value. However, using a larger value for translation in our case has a direct

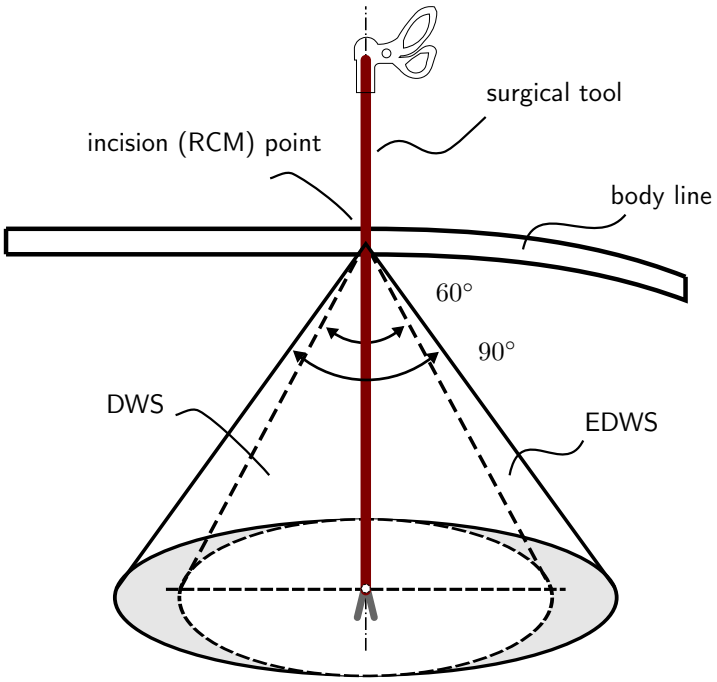

Figure 2-2: MIS workspace requirements: It is determined that the surgical tool covers a conical region inside the patient body. Dexterous Workspace (noted as DWS) denotes the region containing 95% of the surgical tool, where as the Extended Dexterous Workspace (EDWS) bounds the remaining 5% of the surgical tool movements. The depth of the conic regions shows the maximum tool translation required to perform surgical operation.

effect on the overall size of the mechanims. Assuming the fact that the wrist of surgical tool should also help to extend the reach of the manipulator, using translation around 200mm, also used by [6], would be sufficient for design purposes.

Dexterous Workspace (DWS)

Dexterous Workspcace is a high dexterity region defined by a right circular cone with a vertex angel of 60° in which 95% of the total surgical tool motions are contained. This result has been concluded by *in-vivo* experiments [48,49] conducted by 30 different surgeons with different levels of expertise. The dotted conic region in Fig. 2-2 illustrates DWS.

Extended Dexterous Workspace (EDWS)

Similarly, Extended Dexterous Workspace is a conic region with an elliptical cross section created by two orthogonal vertex angels of 60° and 90°. For a minimally invasive surgical procedure, EDWS contains the remaining 5% of surgical tool motions. The region between

the dotted cone and solid cone defines the EDWS (Fig. 2-2).

Total Workspace

Dexterous workspace and extended dexterous workspace together define the total workspace requirement for MIS [49] as shown in Fig. 2-2.

It is clear form the above discussion that remote center of motion (RCM) is essential requirement for Minimally Invasive Surgery. The second important requirement is defined by DWS, which contains roughly the 95% of the surgical tool motion in an MIS procedures. A surgical manipulator designed for MIS should at least meet these two fundamental requirements. The Extended Dexterous Workspace (EDWS) is also part of the total workspace required for MIS. Thus, for any surgical manipulator to be able to offer all the possible surgical tool motions required for a typical surgical procedure, it is important to satisfy the RCM constraint and total workspace requirements.

2.2 Approaches to achieve RCM

Remote center of motion being the critical requirement of Minimally Invasive Surgery has been under consideration for quite some time. Though it has some applications in other fields as well, its applications in surgical field have out numbered all others. To achieve remote center of motion, traditionally there have been two approaches;

2.2.1 RCM through software

In this technique, remote center of motion is achieved through precise control and coupled motion of more than one actuators. Simple serial manipulators use this kind of approach to achieve remote center of motion. A virtual point in the workspace of manipulator is considered as remote center of motion and the manipulator is programmed in such a way that the end-effetor link always pases through that virtual point. Though computaionally more expensive, this approach gives the flexibility to make any point in the workspace as remote center of motion. Given the ease of setting up, this approach needs careful considerations to achieve RCM. If failed due to any reason, the manipulator could lose the RCM which could be highly dangerous for the patient [1]. This is the biggest caveat affiliated with this technique to achieve remote center of motion.

2.2.2 RCM through mechanism

Using this approach, intelligence is incorporated into the mechanism such that it maintains remote center of motion in all situations irrespective of the posture of the mechanism by virtue of its mechanical design. Double-parallelogram mechanism (depicted in Fig. 2-1) is a typical example of this method. This method uses less number of actuators to achieve remote center of motion but requires deep understanding to design at the first place. Contrary to the software approach, in order to maintain the remote center of motion there is no compuation involved. However, remote center of motion achieved by this method is rigid in most cases; it can not be changed within the workspace of the mechanism. Given the inherent safety features and relatively large range of motion, this technique has been the most widely used one in surgical robotics research so far [50]. Further details about the working and various classifications of parallelogram-based RCM mechanisms can be found in [51].

2.3 Planar versus Non-Planar Manipulators

As described earlier, MIS is a difficult surgical technique to perform [34] as it requires highly controlled tool movements inside the patient body [15, 31–33]. To overcome this difficulty, robotic manipulators offer a natural choice as their precision performance is well established [36]. A number of surgical manipulators have been proposed and developed for this purpose [1, 6, 7, 15, 38, 52, 53]. A thorough literature review reveals that the majority of existing surgical manipulators are based on a special kind of mechanisms called *Remote Center of Motion (RCM)* mechanisms. Among these mechanisms, 1 degree-of-freedom (DoF) planar mechanisms have been highly popular for MIS applications [51].

Despite of their many advantages, the planar 1 DoF RCM mechanisms short fall of the number of DoFs required for MIS. This study is primarily aimed at proposing a new planar RCM mechanism in order to overcome the limitations of the traditional 1 DoF double-parallelogram RCM mechanisms. The proposed solution, with all its advantages of existing planar mechanisms, provides the two most important DoFs by virtue of its mechanical design.

In a typical MIS procedure, 4 DoFs are required at the incision point, namely; *pitch*, (tool) *translation*, (tool) *roll* and *yaw*. Also the surgical tool remains virtually hinged at the *incision point* where the only possible motions are a rotation and a translation along the center of the *incision point*. Technically, the incision point is called as the remote center of motion (RCM) [1, 54] which is defined as a point about which a mechanism, or a part of the

mechanism, rotates. Fig. 2-1 shows a typical RCM mechanism called Double-parallelogram RCM mechanism, first used by [45] and then further explored by Taylor et al. [46,47]. When joint O_1 or O_2 is actuated, the distal link of the mechanism rotates along the virtual pivot point (O) depicted as RCM.

For the MIS workspace requirements, measurements presented in [55] show that a region defined by a circular cone with a vertex angel of 60° contains 95% of the total surgical tool motions during a typical MIS procedure. This conic region is named as Dexterous Workspace (DWS). Another conic region with an elliptical base, created by two orthogonal vertex angels of 60° and 90°, is identified as the Extended Dexterous Workspace (EDWS) which contains the remaining 5% of the tool motions. DWS and EDWS together define the total workspace required for the MIS [49] as shown in Fig. 2-2.

Chapter 3

Surgical Manipulator Design & Evaluation

Chapter 2 lays out the necessary foundation and background concepts required to understand the surgical requirements and the use of RCM mechanisms to provide the tool movements required for MIS. In this chapter, we address the problem of providing a proper-tool entry angle to the patient body. First, we explain the importance of a nearly vertical tool-entry angle, with respect to the surrounding skin tissue, to the patient body during the robotic MIS (RMIS). We highlight the problem in the existing traditional robot designs, and propose potential solutions.

We propose a novel RCM based planar manipulator design to solve this problem. We describe the design, perform kinematic analysis to show its ability to achieve RCM and the required workspace. We perform the proposed design evaluation through experiments to show its ability to solve the above-mentioned problem in a experimental setting.

3.1 Problem of a proper tool-entry angle

3.1.1 State-of-the-art Surgical Manipulators

As discussed in Sec. 2.3, majority of the exisiting surgical manipulators make use of planar RCM mechanisms, such as Double-Parallelogram (DP) Mechanism (see Sec. 2.1.1), to accomplish remote center of motion and surgical tool movements. These RCM mechanisms have their particular benefits and suitability for MIS applications that make them being

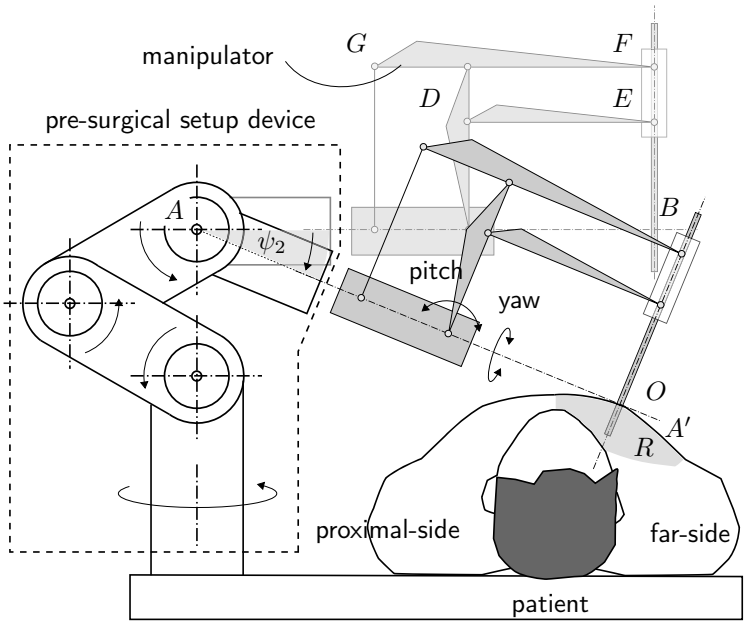

Figure 3-1: An example use of a *pre-surgical setup* device (enclosed with dotted lines) to maintain a proper tool entry-angle. Without such hardware, providing a right-angled tool entry becomes challenging for ports located on the far-side of the patient's body (gray area, marked by R).

widely used in the existing robots. However, the state-of-the-art planar RCM manipulators which are based on these RCM designs, such as da Vinci [5,37], SOFIE [38] and, Silver and Black Falcon [6], do not inherently provide a suitable tool entry-angle, especially when the entry-port is located on the far-side of the patient-body.

3.1.2 Need of a proper tool-entry angle

It is highly desirable that the surgical tool makes a right-angled entry to the patient's body with respect to the surrounding skin-tissue [56], as shown in Fig. 5-1. This helps to avoid causing unnecessary fatigue and post-operative pain—the *parietal pain* [57]—in the nearby tissues. As the abdominal wall mostly features a curvy shape, maintaining a nearly right-angled tool entry becomes challenging for surgical manipulators for certain port locations, e.g., as shown in Fig. 3-1. Moreover, the range of the surgical tool movement—necessary to meet the MIS workspace requirements—should remain available to the operator (surgeon) irrespective of the entry-port location.

The main reason for the existing manipulators' inability to inherently provide a proper tool entry-angle is their DP mechanism design,in which the yaw-axis (AB, Fig. 3-1) always remains parallel to the top-horizontal links (DE and GF). This choice of the yaw-axis does

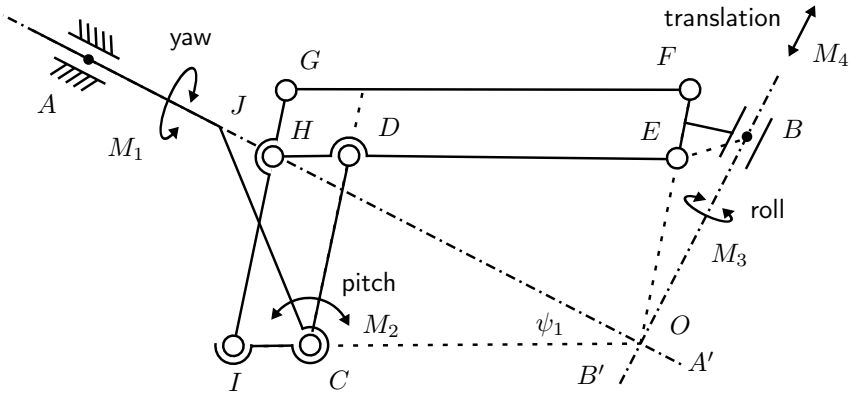

Figure 3-2: Proposed RCM mechanism, with scheme to achieve the basic DoFs required for Minimally Invasive Surgery.

not naturally provide a right-angled tool entry when the entry-port is located on the far-side of the patient's body, as shown in Fig. 3-1. Similarly, the available operating workspace of the manipulator becomes smaller and constrained in certain configurations, e.g., when the tool is inserted from a port located on the far-side of the patient-body [58]. This might be due to the limited availability of the manipulator pitch movement range for such entry-port locations.

3.1.3 Use of the Pre-Surgical Setup Devices

To facilitate a proper tool entry-angle and reach over the surgical site, the above-mentioned manipulators rely on specifically-designed extra hardware, referred to as the *pre-surgical setup* devices [38]. An example scheme depicting use of such an extra-hardware is shown in Fig. 3-1. The da Vinci [37] and SOFIE surgical robots [38] employ similar means to maintain a proper tool entry-angle and reach. Use of this extra hardware adversely affects the size, weight and cost of a surgical system. These devices may also cause occlusion and limit the direct access of the medical staff to the surgical site. Even with this extra hardware, the workspace and performance of a manipulator may decrease for entry-ports located on the far-side of patient-body, as noted by Freschi et al. in case of the da Vinci surgical robot [58].

3.2 Proposed Manipulator Design

To overcome the above-mentioned limitations, we propose a manipulator design that offers—with all advantages of the existing planar RCM-based manipulators—a nearly right-angled tool entry to the surgical site, including ports located on the far-side of the patient-body.

Table 3.1: Comparison of selected features with existing planar surgical manipulators

Name	Manipulator			Instrument	
	Pitch	Yaw	Translation	Actuator-free	Quick-release
SOFIE [38]	70°	180°	300 mm	No	No
Silver Falcon [6]	90°	90°	190 mm	Yes	No
Black Falcon [6]	160°	120°	203 mm	Yes	No
da Vinci*	–	–	–	Yes	Yes
Proposed	170°	180°	300 mm	Yes	Yes

* specifications not available.

The proposed design accomplishes this by modifying the traditional DP mechanism. A tilted yaw link (AJC, Fig. 3-2) is used to provide the desired tool entry-angle by shifting the yaw-axis (AA') location and orientation.

The manipulator also carries an actuator-free and replaceable surgical tool. Being actuator-free means the same actuators (3 in this case) are used to drive different surgical tools at different times. This is desirable to reduce the overall cost of the surgical robotic system. A custom-designed mechanical interface is also proposed that allows rapid change of the surgical tool during robot operation. Given the inherent ability of the manipulator to insert the surgical tool at a proper angle, it does not require a *pre-surgical setup* device to accomplish the desired surgical tasks.

3.2.1 Summary of the kinematic requirements

For a manipulator design to overcome the above-mentioned issues, the kinematic requirements for the MIS are studied. As shown in Fig. 5-1, MIS requires four basic degrees of freedom (DoF) at the incision point; namely pitch, yaw, roll and translation. Another fundamental requirement is that the tool remains virtually hinged at the center of the incision, i.e., there should be no lateral movement at the tool entry-port. From the technical viewpoint, this incision constraint is called Remote Center of Motion (RCM). It is defined as the point about which a mechanical mechanism, or part of that mechanism, rotates [17]. In terms of workspace, Rosen et al. [55] experimentally measured the required workspace for MIS. It is determined to be a conic volume with vertex angle of 90° [49]. A tool translation of 15-30 cm is required inside the patient-body [6,38]. Additionally, it is important to maintain a proper tool entry angle with respect to the surrounding skin-tissue at the entry-port to avoid undue stretch in the skin-tissue.

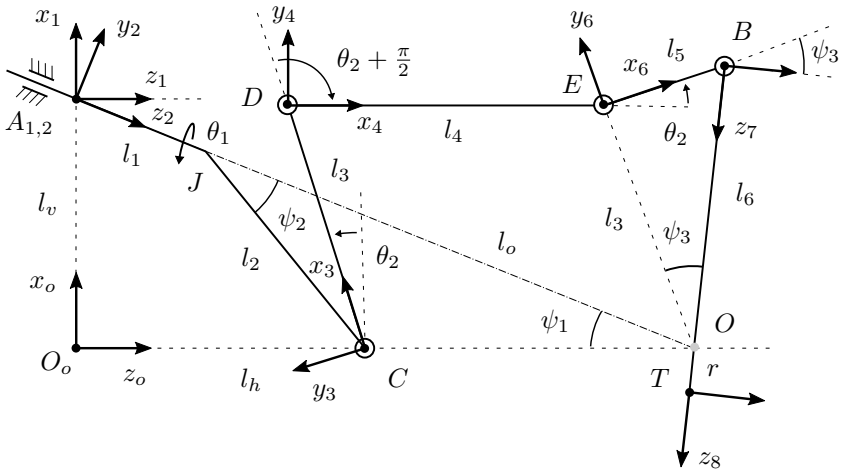

Figure 3-3: A simplified representation of the manipulator. θ_1, θ_2 and r denote the yaw, pitch and tool translation below the RCM point O, respectively.

To provide a proper tool entry-angle without using a dedicated *pre-surgical setup* device, and to ensure the availability of the manipulator workspace for adversely located tool ports, we propose a new manipulator design based on a modified DP RCM mechanism. Three distinctive features of this design are; i) the ability to inherently provide a right-angled tool entry, ii) with a quick-release mechanism for rapid change of the surgical tool, and iii) an actuator-free tool design.

The angular yaw link (AJC in Fig. 3-2) is designed to maintain a proper tool entry-angle through the mechanism design itself. Also, it helps (as described in Sec. 3.2.2) to generate extended movement for links IG and GF by avoiding mutual collision with the base and yaw link. This helps in achieving a larger workspace in the pitch direction compared to the existing planar designs (see Table 3.1), which is important to provide the required workspace for MIS, particularly, for entry-ports located on the far-side of the patient-body. Details of the replaceable surgical tool are described in Sec. 3.7.

3.2.2 RCM Mechanism Design

Figure 3-2 shows the proposed RCM manipulator mechanism in a a scheme to achieve the required DoFs for MIS at the tool entry-port. Yaw link AC rotates around axis AA' through actuator M_1 and generates motion in the yaw direction. While the motion in pitch direction is achieved through the parallelograms of the DP mechanism, using actuator M_2. The surgical tool roll and translation DoFs (motion in and out of the patient-body) are obtained by the actuators M_3 and M_4, respectively. RCM, point O, occurs where the axes

Table 3.2: DH parameters for the simplified representation of the proposed manipulator design

i	α_i	a_i	d_i	θ_i
1	0	l_v	0	0
2	$-\psi_1$	0	0	$\frac{\pi}{2}$
3	$\frac{\pi}{2}$	$l_2 \sin\psi_2$	$l_1 + l_2 \cos\psi_2$	$\theta_1 + \frac{\pi}{2}$
4	0	l_3	0	$\theta_2 + \psi_1 - \pi$
5	0	$l_2 \sin\psi_2 / \sin\psi_1$	0	$-\theta_2 - \frac{\pi}{2}$
6	0	$l_3 \tan\psi_3$	0	θ_2
7	$\frac{\pi}{2}$	0	0	$-\psi_3$
8	0	0	r	0

AA' and BB' intersect each other. It is demonstrated in the sec. 3.3 that the mechanism is capable to maintain the RCM point for the desired working range of the manipulator.

The key difference between the traditional DP Mechanism and the proposed design is the approach to achieve the yaw DoF. In da Vinci, SOFIE and Black Falcon surgical robots, the yaw-axis always remains parallel to the top links, as mentioned earlier. However, in the proposed manipulator, the geometric design of the yaw link makes a slanted yaw-axis, which passes through the RCM point (see Fig. 3-2). The slanted yaw-axis gives two advantages; Firstly, the links responsible for the pitch movement (CD and DE) can exhibit increased range of movement without colliding with the yaw-link. Secondly, it helps to naturally maintain a right-angled tool entry, including the entry-ports located on the far-side of the patient-body.

3.2.3 Kinematics

A simplified representation of the design is shown in Fig. 3-3. Points A, C, D, E, B represent revolute joints with respective joint angles $\theta_1, \theta_2, \theta_2 + \frac{\pi}{2}, \theta_2$ and ψ_3. θ_1 and θ_2 denote the yaw and pitch DoFs, respectively. Tilt angle of the segment AJ with respect to the horizontal axis is represented by ψ_1. Similarly, ψ_2 represents angle of the segment JC with respect to AJ. Here, l_1, l_2 and l_3 are link lengths for segments AJ, JC and CD, respectively. If we consider the universal coordinate system at O_o, link length l_4 for segment DE, l_5 for segment EB, and l_6 for segment BO can be expressed in terms of l_1, l_2 and l_3 through the

relations expressed below.

$$l_v = l_1 \sin(\psi_1) + l_2 \sin(\psi_1 + \psi_2), \tag{3.1}$$

$$l_h = l_1 \cos(\psi_1) + l_2 \cos(\psi_1 + \psi_2), \tag{3.2}$$

$$l_o = \frac{l_v}{\sin(\psi_1)}, \tag{3.3}$$

$$l_4 = l_o \cos(\psi_1) - l_h, \tag{3.4}$$

$$l_5 = l_3 \tan(\psi_3), \tag{3.5}$$

$$l_6 = \frac{l_3}{\cos(\psi_3)}, \tag{3.6}$$

where, l_v is the distance between point O_o and A, l_h is the distance between O_o and C, and l_o represents the distance between A and O. Here, r denotes the tool translation below the RCM point (O), while θ_1 and θ_2 denote the yaw and pitch DoFs, respectively.

Based on the simplified representation given in Fig. 3-3, Denavit-Hartenberg (DH) parameters for the manipulator are determined and presented in Table 3.2. We have followed the classic DH notation described in [59], where i denotes the joint number, α_i represents the twist angle, a_i is the link length, d_i is joint offset, and θ_i represents the respective joint angles. The homogeneous transformation matrix, from the inertial frame O_o to the distal-end tip frame O_8, can be expressed as,

$$^{0}_{8}T = \begin{bmatrix} r_{11} & r_{12} & r_{13} & p_x \\ r_{21} & r_{22} & r_{23} & p_y \\ r_{31} & r_{32} & r_{33} & p_z \\ 0 & 0 & 0 & 1 \end{bmatrix}, \tag{3.7}$$

and its rotation elements are,

$$r_{11} = -s\psi_1 c\beta + s\beta c\psi_1 c\theta_1, \quad r_{12} = -s\theta_1 c\psi_1, \tag{3.8}$$

$$r_{13} = -s\psi_1 s\beta - c\psi_1 c\theta_1 c\beta, \quad r_{21} = s\theta_1 s\beta, \tag{3.9}$$

$$r_{22} = c\theta_1, \quad r_{23} = -s\theta_1 c\beta, \tag{3.10}$$

$$r_{31} = s\psi_1 s\beta c\theta_1 + c\psi_1 c\beta, \quad r_{32} = -s\psi_1 s\theta 1, \tag{3.11}$$

$$r_{33} = -s\psi_1 c\theta_1 + s\beta c\psi_1. \tag{3.12}$$

Here, s and c denote sin and cos functions respectively, and $\beta := \psi_1 - \theta_1 + \theta_2$. p_x, p_y

and p_z represent position of the distal link tip in Cartesian space which is given by,

$$\begin{aligned} p_x = \; & \frac{r}{16 s\psi_1 c\psi_3}(-2s(\psi_1 - \theta_2) - 4s(\psi_1 + \theta_2) \\ & + 2s(3\psi_1 + \theta_1 + \theta_2) - 4s(\psi_1 + \theta_1 - \theta_2) \\ & - 2s(3\psi_1 - 2\psi_3 + \theta_2) - s(3\psi_1 - \theta_1 + \theta_2) \\ & - s(3\psi_1 + \theta_1 + \theta_2) - s(\psi_1 + 2\psi_3 - \theta_1 - \theta_2) \\ & - s(\psi_1 + 2\psi_3 + \theta_1 - \theta_2) - s(3\psi_1 - 2\psi_3 - \theta_1 + \theta_2) \\ & - s(3\psi_1 - 2\psi_3 + \theta_1 + \theta_2), \end{aligned} \tag{3.13}$$

$$p_y = \; - rs\theta_1 c\beta, \tag{3.14}$$

$$\begin{aligned} p_z = \; & l_1 c\psi_1 + l_2 c(\psi_1 + \psi_2) - rs\psi_1 c\theta_1 c\beta \\ & + rs\psi_1 c\beta - rs(\psi_3 - \theta_2) - l_2 \left(\frac{s\psi_2}{s\psi_1} \right). \end{aligned} \tag{3.15}$$

Equations (3.8-3.12) and (5.4-5.6) express the tip orientation and position of the distal link, respectively. This constitutes the forward kinematics of the proposed manipulator design. In Fig. 3-3, p_x, p_y and p_z correspond to the translation, yaw and pitch DoFs respectively.

3.2.4 Velocity Mapping

The distal link tip velocities $(\dot{p}_x, \dot{p}_y, \dot{p}_z)$ are mapped to the joint velocities $(\dot{r}, \dot{\theta}_1, \dot{\theta}_2))$ through the following relation:

$$\begin{bmatrix} \dot{p}_y \\ \dot{p}_z \\ \dot{p}_x \end{bmatrix} = J(\theta_1, \theta_2, r) \begin{bmatrix} \dot{\theta}_1 \\ \dot{\theta}_2 \\ \dot{r} \end{bmatrix}, \tag{3.16}$$

where $J(\theta_1, \theta_2, r)$ represents the Jacobian matrix, which is given as

$$\begin{bmatrix} A & B & C \\ D & E & F \\ \frac{G}{H} & \frac{I}{H} & \frac{J}{H} \end{bmatrix}, \tag{3.17}$$

and its elements are as follows:

$$A = -rc\theta_1 c\beta, \quad B = -rs\theta_1 s\beta \tag{3.18}$$

$$C = -s\theta_1 c\beta, \quad D = rs\psi_1 s\theta_1 c\beta, \quad H = 4s\psi_1 c\psi_3, \tag{3.19}$$

$$E = r(s\psi_1 s\beta c\theta_1 - s\psi_1 s\beta + c(\psi_3 - \theta_2)) \tag{3.20}$$

$$F = -s\psi_1 c\beta c\theta_1 + s\psi_1 c\beta - s(\psi_3 - \theta_2), \tag{3.21}$$

$$\begin{aligned} G = {} & rs\theta_1(s\psi_3 c\beta - s\psi_3 c(2\psi_1 + \beta) \\ & + s(\psi_1 - \theta_2) + s(3\psi_1 + \theta_2)), \end{aligned} \tag{3.22}$$

$$\begin{aligned} I = {} & -r(2c(\psi_1 - \theta_2) - 4c(\psi_1 + \theta_2) + 2c(3\psi_3 + \theta_2) \\ & + c(\theta_1 + \theta_2 - \psi_1) - 4c(\beta - \psi_3) + 2c(\psi_1 + 2\psi_3 - \theta_2) \\ & + c(\psi_1 + \theta_1 - \theta_2) + 2c(3\psi_1 - 2\psi_3 + \theta_2) \\ & - c(3\psi_1 - \theta_1 + \theta_2) + c(\psi_1 + 2\psi_3 - \theta_1 - \theta_2) \\ & + c(\psi_1 + 2\psi_3 + \theta_1 - \theta_2) - c(3\psi_1 - 2\psi_3 - \theta_1 + \theta_2) \\ & - c(3\psi_1 - 2\psi_3 + \theta_1 + \theta_2))/4, \end{aligned} \tag{3.23}$$

$$\begin{aligned} J = {} & (-2s(\psi_1 - \theta_2) - 4s(\psi_1 + \theta_2) + 2s(3\psi_3 + \theta_2) \\ & + s(\theta_1 + \theta_2 - \psi_1) - 4s(\beta - \psi_3) - 2s(\psi_1 + 2\psi_3 - \theta_2) \\ & - s(\psi_1 + \theta_1 - \theta_2) + 2s(3\psi_1 - 2\psi_3 + \theta_2) \\ & - s(3\psi_1 - \theta_1 + \theta_2) - c(\psi_1 + 2\psi_3 - \theta_1 - \theta_2) \\ & - s(\psi_1 + 2\psi_3 + \theta_1 - \theta_2) - s(3\psi_1 - 2\psi_3 - \theta_1 + \theta_2) \\ & - s(3\psi_1 - 2\psi_3 + \theta_1 + \theta_2))/4. \end{aligned} \tag{3.24}$$

3.3 RCM Validation

To ensure the proposed manipulator's ability to maintain a remote center of motion (RCM) for all possible configurations, we make use of the *manipulability* index proposed by Yoshikawa et al. [60]. Manipulability index (w) indicates the 'degree of ease' of the distal-link tip to move in any direction from an arbitrary position inside the manipulator workspace. Higher manipulability index means the tip can move with greater ease (with higher velocity) from that position. A zero value of w means the manipulator is either in a singular configuration or the tip cannot move anymore due to a design constraint, such as the RCM. For

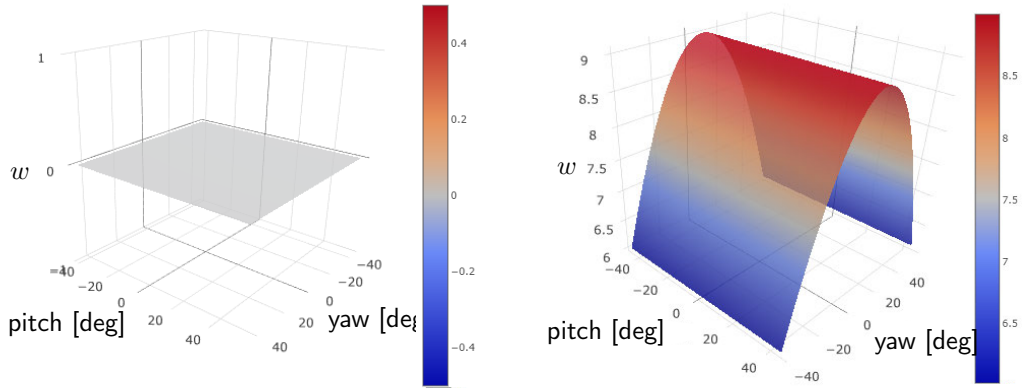

(a) At $r = 0$ [mm] (manipulator tip and the RCM point coincide)

(b) At $r = 3$ [mm] (manipulator tip is below the RCM point)

Figure 3-4: Manipulability index (w) of manipulator over range of joint angles θ_1 (yaw), θ_2 (pitch) and selected values of r (tool translation). At $r = 0$, the manipulator is in virtual singularity due to the RCM constraint.

manipulators, with square Jacobian matrix, manipulability index (w) [60] is expressed as,

$$w = detJ, \quad \geq 0. \tag{3.25}$$

Figure 5-5(a) shows the manipulability index when the distal-link tip coincides precisely with the RCM point. As the relevant joint angles (θ_1, θ_2) change, the tip of the manipulator maintains a zero manipulability, *i.e.*, it does not move away from the RCM point. This means, despite the mechanism being not in a singular configuration physically, actuation in yaw (θ_1) and pitch (θ_2) direction have no effect on the tip position. On the other hand, it becomes evident from Fig. 5-5(b) that when the tip is below the RCM point, the manipulability index of the manipulator maintains a positive non-zero value. Hence, the mechanism possesses RCM constraint for the complete range of the given joint variables. The values of the design constants used in this analysis ($\psi_1 = 20°$, $\psi_2 = 10°$, and $\psi_3 = 20°$) are based on the discussion given in next section.

3.4 Evaluation of the Design Parameters

In this step, we determine the suitable values for the three design constants (ψ_1, ψ_2, ψ_3) and evaluate the effect of joint variables over the performance of the proposed design. It is evident from Fig. (3-4b) that, among the two joint variables θ_1 and θ_2, the kinematic performance is affected only by θ_2. In other words, yaw DoF has no effect over the kinematic performance

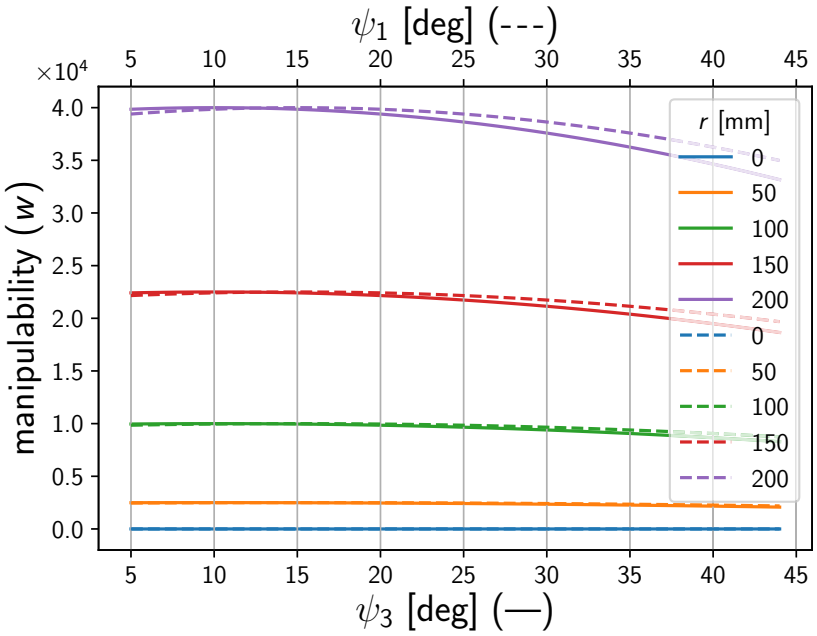

Figure 3-5: Effect of the design constants ψ_1 and ψ_3 over the kinematic performance of the proposed manipulator for various tool translations (r) below the RCM point. The kinematic performance is high for smaller values of the design constants.

as w does not depend on θ_1. On the other hand, the change in w caused by θ_2 is also not significant in terms of value. It is clear that the translation DoF (r) is a key factor to determine kinematic performance of the manipulator. Longer distance of the tool tip below RCM point (larger value of r) would result in increased manipulability and vice-versa.

For the design constants mentioned above, it is obvious from the velocity Jacobian matrix (Eq. 3.16) that ψ_2 has no effect over the manipulator performance. To determine a suitable value for the yaw-axis tilt angle (ψ_1), we plot w for various values of r. In this case, we keep θ_1 and θ_2 fixed such that tip of the distal-link remains at the center of manipulator workspace with respect to the pitch and yaw DoFs. Fig. 3-5 (dotted lines) shows that smaller value of ψ_1 is desirable because it yields relatively higher w index. To achieve this, a value between $10 - 20°$ seems reasonable. Similar procedure is repeated for ψ_3. As both, ψ_1 and ψ_3, affect the manipulability index independently so they are analyzed separately. The current solution considers the entire possible range of both design constants for different values of the tool depth (r) below the RCM point. From Fig. 3-5, it is clear that a smaller value is desirable for ψ_3 (solid lines) as well. Based on the plot, a value between $5 - 20°$ yields higher w index for all values of r.

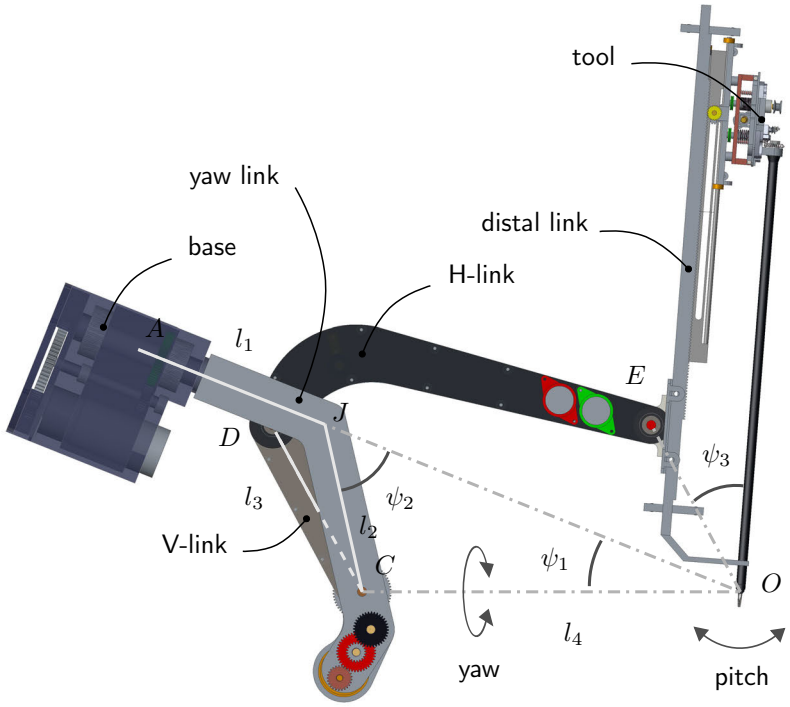

Figure 3-6: CAD model of the proposed design, point O represents the RCM. Yaw-link provides axis (AO) at angle ψ_1 to maintain a right-angled tool entry. The yaw-link and humped design of the H-link jointly help in avoiding mutual link collision, which in turn results in an increased movement in the pitch direction.

3.5 Manipulator Sizing

After determining the relationship between the design parameters and kinematic performance of the manipulator in previous section, we now compute the required link lengths to achieve the desired workspace for surgical application. From the kinematic equations and the geometric relations described in Eqs. (3.1-3.6), it is clear that the link lengths l_4, l_5 and l_6 depend on the chosen values of ψ_1, ψ_2, ψ_3 determined in the previous section. For further simplification, we describe these link lengths in terms of design constants ψ_1, ψ_2, ψ_3 and lengths l_1, l_2, l_3. This representation simplifies the overall problem as three (l_4, l_5, l_6) out of the nine design parameters are eliminated. While the effect of remaining three design parameters (θ_1, θ_2, r) has already been analyzed.

In Fig. 3-6, l_4 represents the distance between the patient and manipulator proximal-end (base). Using relations (3.2-3.4), l_4 can be expressed as

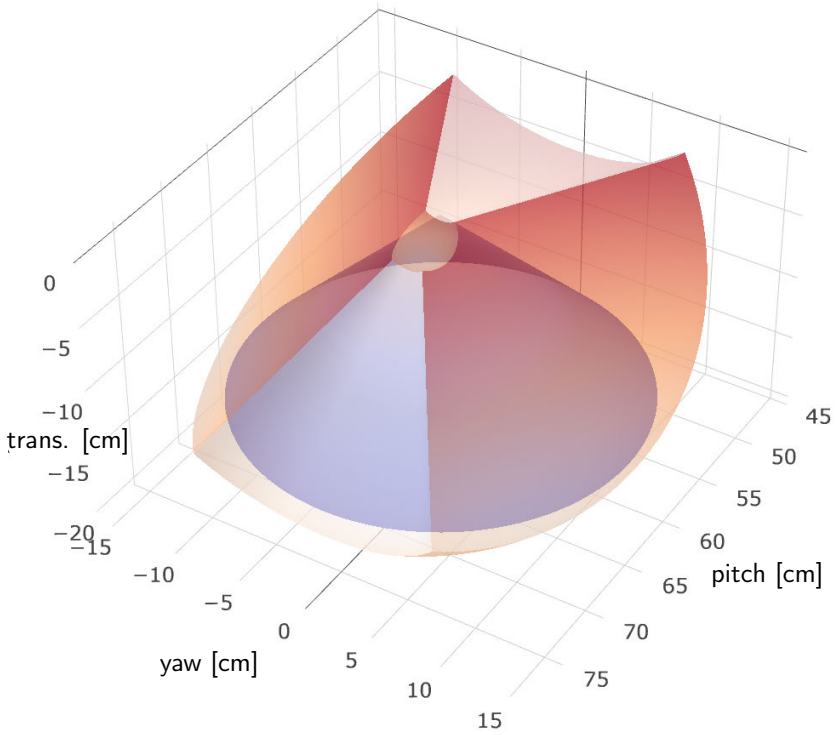

Figure 3-7: Manipulator workspace: translation axis shows the tool position below the RCM point. The conic region depicts the required workspace for MIS. It is evident that the manipulator workspace is larger than the required workspace. Particularly, the increase is significant in the pitch direction which is instrumental in providing sufficient workspace for entry-ports located on the far-side.

$$l_4 = \frac{l_2 \sin(\psi_2)}{\sin(\psi_1)}, \tag{3.26}$$

where, l_2, ψ_1 and ψ_2 are chosen such that l_4 becomes equal to 40 cm. This is a desirable value to have reachability over the surgical site without causing a collision between the manipulator base and the patient's body.

Given the proposed manipulator design, link length l_1 is only significant to drive the yaw link around axis AA'. To provide enough space for the actuators and base unit connection, l_1 is selected as 18 cm. For l_3, a longer length is favorable but it needs to be limited by the extent that the link CD does not collide with the base. Therefore, a link length of 18 cm is determined to be sufficient for this link as well.

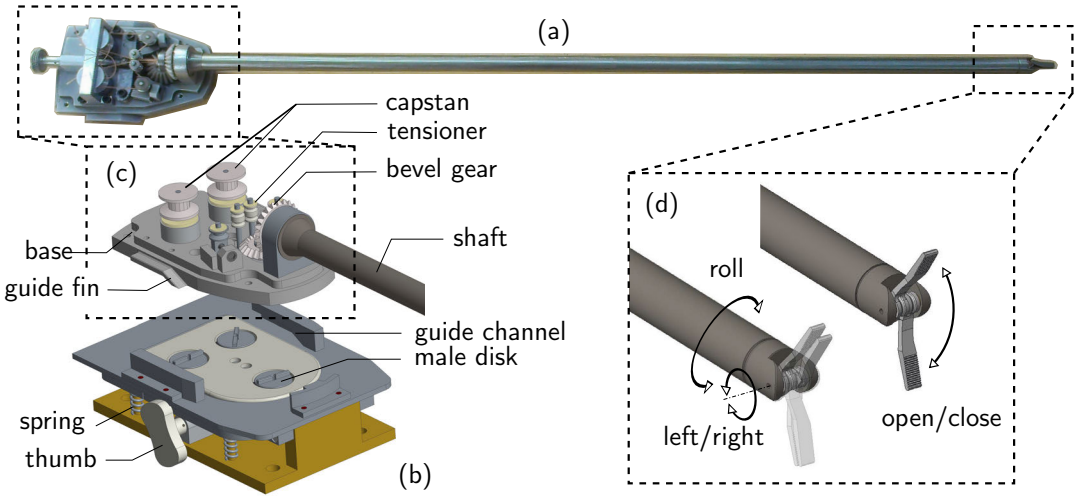

Figure 3-8: Surgical tool and its mechanical interface: (a) Realized prototype (b) Interface unit with quick-release mechanism (c) Tool head (d) Tool tip; exhibiting the three possible movements.

3.6 Manipulator Workspace

The main objective of computing the workspace is to ensure that the manipulator generates enough workspace to satisfy the MIS requirements. Figure 3-7 shows a 3-D representation of the manipulator workspace. We obtain this workspace by setting the joint variables as $\theta_1 \in [-\pi/4, \pi/4] \equiv \Omega_1$, $\theta_2 \in [0, 17\pi/18] \equiv \Omega_2$ and $r = 0.5 - 20$ cm.

Considering the pitch and yaw DoF movements, the manipulator can generate enough workspace for MIS application as it completely covers the conic volume, which represents the required workspace for MIS. It is evident that the manipulator workspace is larger than the required workspace, particularly in the pitch direction. Translation axis shows that a tool depth of 20 cm is achieved below the RCM point, which can be simply increased by using a longer surgical tool. It is important to note that the manipulator workspace does not contain any singularities inside the required workspace region.

3.7 Surgical Tool and Mechanical Interface Design

This section describes the surgical tool design, its mechanical interface for remote actuation, and the quick-release mechanism with the slave manipulator.

3.7.1 Tool Design

The surgical tool is expected to perform basic surgical functions, such as pick-and-place and object manipulation. The tool design process involves consideration of the size, required number of DoFs, ability to be quickly installed/removed, and being actuator-free, i.e., remotely driven. The proposed surgical tool provides three DoFs; roll, left/right and open/close. It consists of a pair of forceps, shown in Fig. 3-8(d), a slender hollow shaft, a base platform to mount the hollow shaft, and a number of idler pulleys to route the actuating cables as shown in Fig. 3-8(c). Both forceps have grooves for the cable passage, and are hinged at the distal-end of the shaft independently. These forceps act as the end-effector of the robotic manipulator. Each limb is actuated independently to provide the human-wrist like articulation for dexterous manipulation. The slender hollow shaft serves as a passage for the cables driving the forceps. The shaft is mounted at the base platform with a bevel gear at the end, shown in Fig. 3-8(c). This gear is meshed with another bevel gear, which is then coupled with the actuator. This provides the roll DoF for the surgical tool end-effector as shown in Fig. 3-8(d).

The base platform also carries two other capstans to drive the forceps. The capstans are then coupled with the actuators through a specialized coupling mechanism. A tensioning mechanism, shown in Fig. 3-8(c), is further added to ensure a smooth and backlash-free movement. The bevel gear and the two capstans mentioned-above are then coupled with three different circular disks, each having an edge-to-edge female rectangular slot . These disks are finally coupled with the actuators through their male counterparts discussed in the tool interface design (Sec. 3.7.2).

To align the surgical tool properly with the driving part, the base platform has fins on both sides. Contrary to the full-body alignment scheme of da Vinci surgical tools, these fins help the tool to easily slide in and out of the guide channels of the adapter, as labeled in Fig. 3-8(c). An actuator-free tool leverages upon the design modularity and reduces the overall cost. As also in the da Vinci robot's Endowrist tools, the actuator-free design enables usage of the same actuators for driving multiple tools at different times. A realized version of the proposed surgical tool is shown in Fig. 3-8(a). As the tool does not carry any electronic components inside, it is easier to transform it into an autoclavable design. Being electronics-free additionally offers safety against electrical hazards, such as current leakage and short-circuiting.

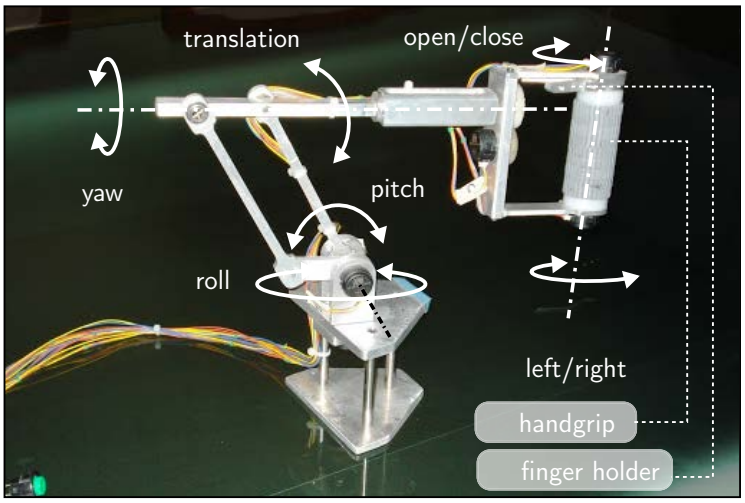

Figure 3-9: The 6-DoF master device used for slave experiments. Finger holders offer independent control of the surgical tool forceps (open/close and left/right) on the slave manipulator.

3.7.2 Tool Interface and the Quick-Release Mechanism

The tool interface mechanism supports two functions; i) remote actuation of the surgical tool, and ii) means to rapidly install and remove the surgical tool during robot operation. It consists of two layers: The top layer ensures the tool alignment and physical connection with the actuator unit. For this purpose, it has guide channels, which direct the tool into its place over the actuator unit. The second layer has a mechanism for the quick-release of the surgical tool as explained below.

As majority of the surgical procedures involve use of multiple surgical tools, it is important to provide easy and rapid change of the tool. For this purpose, a novel quick-release mechanism has been introduced in the proposed design that enables attaching and detaching the surgical tool in a couple of seconds. It consists of an adapter plate, which houses male couplings that in turn engage with the corresponding female counterparts in the tool. The male couplings are driven by the actuators installed behind them. The couplings are pressed by concentric springs, shown in Fig. 3-8(b), to ensure smooth and continuous connection.

Contrary to the da Vinci robot's press-knob mechanism for quick-release of the surgical tool, the proposed interface introduces an independent cam-mechanism that moves the plate, along with the male couplings, up and down. When the cam thumb, shown in Fig. 3-8(b), is rotated, the male coupling parts get disengaged from the female parts. Once the tool is inserted, the male couplings are then released by rotating the thumb again. When actuators are initiated, the attached male couplings engage with the female counterparts on

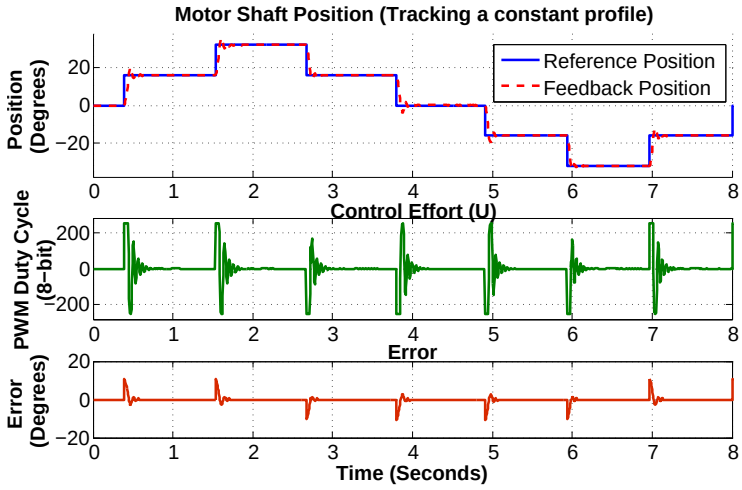

Figure 3-10: Motor shaft tracking the reference position in real-time: It can be noticed that the tracking error is negligible and the controller is highly responsive.

the surgical tool and provide means of a rigid connection.

3.8 Experimental Evaluation

Purpose of this evaluation is to demonstrate the robotic manipulator's ability to i) maintain the RCM, ii) provide a proper tool entry-angle, and iii) to accomplish basic surgical functions such as grasping, transportation and manipulation. For this purpose, we setup a master-slave teleoperation system using a 6-DoF master device, shown in Fig. 3-9. The master manipulator movements are mapped to the slave side, which consists of a 3-DoF slave manipulator, carrying a 3-DoF surgical instrument as its end-effector. For master-slave control, we implemented a Proportional-Integral-Derivative (PID) controller, where position error $e(t)$ is calculated by taking the difference between the motor shaft position $y(t)$ and the reference/commanded position $r(t)$ from the master manipulator. Primary task of the controller is to minimize the error by setting motor input as represented by the control effort U. The error and control law are

$$e(t) = y(t) - r(t), \tag{3.27}$$

$$U = K_P e + K_I \int e dt + K_D \frac{d}{dt} e, \tag{3.28}$$

where, K_P, K_I, and K_D represent the proportional, integral and derivative gains, respec-

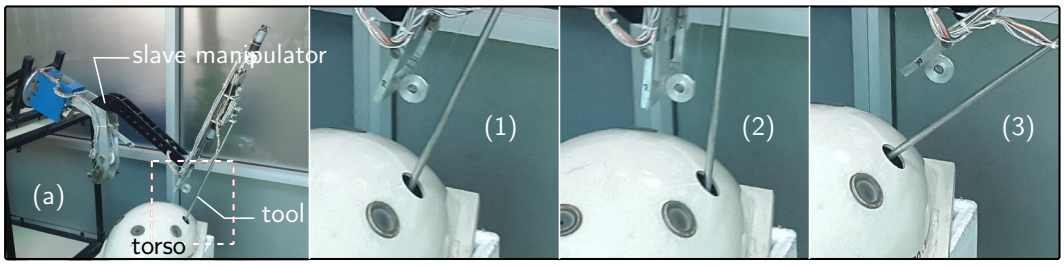

Figure 3-11: Tool-insertion exercise: The tool is inserted into a dummy torso through a port located on the far-side. Figure segments (1), (2) and (3) show that the RCM point and the center of entry-port remain coincident for various slave manipulator configurations.

tively.

Figure 3-10 shows the real-time motor shaft position (red dotted line) tracking the commanded position (blue line) with a staircase profile. The error is negligible as depicted by the orange line, whereas the control effort exerted by the servo drive is shown as the green line. The steady-state position error is observed to be almost 0%. For experimental evaluation, we performed the following tasks such that the user operates the slave robot using the master manipulator device shown in Fig. 3-9.

3.8.1 Performed Tasks

The first task involves insertion of the surgical tool inside a dummy torso such that the RCM point and the center of entry-port remain coincident during the robot operation. The user performs random tool movements through the master manipulator. The aim is to observe whether there occurs any lateral movement at the RCM point. The tool is inserted from the far-side port to observe the tool entry angle and manipulator reach. Fig. 3-11 shows different configurations ((1), (2), (3)) of the slave manipulator while it successfully maintains the RCM point constraint.

In the next task, the user performs pick-and-place operation by controlling the slave robot using the master manipulator. Fig. 3-12 shows the slave manipulator grasping and transporting the rings based on the user action. The rings from distal poles are grasped, transported and then inserted into the corresponding poles on the proximal end of the plate.

The final task requires movement of the slave manipulator along an arbitrary path defined by the metal wire shown in Fig. 3-13. User, using the master manipulator, picks up one ring at a time and transports it to the other end. The intent is to move the ring along the path without coming into contact with the metal wire. Segments (1) and (2) in Fig. 3-13 show the rings being transported from one end of the wire to the other.

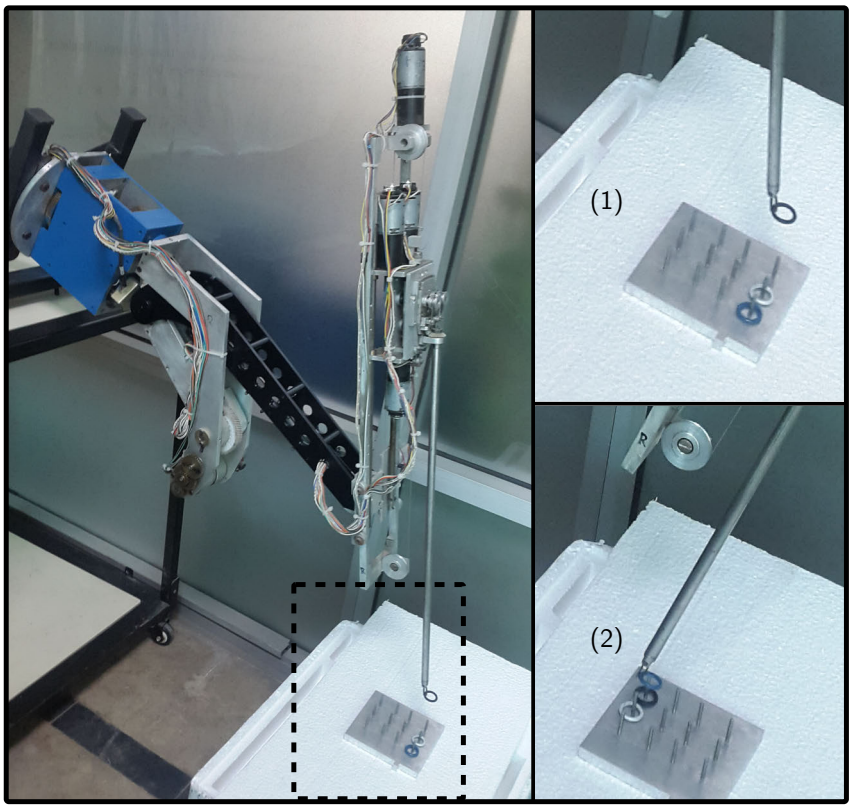

Figure 3-12: Pegs-transfer exercise: The user is asked to transfer the rings one by one, starting from the distal row (1) to the corresponding peg in the proximal row (2).

3.8.2 Discussion

Through the above-mentioned exercises, it is clear that the realized robotic manipulator can successfully perform the basic surgical functions, including the situations with adversely located tool entry-ports. The tool insertion experiment showed that the RCM point remains static (i.e., does not collide with the torso-skin) during the manipulator movement in pitch and yaw directions. It also supports the proposed design idea to provide a proper tool entry-angle through the manipulator design, i.e., without using a *pre-surgical setup* device. Fig. 3-11 shows the proposed design's ability to provide unhindered movement in the pitch direction for the far-side entry-ports.

The pegs-transfer exercise demonstrates that the slave robot is capable to perform basic surgical tasks like grasping and pick-and-place. The zigzag-path exercise shows that the tool can satisfactorily follow a relatively complex trajectory inside the manipulator workspace. These simple tasks were considered to evaluate the performance of proposed manipulator design, tool and its mechanical interface. For a rigorous evaluation, a surgical tool with

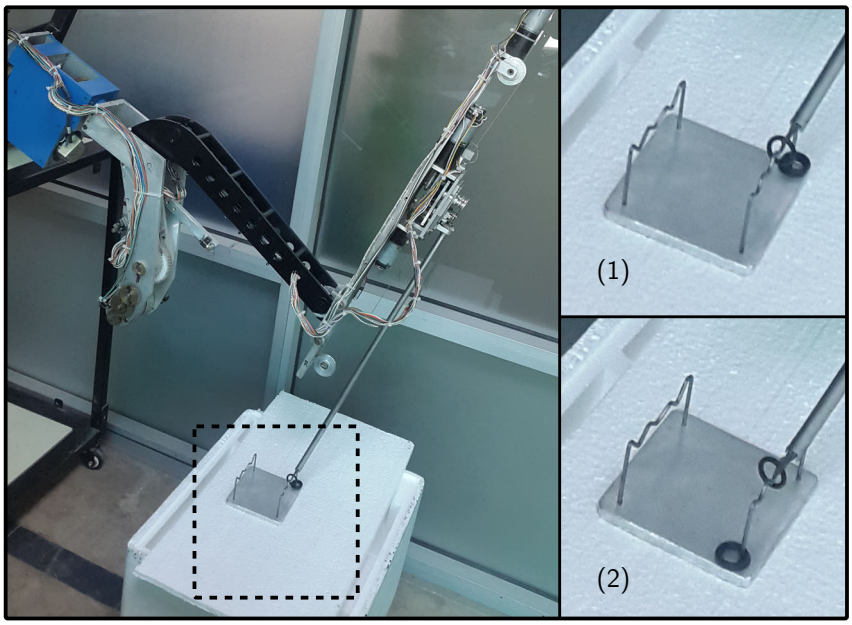

Figure 3-13: Path-following: The user, with the help of master manipulator, grasps and transports the rings—one at a time–from one end to the other. It is desired that the ring should not come into contact with the zigzag wire during the transportation.

increased number of DoFs is needed to carry out more complex tasks like suturing and knot-tying.

3.9 Summary

This paper presented a novel surgical manipulator design and its physical implementation for the MIS application. The manipulator achieves RCM through mechanical means, and provides sufficient workspace and dexterity to accomplish various surgical tasks. Its ability to achieve the RCM constraint is verified. It is demonstrated that the manipulator facilitates tool entry into the patient-body by leveraging its mechanical design, and does not require an external setup device, such as the passive arms used with da Vinci and SOFIE surgical robots. Given the planar nature of its design, the manipulator has minimal footprint in the lateral direction. This is particularly useful for surgical applications where the usage of multiple manipulators in close proximity is a necessity [61].

An actuator-free, modular, and replaceable surgical tool is realized to reduce the over all cost. The electronics-free design of the surgical tool increases prospects of transforming it into an autoclavable design. A mechanical interface, to facilitates easy and rapid change of the surgical tools, is also realized. Ability to quickly replace the tools is highly desirable

for surgical robots as MIS often requires use of more than one surgical tools. A master-slave teleoperation system is setup to demonstrate the basic functions and usefulness of the manipulator for various surgical tasks through experiments. The manipulator has demonstrated the capability to perform all the basic surgical tasks while safely maintaining the RCM.

For a rigorous evaluation, the manipulator performance needs to be further studied using more precise measurement tools, such as the Motion Capture system or optical-tracking based solutions. In the next chapter, we improve the manipulator design to achieve the translation DoF through the RCM mechanism design itself, and realize a 5-DoF surgical tool for advanced surgical tasks like suturing.

THIS PAGE INTENTIONALLY LEFT BLANK

Chapter 4

Multi-DoF RCM Mechanism Design

4.1 Motivation for the New Design

The previous chapter proposed a remote center of motion (RCM) based manipulator design that offers solution to the issue of tool-entry angle to the patient body. However, the proposed design, like the existing traditional RCM designs, can achieve only one of the two important required surgical degrees of freedom (DoFs) through its mechanism design. The other DoF is achieved by making use of *external means*, as described in next section. This choice of *external means* affects the manipulator kinematic and operational performance.

In this chapter, we propose a novel multi-DoF RCM design that achieves both of the important DoFs through its mechanical design. Getting rid of the external means used in previous designs offers enhanced kinematic and operational performance, as described in the course of this chapter.

4.2 Use of *external means* to achieve tool translation

From kinematics view point, MIS requires at least three DoFs (pitch, yaw and translation) at the *incision* point, as shown in Fig. 5-1. Among these, pitch and translation are considered as the most-important DoFs [41] due to a number of reasons. Both DoFs are executed more often than the yaw, and require larger execution forces and higher resolution of the surgical tool movement. Especially, the translation DoF demands highest forces (up to 20N), and

largest travel distance (15–30 cm) [6,38]. By virtue of its location, which forces it to always pass through the incison (RCM point), translation DoF also bears the reaction forces caused by tool operation in other DoFs as well. This makes translation DoF further critical in a surgical manipulator design.

However, the widely used traditional planar RCM mechanisms, including the DP mechanism of the da Vinci surgical robot, offer only one degree of freedom (DoF) — pitch — purely through their mechanism design [41]. The other important DoF — translation — is often realized by installing some *external means*, such as cable-pulleys or actuators directly mounted on the distal-end of a manipulator [41]. In case of da Vinci surgical robot, for example, the translation DoF is implemented using a complex web of cables and pulleys. These cables run from the proximal-end (base) right up to the distal-end of the manipulator [37]. In other designs, such as [7, 38], it is realized by mounting actuators directly on the distal-end of manipulator. In both design approaches, the pitch DoF is achieved through RCM mechanism, but the translation DoF is realized using one of the *external means* mentioned above.

Use of these *external means* to realize translation DoF has several negative effects on the manipulator performance. It increases the design complexity, and (depending on the nature of external means used) may affect the overall compactness of the distal-end. For example, use of cable-pulley scheme complicates the overall design and reduces the operational life of a manipulator. It also increases the joint friction and makes it challenging to maintain an appropriate tension in the metallic cables for longer operational periods. Use of cable-pulley scheme also decreases the power transmission capabilities of the robot [62]. On the other hand, actuators mounted directly on the distal-end increase its size and weight. This consequently increases the torque and energy requirements of a surgcial manipulator. A heavier distal end could easily induce vibrations at the tool tip.

4.3 Problem with the existing traditional manipulators

MIS requires 4 DoFs (*pitch, translation, yaw and roll*) but the existing planar RCM mechanisms, like the double-parallelogram mechanism, only provide 1 DoF (*pitch*). The remaining three DoFs are achieved through *external means*. For example, *yaw* is obtained by tilting the mechanism along its base link (Fig. 4-1), as is the case with [37,38,50]. *Roll* and *translation* are usually achieved by mounting actuators directly on the distal-end of the manipulator as suggested by [38, 50]. The *roll* DoF demands less precision and is relatively easier to

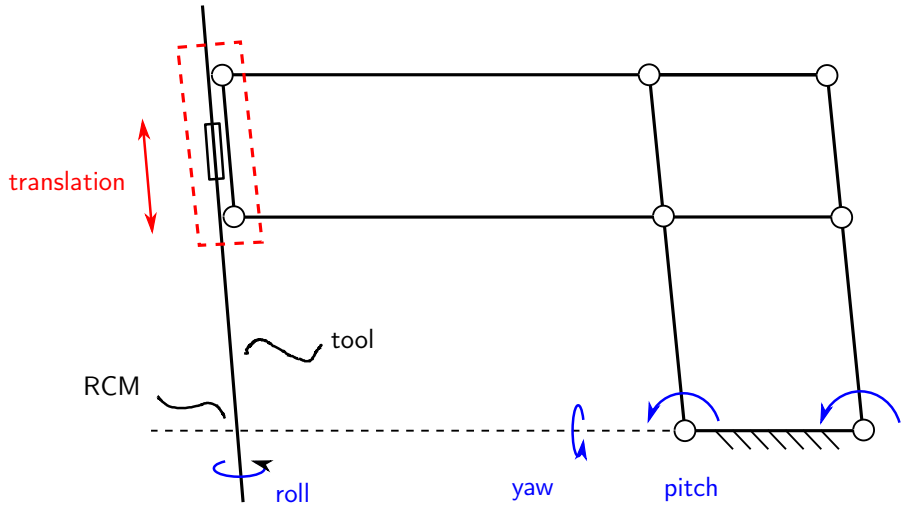

Figure 4-1: A double-parallelogram RCM mechanism

implement. However, the *translation* DoF when implemented using such *external means* causes several performance issues as described below.

The purpose of translation DoF is to facilitate the inward and outward movement of the surgical tool through the incision point. Traditionally, there have been two approaches to implement *translation* DoF in planar RCM mechanisms;

4.3.1 Distal-end Actuators

In this approach, actuators are directly mounted on the distal-end of the manipulator to generate *translation* DoF. Examples of such implementation include Al-Zahrawi Surgical Robot [7] and SOFIE Surgical System [38]. This approach has better power transmission capabilities, but placement of actuators over distal-end makes it bulkier [1] and induces unnecessary vibrations at the tool tip. It also increases inertia of the distal-end which, consequently, increases torque and energy requirements. To avoid these issues, prismatic actuators can be an easy choice to implement *translation*. However, they are relatively expensive and affect the backdrivability of the manipulator [39].

4.3.2 Cable-Pulley Scheme

A typical example of such an implmentation of *translation* DoF is da Vinci Surgical Robot [37]. Using this approach, actuators are installed closer to the base of manipulator and the end-effector is translated through custom-designed steel cables and pulleys. This scheme helps to acheive compact distal-end but is relatively complex to implement. It also affects

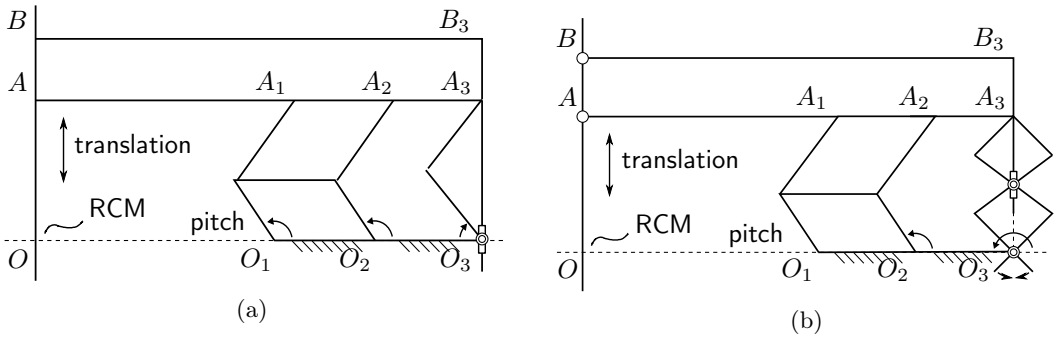

Figure 4-2: Trivial forms of the proposed 2 degrees-of-freedom RCM mechanism

the power transmission capabilities due to a more significant friction factor [1]. Moreover, the cables tend to elongate after a certain period of use and require replacement. This affects the operational cost and performance of the manipulator.

Given the two approaches, it is evident that the implementation of *translation* DoF through *external means* has a number of downsides. Therefore, it is desirable to find a solution which could provide the two most important DoFs, *pitch* and *translation*, independent of any such *external means*.

4.4 State-of-the-art multi-DoF planar RCM designs

In the exisiting literarture, we could find only two studies aimed at solving the limitations of 1 DoF planar RCM mechanism, though indirectly. One by Li *et al.* [39] and another by Gijbels *et al.* [50]. The mechanism proposed by Li *et al.* provides 2 DoFs - *pitch* and *translation* - and is backdrivable as well. However, pertaining to the link length ratios required for RCM constraint the size of the mechanism becomes larger. This increases the risk of mutual collision between the manipulators when working in close-proximity [39] such as in MIS. Moreover, the weight of whole mechanism is supported by only two links and the static stability is not taken into account.

The mechanism proposed by Gijbels *et al.* also provides *pitch* and *translation* DoFs and is statically stable with actuators in energized state. However, the limited tool translation (about 30mm) affects its suitability for MIS procedures like Laparoscopy. The mechanism carries a translating downward protruding link towards the patient-side which could pose a potential unwanted interference risk with the surgical site. It also has a number of links towards the distal-end supported by only one cantilevered-link. This could induce unnecessary vibrations in the tool tip for a larger manipulator, such as intended for Laparoscopic

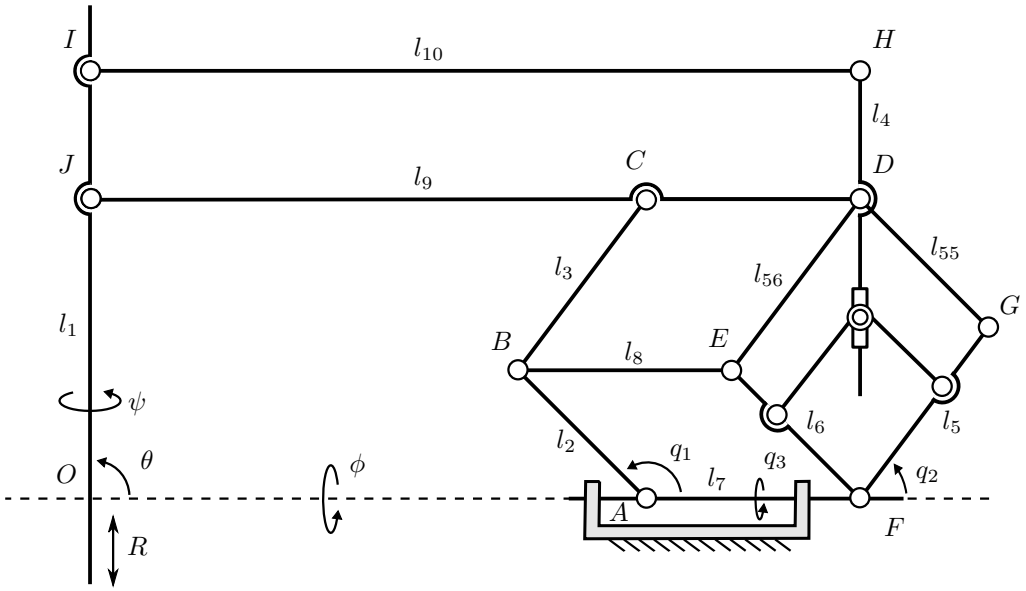

Figure 4-3: The proposed 2-DoF mechanism with RCM at point O. When actuated using M_1 and M_2 at proximal end, pitch (θ) and translation (R) DoFs are achieved at the distal end. Similarly, yaw (ϕ) DoF is obtained by tilting the mechanism along base link AF.

applications.

4.5 Proposed 2-DoF RCM Mechanism

To solve the problems induced by *external means* in 1 DoF RCM mechanisms and to avoid the downsides present in the existing 2 DoFs RCM mechanisms, we propose a new RCM mechanism which is planar and provides the two most important DoFs by virtue of its mechanical design, *i.e.* without any *external means*. The mechanism design, its ability to maintain RCM constraint, kinematics, workspace and singularities are explained below.

Based on the concept of double-parallelogram RCM mechanism, we construct various trivial forms of the mechanism capable of providing *pitch* and *translation* DoFs. Fig. 4-2 shows a couple of such trivial forms. These trivial forms are able to achieve RCM, but they lack in one or another aspect. For example, the mechanism shown in Fig. 4-2(a) is statically not stable which means it can not hold its posture independently. It requires more actuators to function properly than the number of DoFs produced. Similarly, the mechanism shown in Fig. 4-2(b) is statically stable but involves many redundant links which has its own downsides for practical purposes.

If we take a collective look over these trivial mechanisms, a minimalist version of the

RCM mechanism can be envisaged as shown in Fig. 4-3. M_1 and M_2 represent the two actuators to achieve *pitch* and *translation* DoFs while A_3 represents a a passive prismatic joint. If M_1 and M_2 are actuated in same direction (clockwise or counter clockwise), *pitch* motion is produced. When both are moved in opposite direction to each other, *translation* DoF is achieved. A similar actuation scheme is present in [50].

The proposed mechanism provides the two most important DoFs without using any *external means*. It does not have any downward protruding link contrary to the mechanism in [50]. Moreover, the number of linkages and joints in the proposed mechanism are fewer than the solution proposed in [39].

4.5.1 Mechanism Kinematics

Due to interconnected parallelograms, the effect of M_1 remains same whether it actuates link O_1E or O_2E_1 (Fig. 4-3). Also to achieve RCM, segments OA and A_3B_2 remain parallel to each other. Based on this, a simplified representation of the mechanism is shown in Fig. 4-4 where O is the RCM point. q_1, q_2 and q_3 are the joint variables and θ, ϕ and R represent the *pitch*, *yaw* and *translation* DoFs, respectively.

The position of point A_1 in Cartesian space can be expressed as $x = l_2\cos(q_1)+l_3\cos(q_2)$ and $y = l_2\sin(q_1)+l_3\sin(q_2)$, where l_2 and l_3 are lengths of link AB and BC, respectively. As $\overline{OA} \parallel \overline{O_1A_1}$ and $\angle AOO_1 = \angle XO_1A_1$ are in virtual parallelogram OO_1A_1A, the *pitch* (θ) can be expressed as,

$$\theta = \tan^{-1}\left(\frac{l_2\sin(q_1)+l_3\sin(q_2)}{l_2\cos(q_1)+l_3\cos(q_2)}\right). \tag{4.1}$$

Translation (R) DoF represents the length of distal link below the RCM point. From Fig. 4-4, $R = l_1 - |\overline{O_1A_1}| = l_1 - |\vec{r}|$, where l_1 is length of the distal-link.

$$R = l_1 - \sqrt{l_2^2 + 2l_2l_3\cos(q_1-q_2)+l_3^2}. \tag{4.2}$$

Yaw (ϕ) is achieved by mounting actuator along the axis OO_1 and can be simply given by $\phi = q_3$. Based on the kinematic equations, a relation between the joint velocities and the distal-link tip velocities can be expressed as,

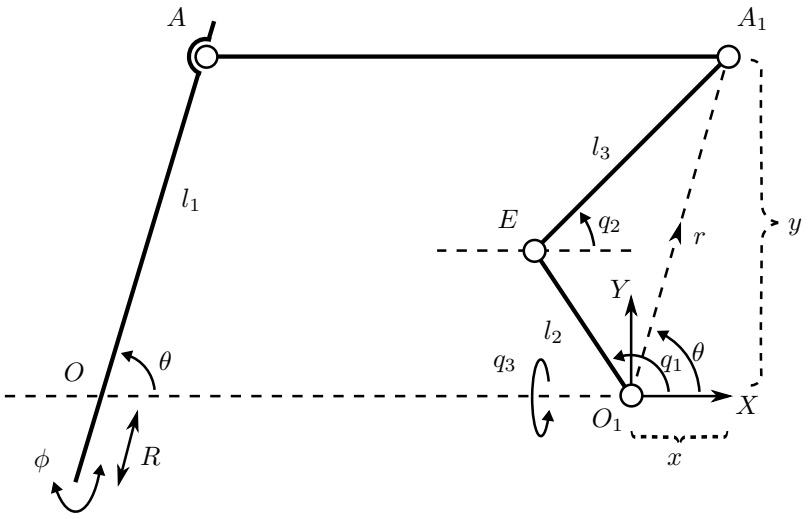

Figure 4-4: A simplified representation of the proposed RCM mechanism

$$\begin{bmatrix} \dot{R} \\ \dot{\theta} \\ \dot{\phi} \end{bmatrix} = J(q) \begin{bmatrix} \dot{q_1} \\ \dot{q_2} \\ \dot{q_3} \end{bmatrix}, \quad J(q) = \begin{bmatrix} \frac{A}{\sqrt{E}} & \frac{B}{\sqrt{E}} & 0 \\ \frac{C}{\sqrt{E}} & \frac{D}{\sqrt{E}} & 0 \\ 0 & 0 & 1 \end{bmatrix}, \tag{4.3}$$

where a dot represents time derivative and $J(q)$ is the Jacobian matrix with elements,

$$A = l_2 l_3 \sin(q_1 - q_2),\ B = -l_2 l_3 \sin(q_1 - q_2),$$
$$C = l_2 l_3 \cos(q_1 - q_2) + (l_2)^2,\ D = l_2 l_3 \cos(q_1 - q_2) + (l_3)^2,$$
$$E = (l_2 \cos q_1 + l_3 \cos q_2)^2 + (l_2 \sin q_1 + l_3 \sin q_2)^2.$$

Alignment Mechanism

To achieve RCM, it is vital for the points O_2, A_3, A_2, B_2 (Fig. 4-3) to remain collinear with each other. It is important to note that the link B_2A_4 in quadrilateral $O_2E_1A_2G_1$ is not physically constrained at point O_2. Therefore, there is a possibility to lose the collinearity, and consequently the RCM. To avoid this, the mechanism portion represented by quadrilateral $O_2E_1A_2G_1$ (Fig. 4-5), named as *alignment mechanism*, is solved to ensure collinearity.

Let us define $r_1 = \vec{O_2A_2}$, $r_2 = \vec{O_2A_3}$ and $l_5 = \overline{O_2G_1}$, $l_6 = \overline{O_2E_1}$, $k_5 l_5 = \overline{O_2G_2}$,

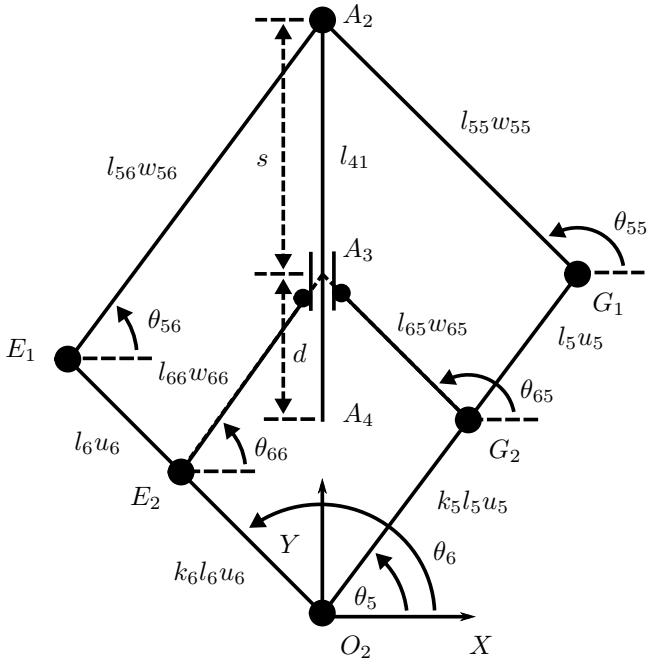

Figure 4-5: The alignment mechanism to maintain the remote center of motion constraint. A_3 is a passive prismatic joint.

$k_6l_6 = \overline{O_2E_2}$, $l_{55} = \overline{G_1A_2}$, $l_{56} = \overline{E_1A_2}$, $l_{65} = \overline{G_2A_3}$, $l_{66} = \overline{E_2A_3}$, $u_i = [\cos\theta_i \ \sin\theta_i]^T$, $w_{ji} = [\cos\theta_{ji} \ \sin\theta_{ji}]^T$, $(i = 5, 6, j = 5, 6)$ where $\theta_i, \theta_{ii}, (i = 5, 6)$ denote the corresponding angles. A set of sufficient conditions for the collinearity of points O_2, A_3, A_2 is determined (Appendix A) as,

$$k = k_5 = k_6, \quad (0 < k < 1), \tag{4.4}$$

$$k^2(l_{55}^2 - l_{56}^2) = l_{65}^2 - l_{66}^2. \tag{4.5}$$

To maintain the geometric symmetry of the mechanism, we further assume that $l_5 = l_{56}$, $l_6 = l_{55}$, $k_5l_5 = l_{66}$ and $k_6l_6 = l_{65}$. Using $k = k_5 = k_6$, (4.5) holds true with these assumptions. For *alignment mechanism* (Fig. 4-5) the above assumptions mean that the quadrilaterals $O_2E_1A_2G_1$ and $O_2E_2A_3G_2$ are essentially two parallelograms such that,

$$\theta_5 = \theta_{56} = \theta_{66}, \tag{4.6}$$

$$\theta_6 = \theta_{55} = \theta_{65}. \tag{4.7}$$

After ensuring the collinearity, it is important to restrict the motion of A_2A_4 inside

the geometric boundary of the *alignment mechanism*. From Fig. 4-5 if $d = l_{41} - s$ where $l_{41} = |\overline{A_2A_4}|$, then s can be written as $s = |\vec{r_1}| - |\vec{r_2}|$. Based on the above assumptions and their subsequent results expressed in (4.6) and (4.7), s can be further written as,

$$\begin{aligned} s &= \sqrt{l_5^2 + l_6^2 + 2l_5l_6\cos(\theta_6 - \theta_5)} \\ &\quad - \sqrt{k^2l_5^2 + k_6l_6^2 + 2k^2l_5l_6\cos(\theta_6 - \theta_5)}, \qquad (4.8) \\ s &= (1-k)|\vec{r_1}|. \qquad (4.9) \end{aligned}$$

Therefore, the condition to restrict the motion of the link segment l_{41} inside the geometric boundary of the mechanism is determined as,

$$0 < l_{41} - ((1-k)|\vec{r_1}|) < |\vec{r_2}|. \qquad (4.10)$$

4.5.2 Singular Configurations

To ascertain the suitability of the mechanism for its intended application, it is important to examine its singularities. To find singular configurations of the proposed RCM mechanism, $\det|J(q)|$ is solved against zero. From (4.3),

$$\texttt{det}J(q) = \left| \frac{l_2l_3\sin(q_1 - q_2)}{\sqrt{l_2^2 + 2l_2l_3\cos(q_1 - q_2) + l_3^2}} \right| = 0. \qquad (4.11)$$

This means that the mechanism gets into singular configuration when $\{(q_1, q_2)|q_1 = q_2, q_1 = q_2 \pm \pi\}$. Geometrically, these singularities correspond to the mechanism configurations when parallelogram $O_1EE_1O_2$ and $EA_1A_2E_1$ become aligned or the link O_1E and EA_1 become parallel to each other (Fig. 4-3).

4.5.3 Optimal Configuration

Optimal configuration relates to the mechanism configuration when the tip of end-effector achieves a maximum possible velocity in any arbitrary direction from a given point inside its workspace.

For mechanisms with square Jacobian matrix, the *manipulability* is defined as $w = \texttt{det}J(q), w \geq 0$ [60]. From (4.11) the manipulability measure (w) becomes maximum when $q_1 = q_2 + (\pi/2)$.

Geometrically, it means when links O_1E and EA_1 will be at right angle to each other,

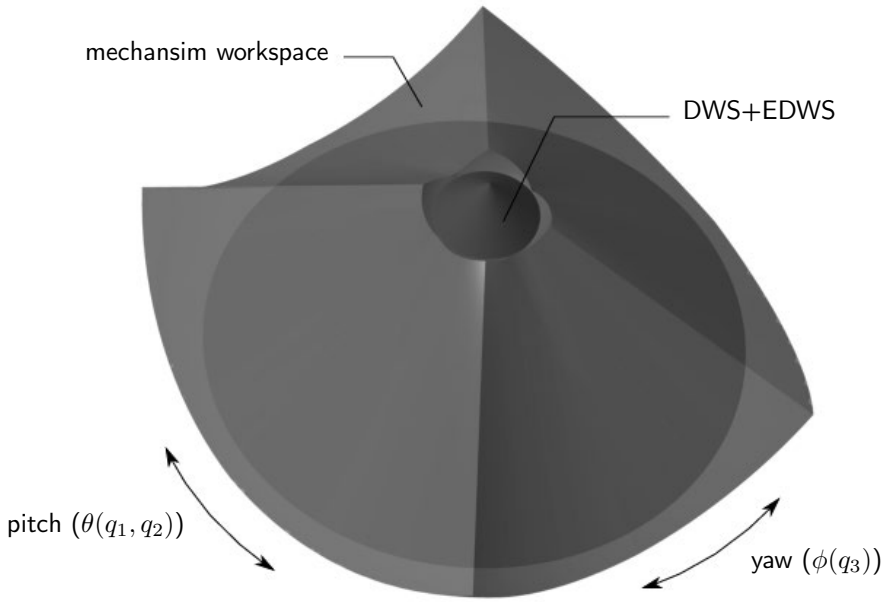

Figure 4-6: Mechanism workspace (light gray) and the required workspace for MIS (dark gray)

or in other words when the mutual angle between the links O_2E_1 and O_2G_1 will be 90° (Fig. 4-3), the mechanism will attain its *optimal configuration*. In MIS, majority of the organs lie towards the bottom of the surgical workspace. Hence, it is desirable to achieve maximum kinematic performance towards the bottom of the mechanism workspace.

4.5.4 Mechanism Workspace

To obtain the required workspace for MIS, we set the joint variables as $q_1 \in [\pi/4, \pi] \equiv \Omega_1$, $q_2 \in [0, 3\pi/4] \equiv \Omega_2$ and $q_3 = [-\pi/4, \pi/4] \equiv \Omega_3$ while maintaining the constraint,

$$q_1 \geq q_2 + \epsilon, \quad \epsilon > 0, \tag{4.12}$$

where ϵ is a constant to avoid singularities. Fig. 4-6 shows a comparison of the generated workspace and the required workspace for MIS with $l_2 = l_3 = 325$ mm. It is evident that the mechanism can generate enough workspace to cover the surgical workspace (the sum of DWS and EDWS). Any singularities with this range of joint variables and constraint occur outside of the required workspace.

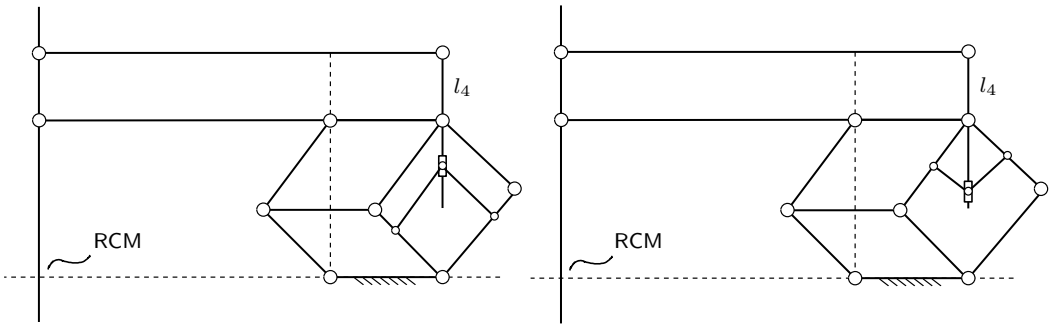

(a) (b)

Figure 4-7: Variant forms of the proposed RCM mechanism; (a) offers larger translation DoF with reduced length of l_4, (b) inverted alignment mechanism can generate even larger translation with further reduced length of l_4.

4.5.5 Variant Forms of the Mechanism

Variant forms of a mechanism provide the flexibility of choice for a particular form over the other in differing application scenarios. From (4.9), it is clear that higher value of k results in smaller s. Which means in order to maximize d for a given length of l_{41}, a higher value of k is favorable ($0 < k < 1$). Based on this inference, the lengths of the rear mini-parallelogram links can be further increased as shown in the Fig. 4-7(a). This results in longer *translation* DoF for the same overall size of the RCM mechanism.

Another variant form of the proposed mechanism can be achieved by implementing the *alignment mechanism* in inverted configuration as shown in Fig. 4-7(b). This results in even further reduced lengths for l_{41} and the support-links.

4.6 Mechanism Optimization

Forward kinematic equations show that the size of the mechanism workspace primarily depends on its ability to generate *pitch*, *yaw* and *translation* DoFs. As the *yaw* DoF has one-to-one mapping, it does not require optimization. However, it is important to optimize the mechanism design to achieve maximum manipulability (in *pitch* direction) and tool *translation* with minimum possible link lengths. For this purpose, we define a cost function (5.27) which is product of two functions; i) Average manipulability and ii) Effective translation. Average manipulability indicates the kinematic performance of a given design candidate (pair of α, l_2 where $\alpha = l_2/l_3$) and r_e provides a measure of *translation* DoF. Here r_e acts as a sizing constraint.

In this optimization, first we maximize and analyze the effect of average manipulability

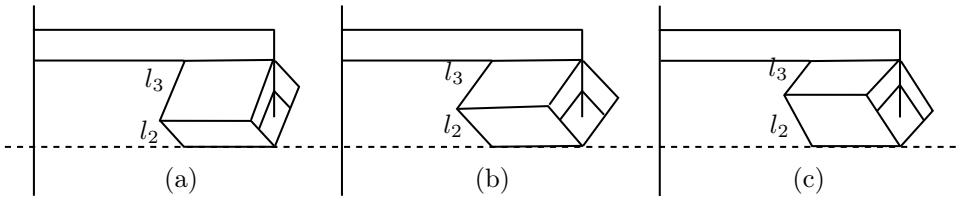

Figure 4-8: Corresponding mechanism forms for cases; (a) $\alpha < 1$, (b) $\alpha = 1$ and (c) $\alpha > 1$

($avg(w)$) and the effective translation (r_e) separately. Then we maximize the overall cost function (5.27) so that the resulting design offers better performance on both aspects.

4.6.1 Problem Statement

Find α and smallest l_2 in the proposed mechanism such that,

$$\max_{l_2,\alpha} \left(avg(w) \times r_e\right), \tag{4.13}$$

subject to,

$$(q_1, q_2) \in \Omega, \quad \Omega = \{(q_1, q_2) \in \mathbb{R}^2 : \pi/4 \leq q_1 \leq \pi, \\ 0 \leq q_2 \leq 3\pi/4.\}, \tag{4.14}$$

$$\alpha = l_2/l_3, \quad (\alpha > 0), \tag{4.15}$$

$$q_1 \geq q_2 + \epsilon, \quad (\epsilon > 0). \tag{4.16}$$

while,

$$r_{min} \text{ covers all elements in } \Omega_4, \quad \Omega_4 = \{\theta \in \mathbb{R} : \\ \pi/4 \leq \theta \leq 3\pi/4\}. \tag{4.17}$$

In the above statement r_e denotes the effective translation of tool tip below the RCM point, $avg(w)$ represents the average manipulability of a mechanism design candidate, r_{min} represents the distance of point C from A (Fig. 4-10) when the mechanism is in fully-retracted configuration (the end-effector is at the bottom of the workspace), and θ represents the desired range of *pitch* DoF (Fig. 4-4).

Next, we evaluate both functions and develop necessary mathematics to solve the optimization problem.

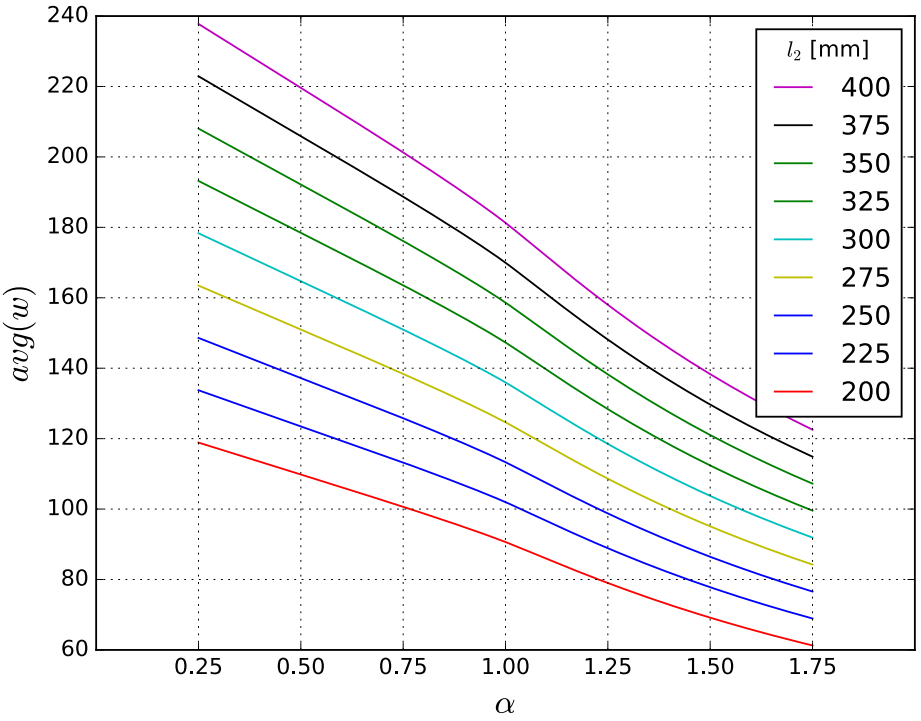

Figure 4-9: Average Manipulability over the range of α ($\alpha = l_2/l_3, \alpha > 0$)

4.6.2 Average Manipulability ($avg(w)$)

Derived from the manipulability measure [60], average manipulability function indicates the overall performance of a mechanism design candidate (pair of l_2, α) in the task space. We express it as,

$$avg(w) = \frac{1}{A} \int_{q_1} \int_{q_2} w(q_1, q_2)\, dq_2 dq_1. \tag{4.18}$$

where $w(q_1, q_2) = \texttt{det}J(q_1, q_2)$ and $A = \int_{\Omega_1} \int_{\Omega_2} dq_2 dq_1$.

$avg(w)$ Maximization

From (4.15) using $\alpha = l_2/l_3$, $\alpha > 0$, the manipulability measure (w) in (4.11) for the mechanism becomes,

$$w(q_1, q_2) = \left| \frac{l_2 \sin(q_1 - q_2)}{\sqrt{\alpha^2 + 2\alpha \cos(q_1 - q_2) + 1}} \right|. \tag{4.19}$$

Using (4.19), the average manipulability (5.32) is analyzed for the following three cases;

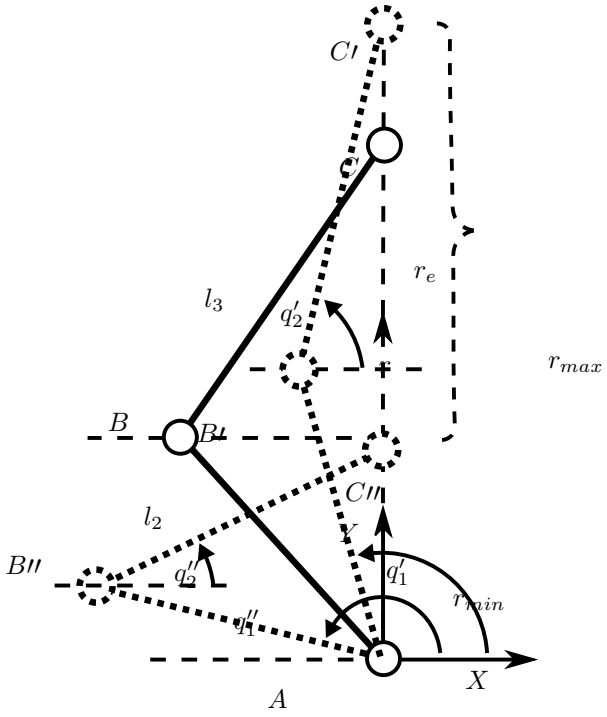

Figure 4-10: Effective Translation in the simplified representation of the proposed mechanism

For case:1, the denominator of (4.19) simply reduces to $\sqrt{2(1+\cos(q_1-q_2))}$. For case:2, when $\alpha < 1$ the denominator in (4.19) becomes smaller than the denominator in case:1. For same numerator, a smaller denominator in case:2 means that the resultant $avg(w)$ in case:2 will be bigger than $avg(w)$ in case:1.

Similarly for case:3, when $\alpha > 1$ it is obvious that the denominator in (4.19) becomes bigger than the one in case:1. For same numerator, bigger denominator means that the resultant $avg(w)$ in case:3 is smaller than the $avg(w)$ in case:1. This means $avg(w)$ in case:2 is bigger than the one in case:1 and $avg(w)$ in case:3 is smaller than that of the case:1. This implies that the $avg(w)$ in case:2 is also bigger than the $avg(w)$ in case:3. In other words, for any values of l_2, l_3 and given range of q_1, q_2, w will be maximum for case:2 only.

The above analytical findings are verified through numerical simulation. The plot in Fig. 4-9 demonstrates that for any l_2 the measure $avg(w)$ tends to maximize when α is less than one. Which means, smaller α yields higher average manipulability for the mechanism. Also, it suggests that longer $_2$ outputs higher average manipulability.

Therefore, the kinematic performance of the mechanism gets maximized for case:2,

$$\alpha < 1 \quad or \quad l_2 < l_3 \tag{4.20}$$

The above conclusion has certain impact on the physical form of the mechanism. Fig. 4-8 represents the corresponding mechanism forms for all three cases of α. For any given values of l_2 and l_3 average manipulability measure ($avg(w)$) is maximum for the form (a) in Fig. 4-8.

4.6.3 Effective Translation (r_e)

Effective translation represents the effective range of tool tip *translation* required for surgical purposes. In the simplified representation shown in Fig. 4-10, it is the distance traveled by point C on the line AC, denoted as r_e. It can be computed as $r_e = r_{max} - r_{min}$. Here r_{max} represents the distance of point C from A when the mechanism is in fully-extended configuration. In this situation, the corresponding angle q_1 is denoted as q_1' and q_2 as q_2'. Similarly, r_{min} represents the distance of C from A when the mechanism is in fully-retracted configuration, *i.e.* the end-effector tip is at the bottom of the mechanism workspace). In this situation, the corresponding angle q_1 is denoted as q_1'' and q_2 as q_2''. The limit of mechanism extension (r_{max}) is dictated by its geometric design, i.e. avoiding singularities. Whereas the limit of retracted configuration is defined by the range of desired pitch angles expressed in (5.31).

From Fig. 4-10, r_e can be expressed as,

$$\begin{aligned} r_e = {} & l_2 \sin(q_1') + l_3 \sin(q_2') - l_2 \sin(q_1'') \\ & - l_3 \sin(q_2''). \end{aligned} \tag{4.21}$$

If we assume $l_2 = \alpha l_3$, Fig. 4-11 shows the possible retracted configurations of the mechanism when $\theta = \pi/2$. From Fig. 4-11 it is clear that the mechanism will satisfy constraint (5.31) - achieve the desired pitch region - if the following two conditions hold true,

$$q_1 < 3\pi/4, \tag{4.22}$$

$$q_2 > \ \pi/4. \tag{4.23}$$

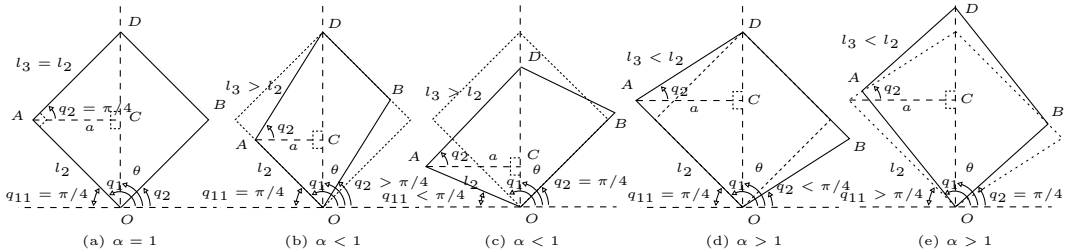

Figure 4-11: Rear-parallelogram configurations for cases $\alpha = 1$, $\alpha < 1$ and $\alpha > 1$ when $\theta = \pi/2$. Distance OD represents r_{min}. Only case (a), (b) and (e) can generate the desired workspace ($\pi/4 \leq \theta \leq 3\pi/4$) as they satisfy the constraint (4.22) and (4.23). As (c) and (d) do not satisfy (4.22) and (4.23), these are excluded from r_e optimization.

If (4.22) and (4.23) do not hold, the range of pitch motion of the mechanism becomes smaller than the desired pitch range as the mechanism reaches its limit without satisfying (5.31). Therefore, the result of r_e maximization for a design candidate satisfying (4.22) and (4.23) when $\theta = \pi/2$ can be generalized for any value of θ in the desired *pitch* range defined in (5.31). This reduces the problem complexity and computational load significantly. In Fig. 4-11 only case (a), (b) and (e) satisfy the conditions (4.22) and (4.23). As (c) and (d) do not satisfy (4.22) and (4.23), they are not considered for further optimization.

Now for case (a), it is easy to visualize that q_1 and q_2 have equal range of motion (both joints will move equally when the mechanism gets in to fully-extended configuration). For case (b), q_1 has larger range of motion than q_2 as q_2 will reach to $\pi/2$ from its current position more quickly than q_1 while the mechanism achieves fully-extended configuration. On similar lines, q_2 has larger range of motion than q_1 for case (e). Therefore for case (a) and (b), we calculate q_2 for any given q_1 and for case (e), we calculate q_1 for any given q_2.

From Fig. 4-11(a), the parallelogram $OADB$ can be expressed in terms of two triangles; $\triangle OAD$ and $\triangle OBD$. $\triangle OAD$ can be further divided into two right-angle triangles $\triangle OAC$ and $\triangle ACD$. From $\triangle OAC$,

$$a = l_2 \sin(q_1 - \pi/2), \tag{4.24}$$

and from $\triangle ACD$,

$$q_2 = \cos^{-1}\left(\frac{a\alpha}{l_2}\right). \tag{4.25}$$

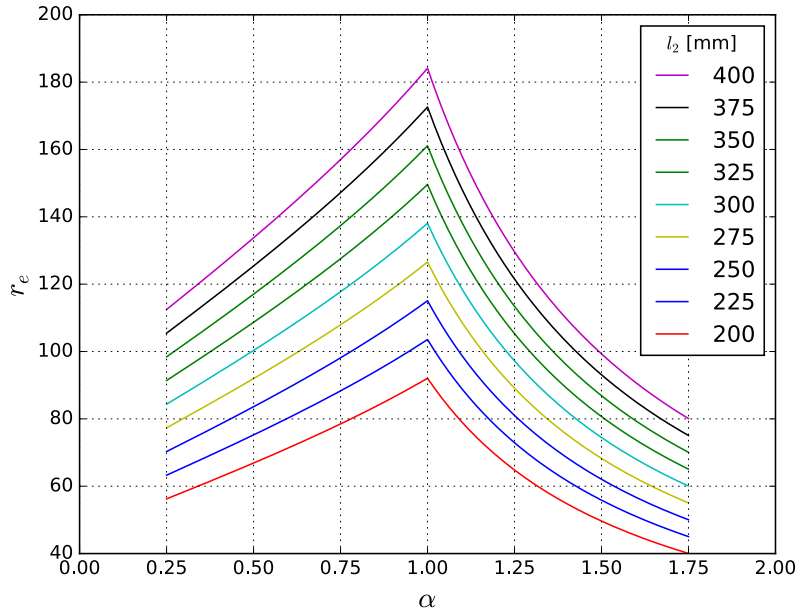

Figure 4-12: Effective Translation over the range of α ($\alpha = l_2/l_3, \alpha > 0$)

Substituting a from (4.24),

$$q_2 = \cos^{-1}(\alpha \sin(q_1 - \pi/2)). \tag{4.26}$$

Therefore, q_2' and q_2'' can be expressed as;

$$q_2' = \cos^{-1}(\alpha \sin(q_1'' - \pi/2), \tag{4.27}$$

$$q_2'' = \cos^{-1}(\alpha \sin(q_1' - \pi/2)). \tag{4.28}$$

For case (e) we express q_1 in terms of q_2. From (4.26), q_1 can be calculated as,

$$q_1 = \sin^{-1}(\cos(q_2)/\alpha) + \pi/2. \tag{4.29}$$

Therefore, q_1' and q_1'' can be expressed as;

$$q_1' = \sin^{-1}(\cos(q_2'')/\alpha) + \pi/2, \tag{4.30}$$

$$q_1'' = \sin^{-1}(\cos(q_2')/\alpha) + \pi/2. \tag{4.31}$$

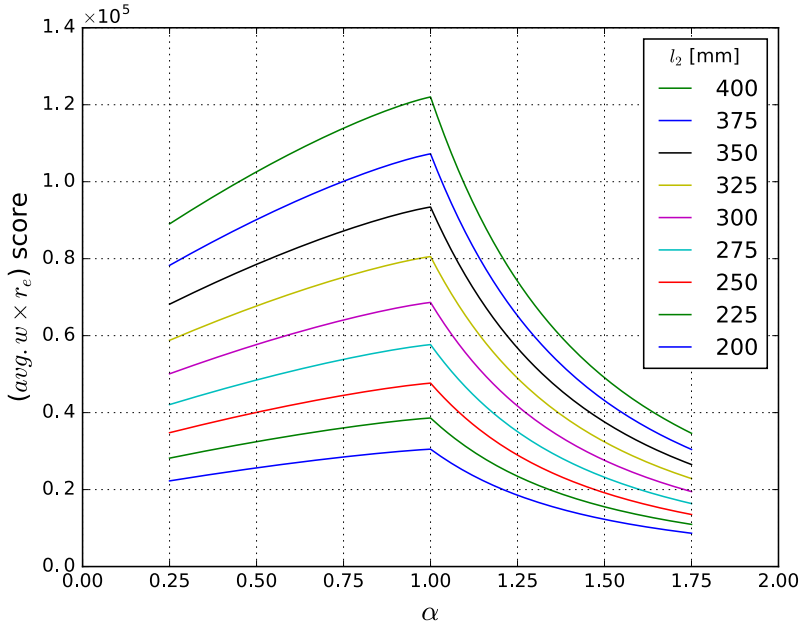

Figure 4-13: Combined performance score over the range of α ($\alpha = l_2/l_3, \alpha > 0$)

r_e Maximization

After the necessary formulation, we now maximize r_e with l_2 and α as tuning parameters. For case:1 and case:2 ($\alpha \leq 1$, Fig. 4-11(a) and (b)), r_e is evaluated by using q_2' and q_2'' as derived in (4.27) and (4.28). Similarly, for case:3 ($\alpha > 1$, Fig. 4-11(e)), r_e is evaluated by using q_1' and q_1'' as derived in (4.30) and (4.31) respectively.

The plot shown in Fig. 4-12 demonstrates that for all values of l_2 effective translation r_e tends to maximize when α is equal to one. Like the average manipulability function, longer link length of $_2$ returns higher value of r_e. Therefore, we conclude that for any corresponding values of l_2 and α, r_e favors case:1,

$$\alpha = 1 \quad or \quad l_2 = l_3 \tag{4.32}$$

Like the average manipulability maximization, the above conclusion also has certain impact on the physical form of the mechanism. Fig. 4-8 represents the corresponding mechanism forms for all three cases of α. For any given values of l_2 and α, effective translation (r_e) becomes maximum for the form (b).

4.6.4 Optimal Design

We now maximize the overall cost function (5.27) which is product of the average manipulability and the effective translation of the mechanism. The plot in Fig. 4-13 demonstrates that the overall cost function maximizes for case:1. Therefore, for any corresponding values of l_2 and α, the optimal design corresponds to the case:1,

$$\alpha = 1 \quad or \quad l_2 = l_3 \tag{4.33}$$

Hence, the optimum link lengths can be calculated by considering case:1. By substitute r_e in (4.21) with desired effective translation (r_{ed}) and using $\alpha = 1$, we can calculate l_2 and l_3. Similarly substituting R with desired effective translation (r_{ed}) and r with r_{min} in (4.2), l_1 can be determined to achieve the required workspace for MIS.

4.7 Summary

To solve the problems of existing 1 DoF RCM mechanisms, a new 2 DoFs planar RCM mechanism is proposed. The proposed design provides *pitch* and *translation* DoF without using any external means such as cable-pulleys or actuators mounted directly on the distal-end of the manipulator. The mechanism satisfies the MIS workspace requirements and an *optimal configuration* is selected such that the maximum kinematic performance is achieved towards the bottom of the workspace.

The design optimization shows that the maximum kinematic performance of the mechanism is achieved when the adjacent parallelograms have same lengths for the vertical links ($\alpha = 1$). It ensures that the maximum manipulability and translational motion of the end-effector is achieved with a minimum possible size of the mechanism.

Moreover, the proposed mechanism design does not include any active prismatic joints which makes it ideal for a fully-backdrivable manipulator design implementation. The geometric design of the mechanism is simpler than the existing 2 DoFs RCM mechanisms described in the state-of-the-art. It uses fewer number of links and joints than the mechanism proposed in [39]. Contrary to the solution in [50], the absence of any protruding links makes the mechanism more suitable for practical application as it minimizes chances of any untoward interference with the surgical site. Unlike [50], there is no cantilevered-link as the main part of this mechanism which results in a more rigid and stiffer design for surgical application.

The ability to achieve *translation* DoF without external means makes distal-end of the mechanism compact and slender. This is highly desirable in surgical applications where multiple robotic manipulators are supposed to work in close proximity. The compact distal-end makes it particularly suitable for surgeries where the tool is supposed to maneuver in confined and narrow spaces such as Laparoscopy and Retinal MIS. The mechanism is a potential choice for manipulator designs aimed at achieving high backdrivability, low design complexity, compact distal-ends and higher power transmission capabilities.

In the next chapter, we consider the problem of manipulator footprint and propose a modified design to offer even better prospects for applications in robot-assisted MIS.

Chapter 5

Multi-DoF RCM with Reduced Footprint

5.1 Motivation for the New Design

In the previous chapter, we have proposed and optimized a new RCM mechanism design that, contrary to the traditional RCM designs, offers the two most important DoFs—pitch and tool translation—required for surgery through its mechanism design. In this chapter, we will propose a new RCM design to even further extend the compatibility of design with the surgical environment. In other words, the motivation to behind the new design is to reduce the mechanism footprint and size, without sacrificing kinematic performance or functional capabilities, for easier setup in the surgical theater.

Just to provide a quick recap, traditionally 1-DoF planar RCM mechanisms (such as DP RCM mechanism described in Sec. 4-1) have been used to accomplish the surgical tasks. However, they are faced with numerous performance challenges as described in Sec. 4.2. To solve these problems, a number of new 2-DoF planar RCM mechanisms [39,41,50] have been proposed in recent years. These mechanisms (described in next section) provide pitch and yaw DoFs at the incision point purely through their mechanism design. Contrary to the 1-DoF RCM mechanisms, these designs achieve translation DoF by virtue of their mechanism design and, therefore, do not rely on the *external means* discussed above. However, with capability to produce translation DoF through their design, the 2-DoF RCM mechanisms have a significantly larger footprint (space required to setup and operate) than the 1-DoF RCM designs. Larger footprint means more space is required to setup and operate a

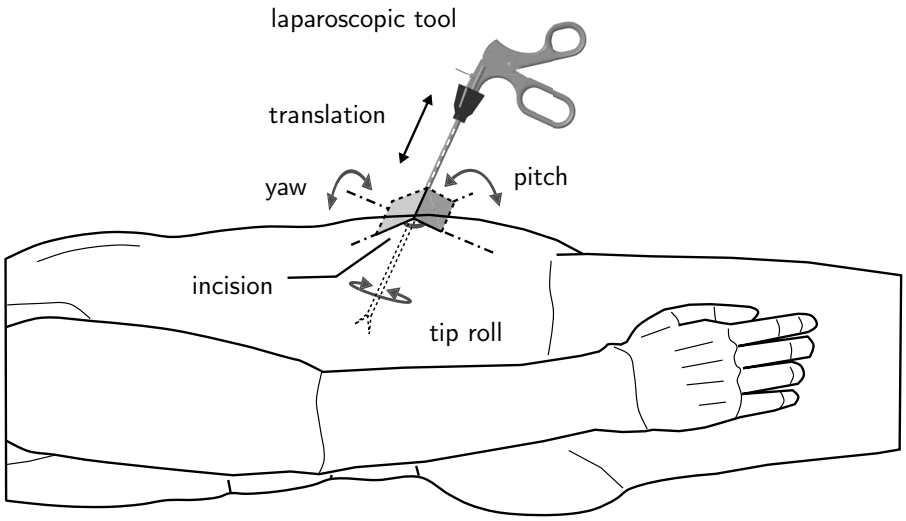

Figure 5-1: DoFs required at the incision point in a typical MIS procedure: pitch, yaw and translation. Another DoF, roll, can be implemented at the tip of surgical tool, as shown in the figure.

manipulator. This issue becomes even more significant in the case of MIS, where multiple (three or more) manipulators are required to complete a surgical procedure in a relatively confined space.

To solve this problem, we propose a new RCM mechanism design which offers the two most important DoFs — pitch and translation — through its mechanism design, but with a considerably smaller footprint. Novelty of the design lies in the fact that it achieves the pitch and translation DoFs by virtue of its mechanism design, and offers a smaller footprint without sacrificing the kinematic performance. As the proposed design does not rely on any *external means* to achieve translation DoF, it is supposed to offer a better operational performance than the existing state-of-the-art 2-DoF RCM designs. We also validate the RCM capability of the proposed design through simulation. To achieve the maximum kinematic performance with smallest size of the manipulator, an optimized design of the proposed mechanism is also presented.

5.2 State-of-the-Art 2-DoF RCM Designs

This section describes the existing 2-DoF planar RCM mechanisms, designed to overcome the limitations of 1-DoF RCM mechanisms. We highlight their salient features and point out potential downsides. The 2-DoF RCM mechanisms are a relatively new class of mechanisms [17], and the existing literature reports only three designs to the best of our knowledge.

The first 2-DoF planar RCM mechanism in this category is proposed by Li et al. [39]. It is essentially a 2-DoF planar design, based on the Diamond Mechanism presented in [63]. The mechanism achieves pitch and translation DoFs through its mechanical design. However, given the large link length ratios required to ensure the RCM constraint, the size of the mechanism becomes considerably large [41]. Also, the whole mechanical structure of the mechanism is supported by only two proximal links, which makes it statically unstable. A prototype manipulator based on this design has been developed to demonstrate its ability to maintain the RCM point [43].

Another interesting design is developed by Gijbels et al. [50]. it also provides pitch and translation DoFs through mechanism design and remotely from the distal end. It has a relatively simpler design and results in a compact manipulator design as compared to the mechanism in [39]. However, this design carries a downward protruding link towards the distal end which increases its overall footprint. When applied to MIS procedures such as Laparoscopy, the downward protruding link could cause interference with the patient side environment. Moreover, the whole weight of its distal end is supported by a single long cantilevered-link. This makes the whole design prone to vibrations caused at the end-effector tip. The design is originally intended for micro surgical procedures such as retinal MIS [40]. Its suitability for larger MIS procedures is not explored yet.

The third mechanism, described in our previous chapter [41], is also a planar RCM mechanism which offers pitch and translation DoFs through the mechanism deign. This design shown in Fig. 4-3, like the other two mentioned above, has a compact distal end and is fully-backdrivable. In addition, the design is optimized to yield maximum kinematic performance inside the surgical workspace. One common feature present in the existing designs is that they provide the two important DoFs through their mechanism design, and do not rely on *external means*, such as cable-pulleys and actuators mounted over the distal end of the manipulator, to achieve the translation DoF. This greatly enhances their operational life and suitability for applications demanding compact distal end and backdrivable design. Moreover, the footprint of this design is smaller than the above-mentioned mechanisms.

However, the cost of providing translation DoF through mechanism design comes in the form of increased footprint of the new designs. The 2-DoF mechanisms discussed above have considerably larger footprint as compared to the traditional 1-DoF RCM mechanisms. Larger footprint means bigger operational space is required for robot setup and movement. This becomes challenging, particularly for surgical applications where multiple robotic manipulators are required to operate in close proximity and in confined spaces [64–66].

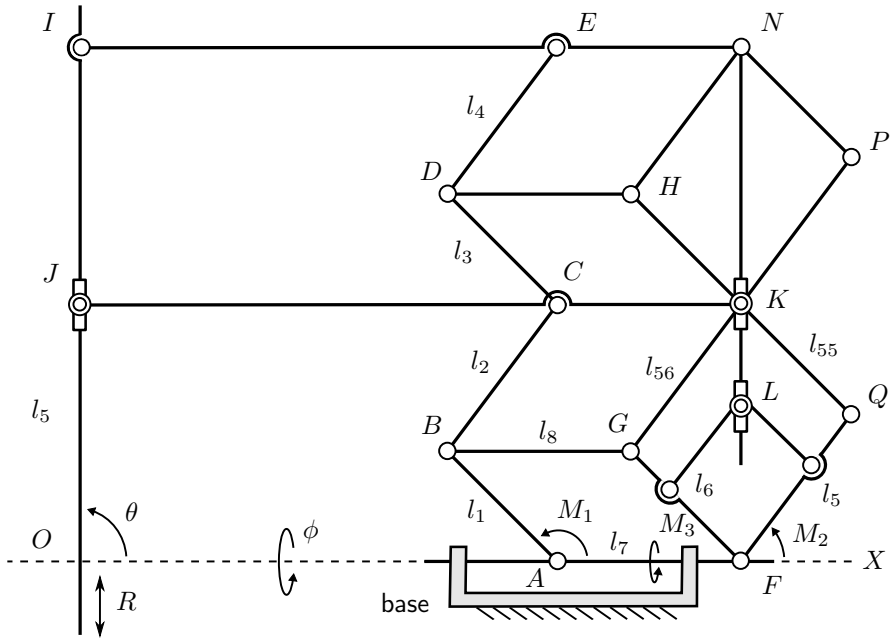

Figure 5-2: The proposed 2-DoF mechanism with RCM at point O. When actuated using M_1 and M_2 at proximal end, pitch (θ) and translation (R) DoFs are achieved at the distal end. Similarly, yaw (ϕ) DoF is obtained by tilting the mechanism along base link AF.

One way to minimize the chances of collision between the manipulators working in close proximity — considered critically important [67] — is to design mechanisms with compact distal ends and smaller footprint. The existing 2-DoF RCM designs — such as [50], [41], and [39] — offer a compact distal end but their larger footprint affects their suitability for MIS applications.

5.3 Proposed Mechanism Design

To solve the problem of larger footprint of the existing 2-DoF RCM mechanisms, we propose a new RCM design, capable to provide pitch and translation DoFs without using any *external means*, based on our previous work described in [41]. The key advantage of the new design is that it offers same kinematic performance and surgical workspace size as of the previous design, but with a smaller footprint. Figure 5-2 shows the proposed planar mechanism with scheme to achieve pitch and translation DoFs remotely from the distal-end. An additional DoF required for MIS, yaw, is realized by attaching a base along the link AF.

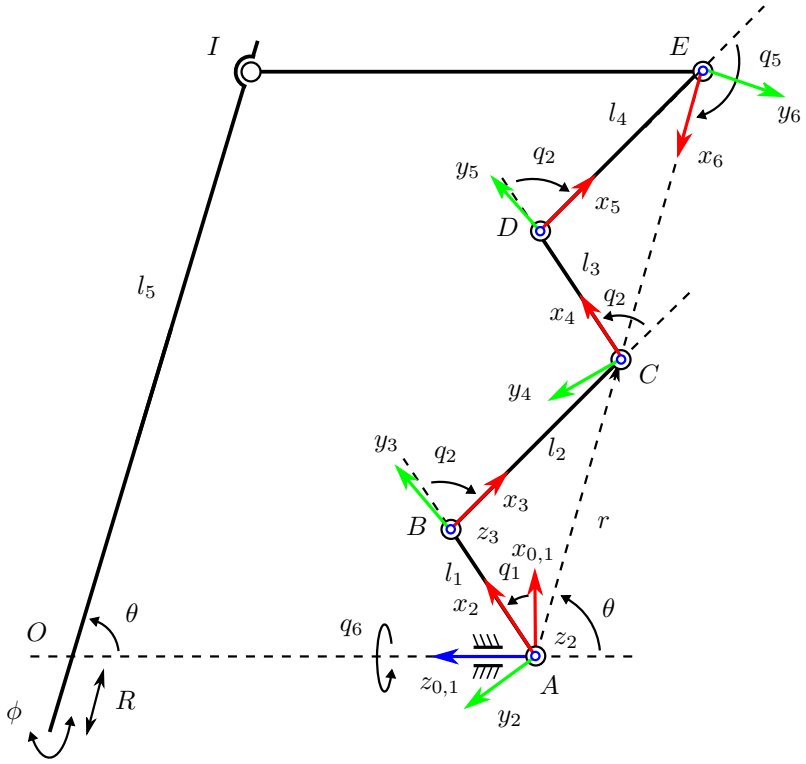

Figure 5-3: A simplified representation of the proposed mechanism with frames assigned according to Denavit-Hartenberg (DH) classic notation. Here, l denotes the link length, q represents the joint angles, θ, ϕ and R denote the pitch, yaw and translations DoFs respectively.

5.3.1 Mechanism Description

The proposed design makes use of double-parallelogram structures to achieve the desired function of providing indigenous pitch (θ) and translation (R) DoFs at the incision point. The incision point is technically referred as the RCM point, denoted by O in Fig. 5-2. The two actuators M_1 and M_2 can be installed at a number of locations in the mechanism to achieve the desired motion. However, as a general principle it is an intelligent choice to place actuators closer to the base of mechanism. This reduces the moving mass and ensuing gravitational effects due to increased inertia.

In the proposed design, when M_1 and M_2 actuate together in clockwise or anti-clockwise direction, pitch (θ) motion is achieved. When both actuators move in opposite direction to each other, motion in translation (R) direction is produced. Actuator M_3 can be used to tilt the whole mechanism along the base link AF to achieve yaw (ϕ) DoF while maintaining the RCM. J, K and L represent three passive prismatic joints while the remaining joints are passive revolute joints.

Table 5.1: Denavit-Hartenberg (DH) parameters for the simplified representation of the mechanism

i	α_i	a_i	d_i	θ_i
1	$\frac{\pi}{2}$	0	0	q_6
2	0	l_1	0	q_1
3	0	l_2	0	$-q_2$
4	0	l_3	0	q_2
5	0	l_4	0	$-q_2$
6	0	l_5	0	q_5

5.3.2 Kinematics

As the mechanism is composed of various parallelogram structures, a virtual parallelogram $OINF$ can be envisaged. Furthermore, the parallelograms $ABGF$ and $CDHK$ maintain identical configurations independent of the posture of mechanism. Same principle applies to the parallelogram $BCKG$ and $DENH$, which leads to another virtual parallelogram $AENF$. Due to the interconnected parallelograms, it is easy to conclude that link IO and NL will always remain parallel to each other as they are part of the same virtual parallelogram $OINF$. Moreover, links IN and JK will always remain horizontal independent of the pose of mechanism.

Next, due to the adjoining parallelograms $BCKG$ and $GKQF$ links FQ, GK and BC will always remain parallel to each other. This means the joint variable q_2 measured at $\angle CBG$ will be same as caused by actuator M_2 at $\angle QFX$. Above discussion simplifies the whole mechanism to the form shown in Fig. 5-3. Here, q_1, q_2 and q_6 represent the joint variables corresponding to actuators M_1, M_2 and M_3 respectively (Fig. 5-2). l_1, l_2, l_3, l_4 and l_5 denote the link lengths for segments AB, BC, CD, DE and IO, and $\vec{r}$ denotes the position vector from point A to C.

To formulate kinematics of the proposed mechanism, we use Denavit-Hartenberg's classic notation [59, 68] and assign frames to each joint as shown in Fig. 5-3. Based on this, a set of relevant DH parameters is provided in Table 5.1. Here, i denotes the joint number, α_i represents the twist angle, a_i is link length, d_i is joint offset and θ_i represents the respective joint angle.

In Table 5.1, q_5 is given by,

$$q_5 = \theta - q_1 + q_2 - \pi, \tag{5.1}$$

where θ can be expressed as,

$$\theta = \text{atan}\left(\frac{l_1 \sin q_1 + l_2 \sin(q_1 - q_2)}{l_1 \cos q_1 + l_2 \cos(q_1 - q_2)}\right). \tag{5.2}$$

Using the parameters in Table 5.1, a homogeneous transformation matrix mapping the orientation and position of the distal link tip to the base frame is formulated as,

$$T_1^6 = \begin{bmatrix} -\cos q_6 \cos\theta & \sin\theta \cos q_6 & \sin q_6 & p_x \\ -\sin q_6 \cos\theta & \sin q_6 \sin\theta & -\cos q_6 & p_y \\ -\sin\theta & -\cos\theta & 0 & p_z \\ 0 & 0 & 0 & 1 \end{bmatrix}, \tag{5.3}$$

where,

$$p_x = \{(l_1 + l_3)\cos q_1 + (l_2 + l_4)\cos(q_1 - q_2) - l_5 \cos\theta\}\cos q_6, \tag{5.4}$$

$$p_y = \{(l_1 + l_3)\cos q_1 + (l_2 + l_4)\cos(q_1 - q_2) - l_5 \cos\theta\}\sin q_6, \tag{5.5}$$

$$p_z = (l_1 + l_3)\cos q_1 + (l_2 + l_4)\cos(q_1 - q_2) - l_5 \sin\theta. \tag{5.6}$$

Equations (5.4, 5.5, 5.6) constitute the forward kinematics of the mechanism expressing distal link tip position in Cartesian space using joint angles and related link lengths expressed in inertial frame of reference. Further, the distal link tip velocities $\dot{p_x}, \dot{p_y}$ and $\dot{p_z}$ can be mapped to the joint velocities $\dot{q_1}, \dot{q_2}$ and $\dot{q_6}$ as,

$$\begin{bmatrix} \dot{p_x} \\ \dot{p_z} \\ \dot{p_y} \end{bmatrix} = J(q_1, q_2, q_6) \begin{bmatrix} \dot{q_1} \\ \dot{q_2} \\ \dot{q_6} \end{bmatrix}, \tag{5.7}$$

where $J(q_1, q_2, q_6)$ denotes the velocity Jacobean matrix.

5.3.3 Reduced Footprint

To emphasize the reduced footprint of the new design, we perfrom a geometric comparison between the proposed design and the mechanism described in [41]. Fig. 5-4 demonstrate that for the same base link lengths ($l_{01} = l_{02}$) and height ($h_1 = h_2$), the resulting link

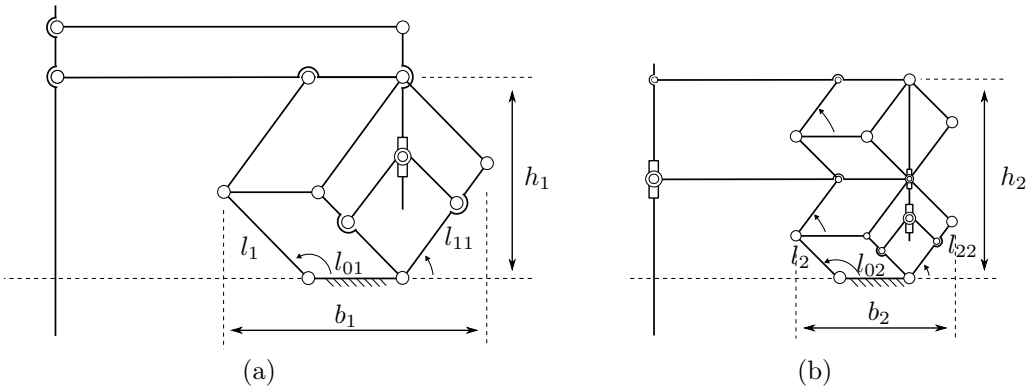

Figure 5-4: Footprint comparison between an existing design (a) and the proposed design (b): For $l_{01} = l_{02}$ and $h_1 = h_2$, the footprint b_2 is smaller than the footprint b_1. Similarly, the link length l_2 and l_{22} are also reduced to half of the original link lengths l_1 and l_{11}. The reason for reduction in footprint of (b) pertains to the addition of extra parallelograms between the two long horizontal links at the top of the mechanism.

lengths l_2, l_{22} are equal to half of the respective link lengths (l_1, l_{11}) in previous design. This indicates that the footprint b_2 of the proposed design will also be smaller than b_1, which is the footprint of previous design. This is expressed as,

$$\because \quad l_2 = \frac{l_1}{2}, \quad l_{22} = \frac{l_{11}}{2}, \tag{5.8}$$

$$\therefore \quad b_2 = \frac{b_1 + l_{01}}{2}, \quad l_{01} = l_{02}. \tag{5.9}$$

Numerical calculations show that for equal size of the mechanism workspace (Sec. 5.3.7), the proposed design has a smaller footprint ($b_2 = 49.2$ cm) than that of an existing design shown in Fig. 5-4(a) ($b_1 = 81.6$ cm). It is important to mention that the mechanism design shown in Fig. 5-4(a) has smallest footprint among the three existing state-of-the-art designs described in Sec. 5.2. This means the proposed design offers smallest footprint of all the three 2-DoF RCM designs.

Next, we validate the RCM capability of the proposed design and investigate whether the reduced footprint has any adverse affects over the mechanism performance in terms of operating range, workspace size and mechanism manipulability. The optimization results (Sec. 5.4) demonstrates that even with a considerably smaller footprint, the proposed design provides same kinematic performance as of an existing design with larger footprint (shown in Fig. 5-4(a)).

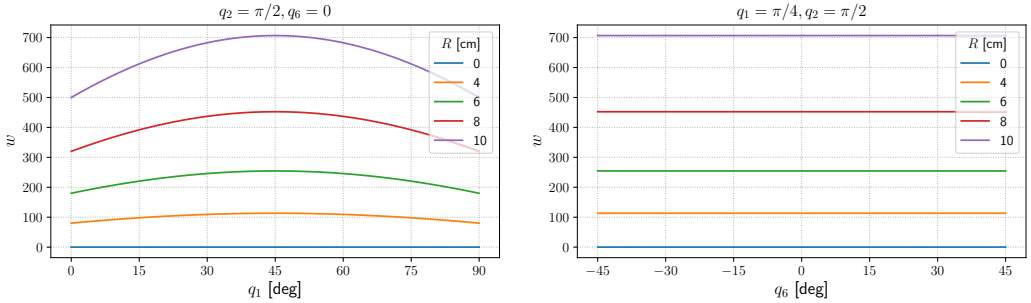

(a) Manipulability in pitch (θ) direction (b) Manipulability in yaw (ϕ) direction

Figure 5-5: Manipulability measure (w) for the proposed design at various distal-link tip positions (R): In both pitch and yaw directions, when the tip of distal link coincides with the RCM point ($R = 0$), the manipulability remains zero. When the tip is below the RCM point ($R > 0$), w maintains a non-zero positive value.

5.3.4 RCM Validation

It is important to validate the RCM capability of the proposed design for the desired operating range. For this purpose, we make use of Yoshikawa's manipulability measure (w) [60] to validate that the proposed design is essentially an RCM mechanism, i.e., maintains an RCM constraint. As the proposed design has a square Jacobian matrix (5.7), its manipulability can be expressed as,

$$w = \det J(q_1, q_2, q_6), \quad w \geq 0. \tag{5.10}$$

By definition, the part of mechanism passing through the RCM point should observe no lateral movement in pitch and yaw directions for the complete range of mechanism movement [17]. Here, we will use manipulability (w) to demonstrate that the mechanism generates no lateral movement at the RCM point. For this purpose, we consider two cases; (i) when the tip of distal link coincides with the RCM point ($R = 0$), and (ii) when the tip of distal link is below the RCM point at any arbitrary distance ($R > 0$). Ideally for case (i), manipulability of the proposed design should remain zero for the complete range of motion. On the other hand, for case (ii) it should remain higher than zero for the same range of motion unless the mechanism goes into a singular configuration.

Figure 5-5(a) shows the mechanism manipulability in pitch direction. It is clear that at $R = 0$, w remains zero. This means tip of the distal link has zero velocity in this situation. However, the w maintains a positive non-zero value when $R > 0$. Similarly, Fig. 5-5(b)

shows the mechanism manipulability in yaw direction. As can be seen from the plots, it exhibits similar behavior to the w in pitch direction. Therefore, it becomes evident that for the given range of motion in pitch and yaw DoFs, the manipulability w remains zero for $R = 0$, and maintains a higher than zero value for $R > 0$. From this we conclude that the proposed mechanism is an RCM mechanism; its manipulability remains zero at a certain point in its workspace ($R = 0$), while maintains a non-zero for all cases when the tip of distal link is below the RCM point.

5.3.5 Mechanism Singularities

To further analyze the mechanism workspace and its optimal configuration, it is important to identify mechanism singularities. The proposed mechanism will be in singular configuration when $\texttt{det}J(q) = 0$. However, the Jacobian matrix given by (5.7) is too complex to solve analytically. To obtain a relatively simpler Jacobian matrix for singularity and optimal configuration analysis (discussed in next section), we rewrite the forward kinematic equations in terms of spherical coordinates.

Considering the simplified representation of the mechanism shown in Fig. 5-6, pitch, yaw and translation can be obtained as,

$$\theta = \tan^{-1}\left(\frac{(l_1 + l_3)\sin(q_1) + (l_2 + l_4)\sin(q_2)}{(l_1 + l_3)\cos(q_1) + (l_2 + l_4)\cos(q_2)}\right), \tag{5.11}$$

$$R = l_5 - \sqrt{((l_1 + l_3)\sin(q_1) + (l_2 + l_4)\sin(q_2))^2} \\ \overline{+ ((l_1 + l_3)\cos(q_1) + (l_2 + l_4)\cos(q_2))^2}, \tag{5.12}$$

$$\phi = q_6. \tag{5.13}$$

Contrary to the simplified representation in Fig. 5-3, the form shown in Fig. 5-6 uses absolute values for joint variables q_1, q_2 and q_3. Now, expressing the tip velocities of the distal link in terms of relevant joint variables results in,

$$\begin{bmatrix} \dot{R} \\ \dot{\theta} \\ \dot{\phi} \end{bmatrix} = J_{(q)} \begin{bmatrix} \dot{q_1} \\ \dot{q_2} \\ \dot{q_6} \end{bmatrix}, \tag{5.14}$$

where, $\dot{R}$, $\dot{\theta}$ and $\dot{\phi}$ are tip translational and rotational velocities, $\dot{q_1}$, $\dot{q_2}$ and $\dot{q_6}$ are joint velocities, and $J_{(q)}$ is Jacobian to map joint velocities to tip velocities. The Jacobian matrix,

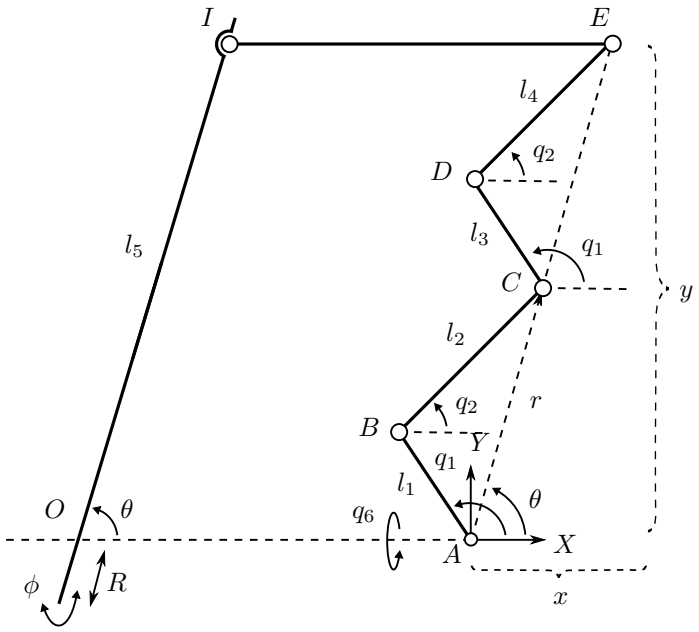

Figure 5-6: The simplified representation of the mechanism with absolute joint variables q_1, q_2 and q_6

$$J_{(q)} = \begin{bmatrix} \frac{A}{\sqrt{E}} & \frac{B}{\sqrt{E}} & 0 \\ \frac{C}{\sqrt{E}} & \frac{D}{\sqrt{E}} & 0 \\ 0 & 0 & 1 \end{bmatrix}, \tag{5.15}$$

has elements,

$$A = (l_1 + l_3)(l_2 + l_4)\sin(q_1 - q_2), \tag{5.16}$$

$$B = -(l_1 + l_3)(l_2 + l_4)\sin(q_1 - q_2), \tag{5.17}$$

$$C = (l_1 + l_3)(l_2 + l_4)\cos(q_1 - q_2) + (l_1 + l_3)^2, \tag{5.18}$$

$$D = (l_1 + l_3)(l_2 + l_4)\cos(q_1 - q_2) + ((l_2 + l_4)^2, \tag{5.19}$$

$$E = ((l_1 + l_3)\cos q_1 + (l_2 + l_4)\cos q_2)^2 + ((l_1 + l_3)\sin q_1 + (l_2 + l_4)\sin q_2)^2. \tag{5.20}$$

To find singular configurations of the proposed mechanism, we solve det $J_{(q)} = 0$,

$$detJ(q) = \left| \frac{\beta \sin(q_1 - q_2)}{\sqrt{\gamma + 2\beta\cos(q_1 - q_2)}} \right|, \tag{5.21}$$

where,

$$\beta = (l_1 + l_3)(l_2 + l_4), \tag{5.22}$$

$$\gamma = (l_1 + l_3)^2 + (l_2 + l_4)^2. \tag{5.23}$$

Solving Eq. (5.21) leads to,

$$\{(q_1, q_2) | q_1 = q_2, q_1 = q_2 \pm \pi\}. \tag{5.24}$$

Geometrically, these singularities correspond to the mechanism configurations when parallelogram $ABGF$ and $BCFG$ become aligned, i.e. the link AB and BC become parallel to each other (Fig. 5-2). Same condition also applies to parallelograms $CDHK$ and $DENH$.

5.3.6 Optimal Configuration

Optimal configuration of a mechanism is defined as the configuration in which the mechanism attains maximum manipulability [60]. It gives important information about the initial desired configuration of the robotic manipulator. As mentioned earlier, for mechanisms with square Jacobian matrix *manipulability* is defined as $w = \texttt{det}J(q), w \geq 0$.

For the proposed design, the manipulability measure is expressed in (5.21). It is clear that the manipulability measure (w) becomes maximum when,

$$q_1 = q_2 + (\pi/2). \tag{5.25}$$

Geometrically, this means when links AB and BC will be at right angle to each other, or in other words when the mutual angle between the links GF and FQ will be 90° (Fig. 5-2), the mechanism will attain its *optimal configuration*.

5.3.7 Workspace Comparison

This section describes the mechanism workspace and its comparison with the required workspace for MIS. To obtain the mechanism workspace, we set joint variables as $q_1 \in [\pi/4, \pi] \equiv \Omega_1$, $q_2 \in [0, 3\pi/4] \equiv \Omega_2$ and $q_6 = [-\pi/4, \pi/4] \equiv \Omega_3$ while maintaining the constraint,

$$q_1 \geq q_2 + \epsilon, \quad \epsilon > 0, \tag{5.26}$$

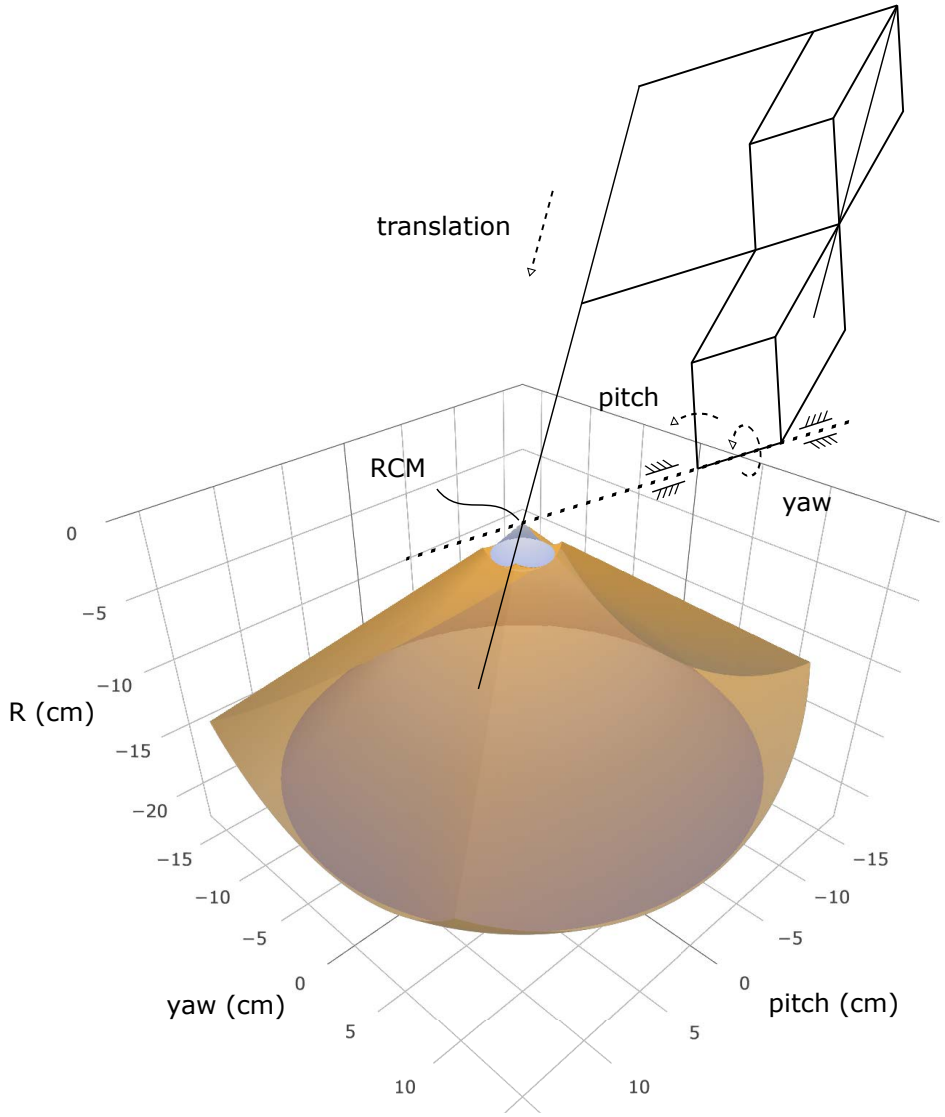

Figure 5-7: Mechanism workspace and its comparison with the required workspace for MIS (inscribed conic volume). Horizontal axes show the workspace size in pitch and yaw DoFs. The vertical axis represents tool translation (R) below the RCM point.

where ϵ is a constant to avoid singularities. Fig. 5-7 shows the resulting mechanism workspace in Cartesian space. The required workspace for MIS is shown as the inscribed volume inside the mechanism workspace. The required workspace is used as a conic region with vertex angle of 90° [49, 55]. It is evident that the mechanism satisfies the workspace requirements for MIS, and is capable to generate more workspace than the required. Furthermore, it is important to note that despite having a smaller footprint the workspace size of the proposed design is equal to that of the RCM design [41] with a relatively larger footprint.

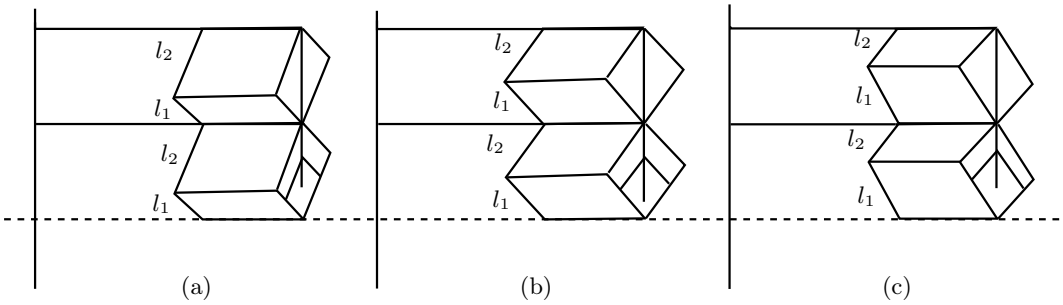

Figure 5-8: Three different forms of the proposed design: (a) when $\alpha < 1$, (b) when $\alpha = 1$, and (c) when $\alpha > 1$, where $\alpha = l_1/l_2, \alpha > 0$. Although the three forms have same function, they offer different kinematic performance in terms of manipulability and tool translation.

5.4 Mechanism Optimization

Objective of this optimization is to find the best performing design in terms of *manipulability* and *tool translation* below the RCM point, with smallest possible size of the mechanism. Fig. 5-8 shows three different possible forms of the proposed design. All three forms have same function but they yield different kinematic performance. The manipulability and tool translation capabilities are affected by the geometric considerations of various link lengths. After finding the optimized design for the proposed mechanism with smaller footprint, we will compare its performance with a previously proposed design with larger footprint. Here we largely follow the optimization scheme used in [41], however the new design requires changes in the mathematical formulation which is described in the course of this sections. We state the optimization problem as given below.

5.4.1 Problem Statement

Find α and smallest l_1 in the proposed mechanism such that,

$$\max_{l_1,\alpha} \left(avg(w) \times r_e\right), \tag{5.27}$$

subject to,

$$(q_1, q_2) \in \Omega, \quad \Omega = \{(q_1, q_2) \in \mathbb{R}^2 : \pi/4 \leq q_1 \leq \pi, \\ 0 \leq q_2 \leq 3\pi/4.\}, \tag{5.28}$$

$$\alpha = l_1/l_2, \quad (\alpha > 0, l_1 = l_3, l_2 = l_4), \tag{5.29}$$

$$q_1 \geq q_2 + \epsilon, \quad (\epsilon > 0). \tag{5.30}$$

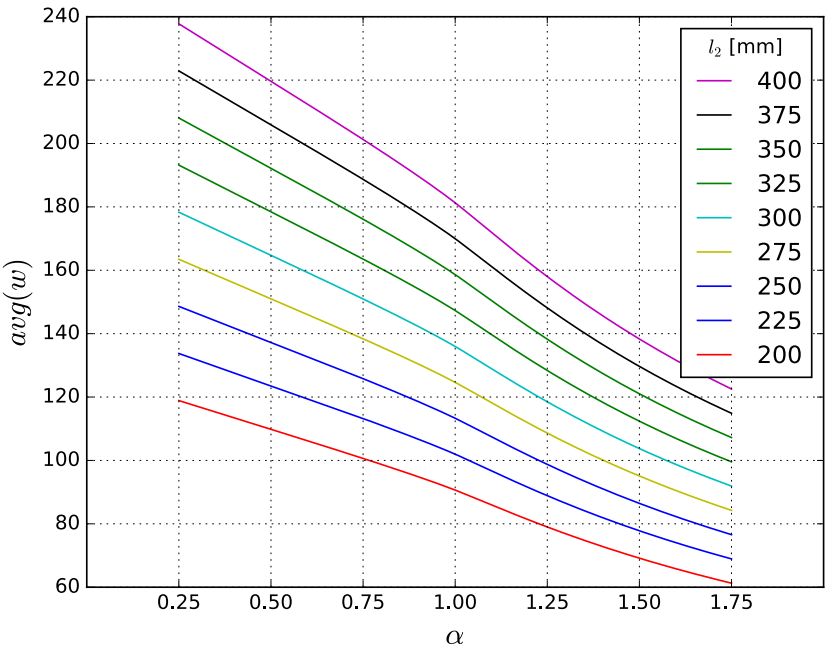

Figure 5-9: Average manipulability ($avg(w)$) over the range of α, ($\alpha = l_1/l_2, \alpha > 0.$), for various values of link length l_1

while,

$$r_{min} \text{ covers all elements in } \Omega_4, \quad \Omega_4 = \{\theta \in \mathbb{R} : \pi/4 \leq \theta \leq 3\pi/4\}. \tag{5.31}$$

In the statement above, r_e denotes the effective translation of the tool tip below the RCM point, $avg(w)$ represents the average manipulability of a mechanism design candidate (pair of l_1, α), r_{min} represents the distance of point E from A (Fig. 5-10) when the mechanism is in fully-retracted configuration (the end-effector is at the bottom of the workspace), and θ represents the desired range of the *pitch* DoF (Fig. 5-3). The assumption that $l_1 = l_3, l_2 = l_4$ in (5.29) is meant to produce a symmetric form of the mechanism.

5.4.2 Average Manipulability ($avg(w)$)

Average manipulability indicates the overall performance of a mechanism design candidate (pair of l_1, α) for considered joint space.

$$avg(w) = \frac{1}{A}\int_{q_1}\int_{q_2} w(q_1, q_2)\, dq_2 dq_1, \tag{5.32}$$

where,

$$w(q_1, q_2) = \texttt{det}\left(J(q_1, q_2)\right), \tag{5.33}$$

$$A = \int_{\Omega_1}\int_{\Omega_2} dq_2 dq_1. \tag{5.34}$$

$avg(w)$ **Maximization**

As described earlier, the manipulability measure is given by $w = det|J(q)| \quad , w \geq 0$. Based on assumption (5.29), we can rewrite manipulability (w) using $l_1 = l_3, l_2 = l_4$,

$$w = \left| \frac{2l_1 l_2 \sin\left(q_1 - q_2\right)}{\sqrt{l_1^2 + 2l_1 l_2 \cos\left(q_1 - q_2\right) + l_2^2}} \right|. \tag{5.35}$$

Now using $l_1 = \alpha l_2$, Eq. (5.35) can be further expressed as,

$$w = \frac{2l_1^2 \sin\left(q_1 - q_2\right)}{\alpha\sqrt{l_1^2\left(1 + \frac{2}{\alpha}\cos\left(q_1 - q_2\right) + \frac{1}{\alpha^2}\right)}}. \tag{5.36}$$

Next, we maximize the $avg(w)$ for the joint variable range mentioned in (5.28), and for various values of α and l_1. The resultant plot is shown in Fig. 5-9, which clearly shows that the $avg(w)$ tends to maximize as α decreases and l_1 increases. Among the three mechanism forms shown in Fig. 5-8, this corresponds to the case when $\alpha < 1$.

5.4.3 Effective Translation (r_e)

The ability of the mechanism to produce enough tool translation below the RCM (incision) point is an important characteristics for MIS applications. In this section, we optimize the proposed design to achieve maximum tool translation with minimum possible size of the mechanism. For this purpose, we define the tool translation below the RCM point as the 'effective translation' (r_e). For the proposed mechanism, this represents the displacement

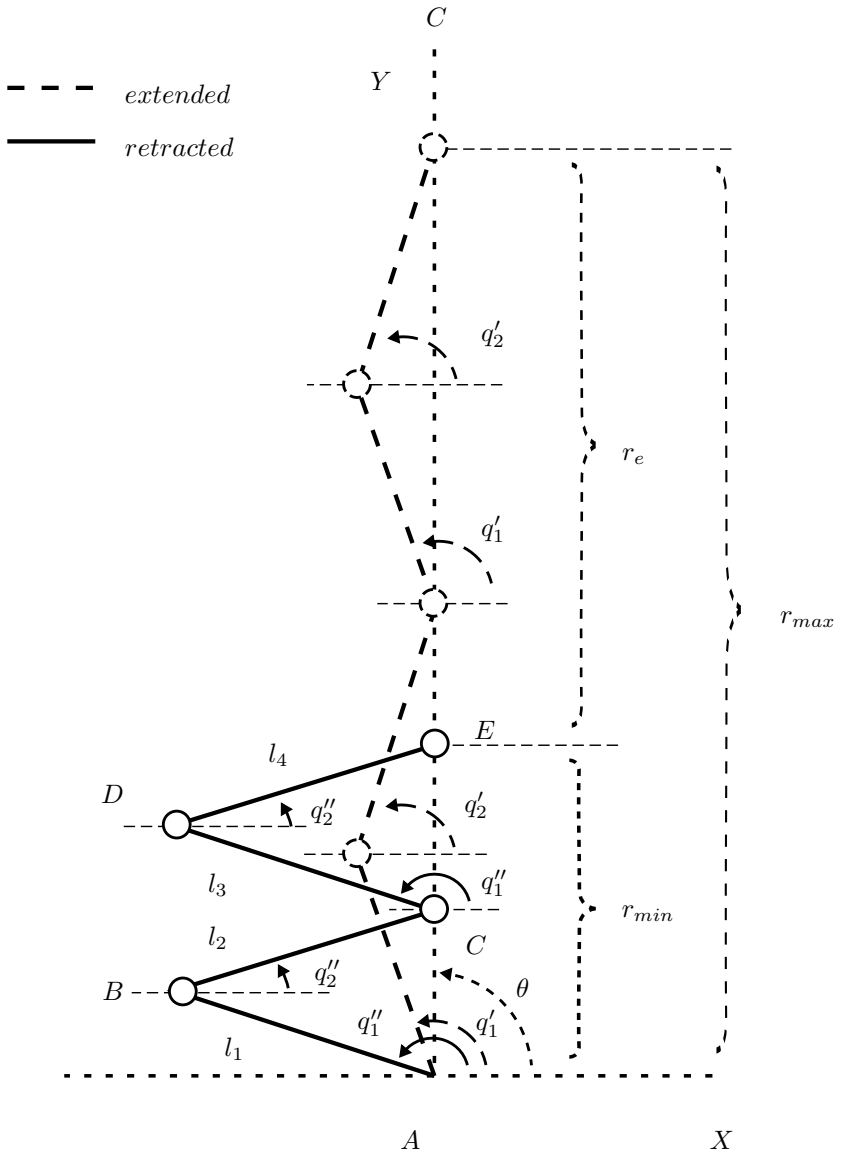

Figure 5-10: Effective translation (r_e) of the mechanism: The distal link tip can translate up and down through the RCM point at a distance equal to r_e below the RCM point. r_{min} and r_{max} denote the distance of point E from base O when mechanism is in retracted and extended forms, respectively.

of point E on line AC.

$$r_e = r_{max} - r_{min}, \tag{5.37}$$

$$r_e = (l_1 + l_3)\sin q_1' + (l_2 + l_4)\sin q_2' - (l_1 + l_3)\sin q_1'' - (l_2 + l_4)\sin q_2''. \tag{5.38}$$

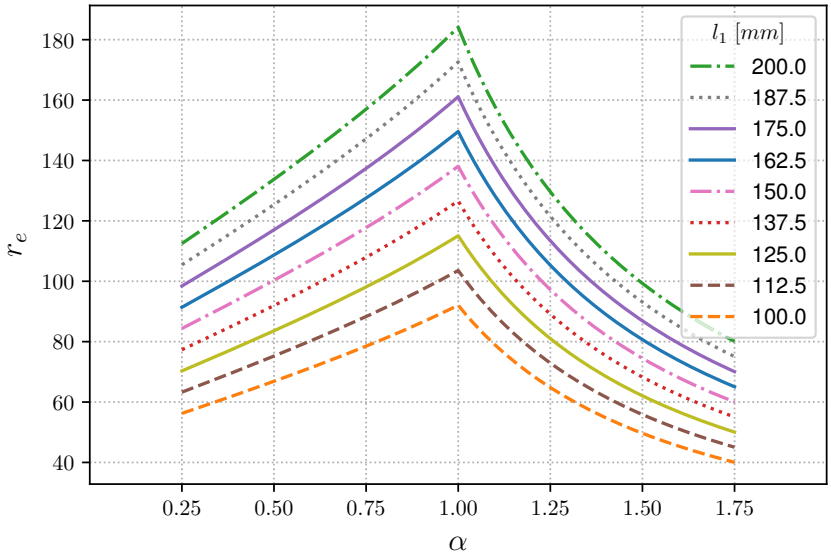

Figure 5-11: Effective Translation (r_e) over the range of α, ($\alpha = l_1/l_2, \alpha > 0.$), for various values of link length l_1

Here, q_1' and q_2' denote the corresponding values of q_1 and q_2, respectively, when the mechanism is in fully-extended configuration. Similarly, q_1'' and q_2'' denote the corresponding values of q_1 and q_2, respectively, when the mechanism is in fully-retracted configuration.

r_e Maximization

For r_e maximization, we rewrite (5.38) using $l_1 = l_3, l_2 = l_4$ and $l_1 = \alpha l_2$, $(\alpha > 0)$ from (5.29) as,

$$r_e = \frac{2l_1}{\alpha}\{\alpha(\sin q_1' - \sin q_1'') + (\sin q_2' - \sin q_2'')\} \tag{5.39}$$

Next, we plot r_e from (5.39) over the range of α for various values of link length l_1. Fig. 5-11 shows that r_e maximizes for design case when $\alpha = 1$, i.e. $l_1 = l_2$. These results are derived for a subspace of q_1 and q_2 (specifically when $\theta = \pi/2$), but they can be generalized and hold true for the whole range of q_1 and q_2 given in (5.28) [41]. Among the three mechanism forms given in Fig. 5-8, this corresponds to the form when $\alpha = 1$.

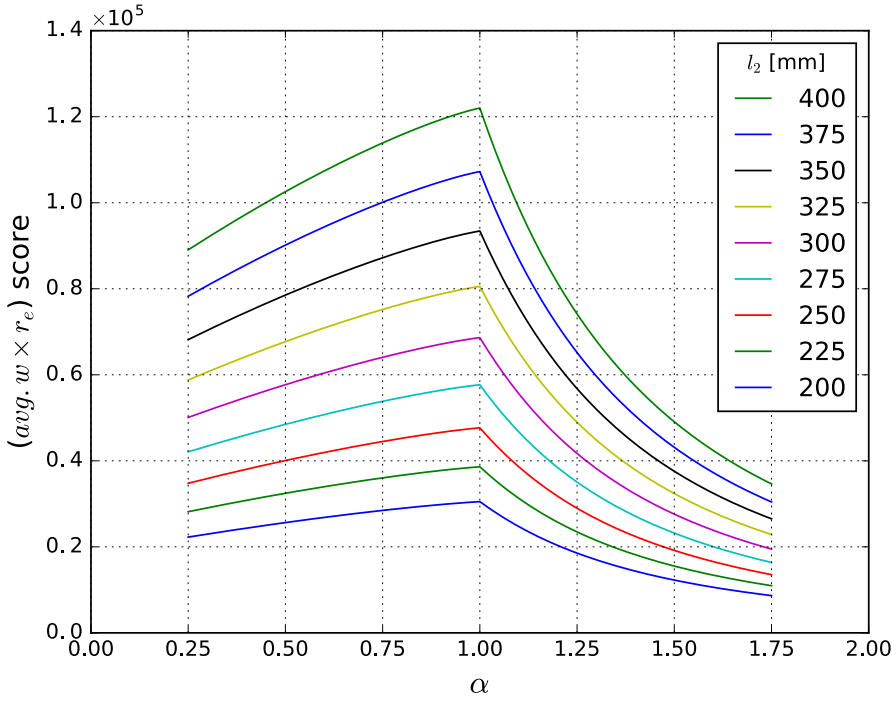

Figure 5-12: Combined score $(avg(w) \times r_e)$ over the range of α, $(\alpha = l_1/l_2, \alpha > 0.)$, for various values of link length l_1

5.4.4 Optimal Design of the Mechanism

To determine an optimal design of the proposed mechanism, we solve the overall cost function (5.27) for all design candidates (pairs of α, l_1) over the given range of joint variables. The combined score, which is a product of the average manipulability $(avg(w))$ and the effective translation (r_e), makes sure that the optimal design yields the best kinematic performance with minimum possible size of the mechanism. Here, $avg(w)$ indicates the kinematic performance while r_e acts as a sizing constraint. The resulting plots shown in Fig. 5-12 demonstrate that the combined score $(avg(w) \times r_e)$ maximizes for case when $\alpha = 1$, i.e. $l_1 = l_2$.

To achieve a tool translation of 20 cm below the RCM point, we can calculate the required optimal link length l_1 using eq. (5.39) and $\alpha = 1$. This results $l_1 = l_2 = l_3 = l_4 = 16.25$ cm. Similarly using $r_e = R$ in Eq. (5.12), l_5 can be computed by using $l_1 = 16.25$cm and $\alpha = 1$ when the mechanism is in its optimal configuration.

5.5 Results and Discussion

Figure 5-4 and the results from Eq.(5.9) demonstrate that the proposed design's footprint is 1.6 times smaller that of an existing design presented in [41]. This conclusion also holds true for the design proposed in [50], where the footprint is even larger than that of the mechanism in [41]. Additionally, the workspace shown in Fig. 5-7 demonstrates that even with reduced footprint, the workspace size remains same as that of the design in [41].

Figure 5-7 shows that the mechanism's generated workspace satisfies the MIS workspace requirements, depicted by the conic volume. Similarly, Fig. 5-5 demonstrates the RCM capability of the proposed mechanism. When the tip of the distal end coincides with the RCM point (Fig. 5-5(a)), the manipulability measure (w) goes to zero. This is an indication that there is no lateral movement of tip at the RCM point in any direction for the whole range of movement in pitch and yaw DoFs. When the tip is not at the RCM point (Fig. 5-5(b)), the mechanism manipulability has a positive nonzero value. This means that the mechanism possess an RCM point and, therefore, is an RCM mechanism.

Optimization results in Fig. 5-9 indicate that the manipulability measure ($avg(w)$) tends to maximize when the link lengths l_1, l_3 are smaller than l_2, l_4. The effective translation r_e results show that it becomes maximum when l_1, l_2, l_3, l_4 are equal to each other, as shown in Fig. 5-11. The combined score (product of $avg(w)$ and r_e) shown in Fig. 5-12 also tends to be maximum for case $l_1 = l_2 = l_3 = l_4$. These results confirm that despite of having reduced link lengths and a smaller footprint, the proposed design offers same kinematic performance as that of the design previously presented in [41].

Additionally, the mechanism offers a more rigid structure where the center of gravity remains relatively closer to the proximal end of the mechanism. This helps improve the static stability of the design and reduces the overall inertia of the moving structure. As the actuators required to achieve pitch and translation DoFs in this design can be installed near the base, more powerful actuators with a bigger size can be used to achieve higher torques and tip forces.

Moreover, the proposed design is fully-backdrivable which has two important benefits; first, the mechanism can be safely used for safety-critical applications such as surgery, where the manipulator can be extracted out of the patient body without causing any damage to the neighboring tissues in case of a mechanical or electrical failure. Secondly, the backdrivability feature results in a highly force-reflective design [69, 70], which is considered a desirable characteristic for a system designed to incorporate force-feedback [71–73].

On the other hand, with the increased number of links and joints, the dynamic performance of the mechanism may be reduced. Similarly, due to an increased number of passive prismatic joints, the manipulator design would require a close attention to minimize the friction at respective joints in a physical implementation of the mechanism. Given the less critical nature of these issues, we believe the proposed design offers significant advantages in terms of reduced footprint and optimized kinematic performance over the existing 2-DoF planar RCM mechanisms.

5.6 Summary

This chapter presented a novel 2-DoF planar remote center of motion mechanism design which offers a significantly smaller footprint than the existing state-of-the-art designs. The proposed mechanism provides the two most important DoFs required for surgery through its novel kinematic design and, therefore, avoids the potential performance issues caused by the *external means*, such as cable-pulleys or actuators directly mounted on the distal-end of a manipulator. The RCM capability of the mechanism is verified. Its suitability for MIS is determined through workspace analysis, which shows that the proposed design meets the required workspace requirements for the target application, MIS. It is also shown that the proposed design offers a 1.6 times smaller footprint than an existing design [41], without sacrificing its kinematic performance.

Furthermore, the optimization results show that the best performance of the design in terms of manipulability and surgical tool translation is achieved for a geometrically symmetric design, i.e. $l_1 = l_2 = l_3 = l_4$. The proposed design is fully-backdrivable, which adds an important feature for the safety-critical surgical applications. The design has high force-reflection capabilities which could be helpful to introduce haptic feedback in the surgical manipulator. Additionally, the proposed design offers a compact distal end which is ideal for applications where multiple manipulators are required to operate in close proximity, such as the robot-assisted MIS.

In the next chapter, we will focus on the aspects of haptics to solve the problem of a lack of compatibility of the existing haptic devices and study the prospects of using a wearable hand-grounded kinesthetic device for virtual reality and robot teleoperation applications.

THIS PAGE INTENTIONALLY LEFT BLANK

Chapter 6

Haptic Device Design and Evaluation

In the foregoing part of this thesis, we focused on the problems related to the robotic manipulator designs and tried to offer solutions by proposing new multi-DoFs RCM designs that offer superior kinematic and operational performance. In the forthcoming part, we will focus to address the challenges related to use of haptic feedback in robotic surgery.

6.1 Introduction

6.1.1 Motivation

The majority of the existing haptic devices providing kinesthetic feedback are world grounded [74]. They offer numerous advantages like high forces and torques, many degrees of freedom (DoF), and a wide dynamic range. These features allow such devices to provide more realistic haptic renderings compared to tactile haptic devices that only stimulate the skin. However, the world-grounded kinesthetic haptic devices generally have a large footprint as well as limited portability and wearability, which limits their application and effectiveness for many virtual and real-world applications. World-grounded haptic devices also offer a limited range of motion to the user due to the scaling of weight and friction with increased size [75].

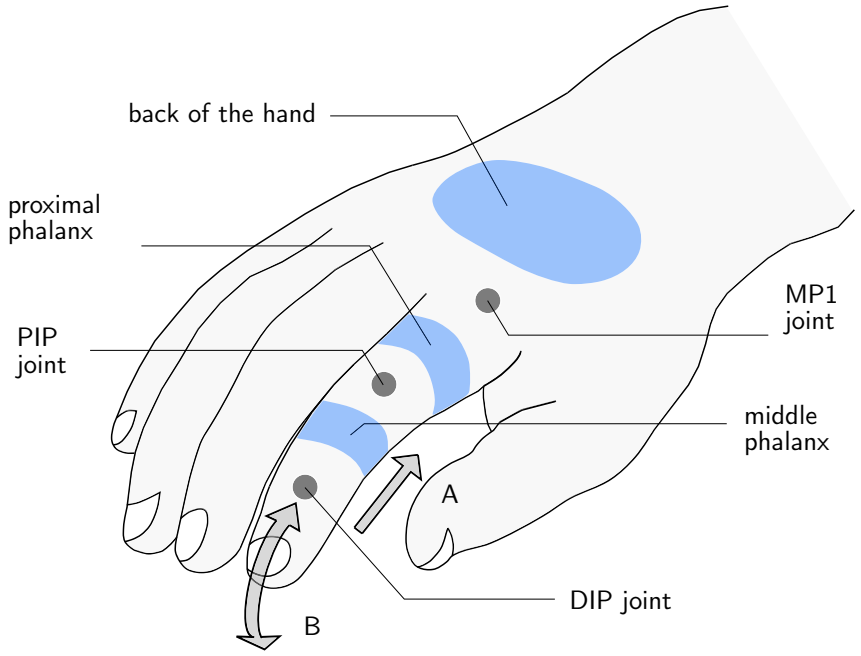

Figure 6-1: Three potential grounding locations on the user's hand: Back of the hand, Proximal Phalanx, and Middle Phalanx of the index finger. Arrows indicate directions of applied kinesthetic feedback on the fingertip: (A) along the finger axis and (B) in flexion-extension.

6.1.2 Issue with the exisiting wearable haptic technology

On the other hand, wearable haptic devices must be portable and typically offer a large range of motion. But, majority of the existing wearable haptic devices are tactile in nature and provide feedback in the form of vibration or skin deformation. They are commonly grounded against the user's fingertip or the nearby region [74]. Though tactile feedback is capable of providing directional cues and aiding users in completing various tasks, it may not be sufficient to perform certain tasks, such as the suture knot-tying in robot-assisted surgery [76], and manipulating objects in virtual reality [77]. As demonstrated by Suchoski et al. [75] in their study, kinesthetic feedback is capable to give more sensitive haptic information to carry out a grasp-and-lift task than the skin deformation feedback (a form of tactile feedback). Similarly, the role of kinesthetic (force) feedback in surgical training and skill development looks very promising [76].

Kinesthetic haptic devices, that are not world grounded but instead impart feedback by grounding forces against the user's hand (*hand-grounded haptic devices*), provide a solution to challenges of portability, wearability and limited workspace in kinesthetic haptic devices. As noted by Pacchierotti et al. [74], the primary advantage of wearable kinesthetic devices

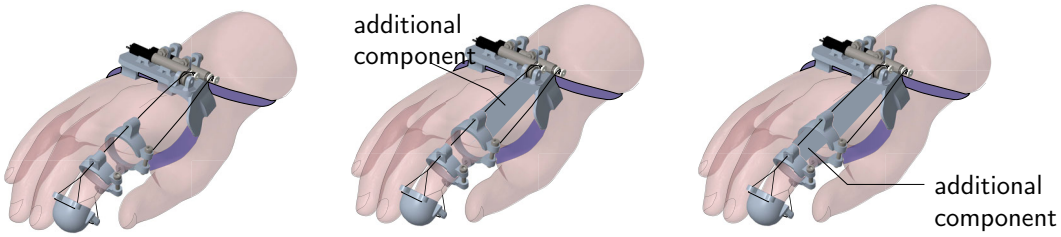

(a) (b) (c)

Figure 6-2: Device design with three different grounding modes: (a) Grounding location is back of the hand, (b) Proximal phalanx is the grounding location, (c) Grounding locations is the Middle phalanx of index finger. In mode (b) and (c), the finger rings are rigidly attached with the base part.

is their small form factor as compared to the world-grounded devices. Similarly, body-grounded kinesthetic devices, i.e. Exoskeletons, could be another potential solution, but they generally encumber the user movement and are difficult to don and doff. However, designing these hand or body-grounded devices is challenging due to the need for increased forces/torques and number of degrees-of-freedom (DoF) in comparison to the fingertip tactile devices. Additionally, the effects of hand-grounded kinesthetic feedback on users' perception and haptic experience are still unknown.

There exist numerous examples of hand-grounded kinesthetic haptic devices, including [78–99]. These devices are either grounded against the back of the hand [78–92], act like a glove [93–95], are grounded against the user's palm [96, 97], or are grounded against the user's fingers [98, 99]. To the best of our knowledge, there exists no device that can be grounded against different locations on the user's hand or a study that explains the effect of different grounding locations on the user's haptic perception and qualitative experience with kinesthetic (force) feedback.

6.1.3 Objectives

We aim to study the effects of different hand-grounding locations on a user's haptic perception by providing kinesthetic feedback on the user's index finger tip. For this purpose, a wearable 2-DoF haptic device is designed that can provide kinesthetic feedback grounded at three different regions of the user's hand (Fig. 6-1): (i) back of the hand, (ii) proximal phalanx of the index finger, and (iii) middle phalanx of the index finger. The light-weight and modular design provides kinesthetic feedback in two directions: (A) along the index finger axis, and (B) in flexion-extension.

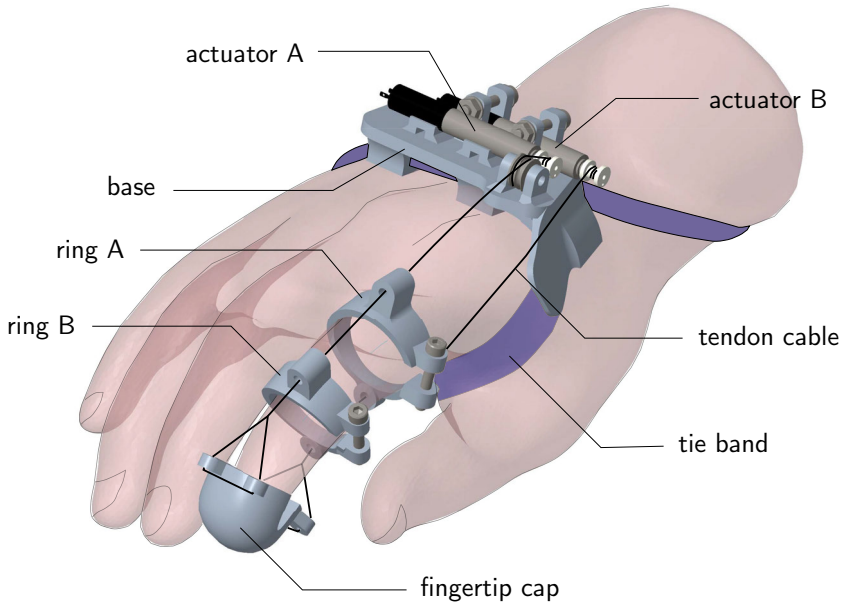

Figure 6-3: Design: The base is tied against the back of the hand. When tendon cables are pulled/released by actuators A and B, the fingertip cap provides kinesthetic feedback along the finger axis and/or in flexion-extension.

We aim to understand how different hand-grounding locations affect the user's haptic performance and overall experience. To identify the significance and impact of different hand-grounding locations, two psychophysical experiments are carried out using *the method of constant stimuli* [100] — one for each feedback direction. The participants were asked, in separate trials, to discriminate the stiffness of two virtual surfaces based on the kinesthetic feedback provided by the hand-grounded device. The Point of Subjective Equality (PSE) and Just Noticeable Difference (JND) were computed to measure the effective sensitivity and precision of the participants' perception of stiffness for each hand-grounding location, in both feedback directions. The PSE gives insight about the accuracy of the applied/perceived feedback, as it represents the point where the comparison stimulus (stiffness) is perceived by the user as identical to the standard stimulus. JND indicates the resolving power of a user and is defined as the minimum change in the stimulus value required to cause a perceptible increase in the sensation [100].

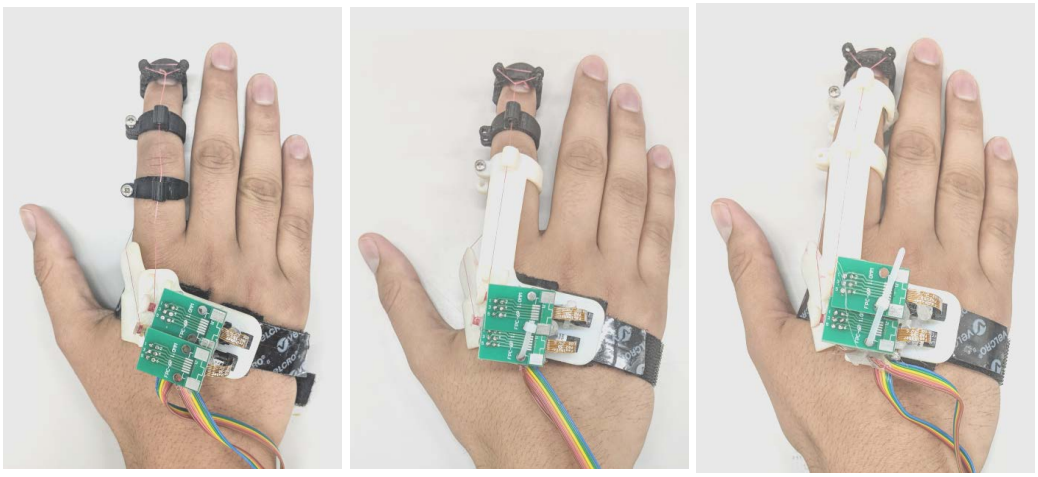

(a) (b) (c)

Figure 6-4: Modular versions of the wearable kinesthetic device with grounding locations: (a) Back of the hand, (b) Proximal Phalanx, and (c) Middle Phalanx

6.2 Proposed Haptic Device Design

6.2.1 Design Description

The device has a base (Fig. 6-3) that can be tied to the back of the user's hand using a hook-and-loop fastener. It has two rings (A and B) which are fitted to the proximal and middle phalanxes of the index finger. The fingertip cap is connected to actuators A and B through two cables, which route through the passage holes on rings A and B, as shown in Fig. 6-3. When both actuators A and B move in the same direction (clockwise or anti-clockwise), a flexion or extension movement at the finger is produced. When both actuators move in opposite directions, a pull force is generated along the finger axis.

To provide hand-grounded kinesthetic feedback at the fingertip, a number of grounding locations can be used. Fig. 6-1 shows the three grounding locations considered in this case: the back of the hand, proximal phalanx of the index finger, and middle phalanx region of the index finger. Another potential location, the palm region, was rejected because such an arrangement may affect the user's ability to open/close the hand and fingers.

To achieve different groundings, the device has three different modes. In mode A (Fig. 6-2(a)), the back of the hand acts as the grounding location. In mode B (Fig. 6-2(b)), the base is physically connected to the ring A at the proximal phalanx, providing grounding at this region. In mode C (Fig. 6-2(c)), the base is rigidly connected with both rings to provide grounding at the middle phalanx region. Different device modes enable execution of

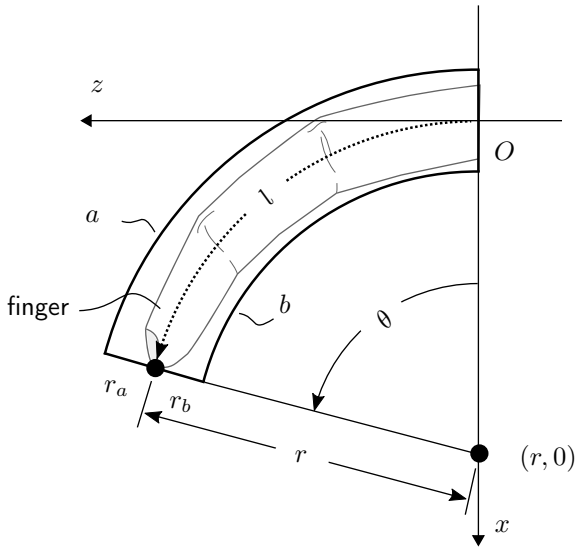

Figure 6-5: A simplified representation of the device's mechanism as a 2-D piece-wise constant-curvature tendon-driven manipulator. Tendon lengths (l_a, l_b), their respective distance from tip center-point (r_a, r_b), and the arc parameters: length (l) and radius (r), are used to determine the tip position and finger configuration in the $x - z$ plane.

different joints of the index finger in the flexion-extension direction. For example, in mode A, the torque is applied at all three joints (MP1, PIP, and DIP). In mode B, only PIP and DIP joints are executed. In mode C, the torque applies only at the DIP joint.

Based on its kinematic design and actuator specifications, the device can apply, in different modes, a maximum force of 28.9 N along the finger axis and a torque in the range of 80 to 300 N-mm at the fingertip. It is driven by two Faulhaber 0615 4,5S DC-micromotors with 256:1 gearboxes, and 50-counts-per-revolution optical encoders are used for position sensing. The device prototypes with different grounding modes (Fig. 6-4) weigh 31, 43, and 49 grams, respectively.

6.2.2 Kinematics

The device renders forces on the user's index finger by controlling the tendon lengths. To calculate the position and configuration of the finger, we use a robot-independent kinematic mapping between the actuator space and the task space. The obtained homogeneous transformation remains identical for all three grounding modes of our device. It is assumed that the device's tendons, when fit to the user index finger, exhibit a continuum-curve shape. The geometry of this curve allows determination of the tip position and configuration of the finger. Fig. 6-5 shows a simplified representation of the haptic device in such a scheme.

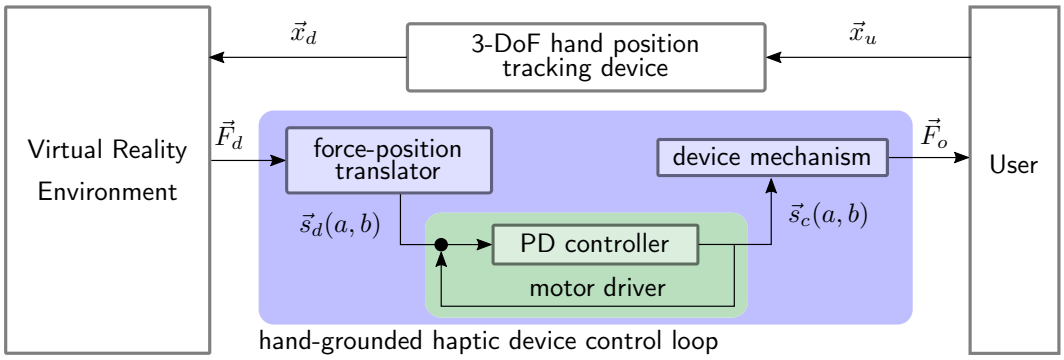

Figure 6-6: Block diagram of the controller used for rendering force on the user's fingertip. The hand position is tracked by a 3-DoF device, and the interaction forces are calculated as the desired force. Forces applied by the hand-grounded device end-effector on the fingertip through tendon displacements are regulated using a proportional-derivative (PD) controller.

As the haptic device aims to provide kinesthetic feedback in two directions (along the finger axis, and in the finger's flexion-extension direction), the kinematic mapping between the inertial frame (O) and the fingertip ($p(x,z)$) is described in a 2-D ($x-z$) plane. Tendon lengths (l_a, l_b), their respective distance from tip center-point (r_a, r_b), and the arc parameters, namely length (l) and radius (r), are used to determine the tip position and figure configuration in $x-z$ plane. The position of fingertip can be expressed as,

$$p(x,z) = [r(1-\cos\theta), r\sin\theta]^T . \tag{6.1}$$

The homogeneous transformation for tendons a and b, from O to $p_a(x,z)$ and $p_b(x,z)$ respectively, is

$$T_j = \begin{bmatrix} \cos(\theta) & 0 & \sin(\theta) & p_{xj} \\ 0 & 1 & 0 & 0 \\ -\sin(\theta) & 0 & \cos(\theta) & p_{zj} \\ 0 & 0 & 0 & 1 \end{bmatrix}, \quad (j = a, b), \tag{6.2}$$

$$p_{xj} = \left(\frac{l}{\theta} \pm r_j\right)(1-\cos\theta), \quad (j = a, b), \tag{6.3}$$

$$p_{zj} = \left(\frac{l}{\theta} \pm r_j\right)\sin\theta, \quad (j = a, b). \tag{6.4}$$

The displacements of tendons a and b can be expressed in terms of arc radius and angles

as

$$s_a = (r + r_a)(\theta_o - \theta_t), \tag{6.5}$$

$$s_b = (r - r_b)(\theta_o - \theta_t). \tag{6.6}$$

where θ_o is the initial angle angle of tendon a and θ_t represents the tendon angle at time t.

6.3 Haptic Device Control

Using the tendon displacements (6.5) and (6.6), a separate control is implemented for each of the actuators to apply force and control the user's finger configuration. Fig. 6-6 shows the block diagram of the control in the virtual reality setup. The control of the 2-DoF kinesthetic device was achieved by using a Nucleo-F446ZE board by STMicroelectronics^{TM}connected to a Desktop computer via USB. The microcontroller reads the encoders of the motors and receives the desired force from the virtual environment sent using a PC's serial port. Using this information, it calculates the desired torque output of the motors. The control loop runs at a frequency of approximately 1 kHz. The CHAI3D framework was used to render the 3-D virtual reality environment [101] using the god-object algorithm [102] to calculate desired interaction force. The user can move the cursor (red sphere in Fig. 6-7(a) & (b)) in 3-D space. Because the wearable device has only 2 DoFs, the third dimension does not give any force feedback to the user. Given the nature of the tasks in the user studies, the third dimension (y-axis) is not required to display the force feedback.

The user's hand position ($\vec{x_u}$) is tracked using a Phantom Omni haptic device (set up to provide no haptic feedback, just position tracking) from SensAble Technologies, Inc. and sent to the virtual environment as $\vec{x_d}$. The resulting interaction force command from the virtual environment ($\vec{F_d}$) is calculated in the computer and then fed to the hand-grounded haptic device. The device then uses a mapping between the force magnitude and the device tip position (force-position translator) to output the desired tip position to the PD controller which, using the encoders mounted on each motor shaft, can estimate the current tip position and configuration and outputs the appropriate tendon displacements ($\vec{s_c}(a, b)$) to the device's motors. As the tendons shorten, the user's finger tip is moved to the right position, allowing him/her to feel a force.

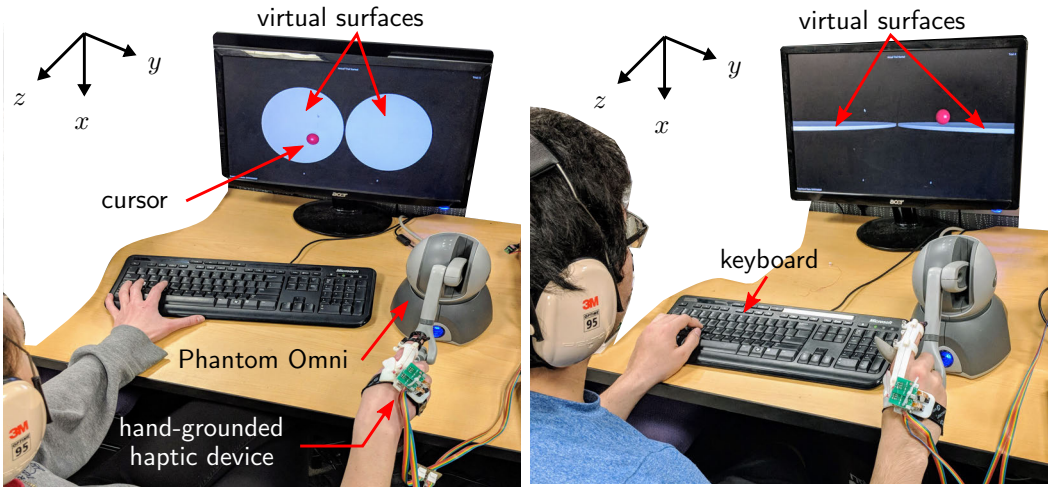

(a) (b)

Figure 6-7: Experimental setup: A user interacts with the virtual environment through a 3-DoF hand position tracking device (Phantom Omni). The new hand-grounded haptic device provides kinesthetic feedback, and a visual display shows the virtual environment. Participants receive force feedback by touching the two virtual surfaces, one carrying the reference stiffness and the other comparison stiffness in a random order. Participants are required to discriminate the stiffness based on the kinesthetic feedback and record their choice through key presses. (a) Study A (the feedback is rendered along the finger-axis) (b) Study B (the feedback is rendered along flexion-extension movements).

The PD controller error and the control law are

$$e(t) = y(t) - r(t), \tag{6.7}$$

$$U = K_P e + K_D \frac{d}{dt} e, \tag{6.8}$$

where, K_P represents the proportional gain and K_D is the derivative gain. $e(t)$ is the position error, $y(t)$ represents the motor shaft position, and $r(t)$ is the reference position calculated from the desired tendon displacements ($\vec{s_d}(a, b)$ in Fig. 6-6).

6.4 User Study for Experimental Evaluation

To evaluate the effects of the three different hand-grounding locations on the user's haptic perception and experience, we conducted two separate user studies (Study A & Study B); one for each haptic feedback DoF provided by the hand-grounded device. In Study A, the kinesthetic feedback is provided along the axis of the user's index finger. In Study B, the feedback is provided along the flexion-extension movement of the finger. The purpose of

evaluating each feedback DoF separately is to develop a clear understanding of the relation between the hand-grounding location and the corresponding feedback direction.

6.4.1 Study A: Feedback Along the Finger Axis

Experimental Setup

13 subjects (9 males and 4 females) participated in this study, which was approved by the Stanford University Institutional Review Board. The metrics were PSE and JND of stiffness perception while the hand-grounded device was set up for each of the three grounding locations (back of the hand, proximal, and middle phalanx of the index finger). All subjects participated in the experiment after giving informed consent, under a protocol approved by the Stanford University Institutional Review Board. The participants used the hand-grounded haptic device on their right hand and performed tasks in a virtual environment, while holding the stylus of the Phantom Omni device in the same hand (Fig. 6-7(a)). A pilot study was conducted to determine a convenient posture to hold the Phantom Omni stylus while the kinesthetic device is donned to the index finger. In the user studies, the participants were instructed to hold the Phantom Omni device in that predefined way to make sure that its stylus does not come into contact with the wearable kinesthetic device.

Experimental Procedure

Each participant used the haptic device configured for each of the three hand-grounding locations, in a predetermined order to minimize the effect of selection bias. As mentioned earlier, a Phantom Omni device was used to track the user hand position during the experiments as shown in Fig. 6-7(a). The Phantom Omni only determined the user hand position, while the kinesthetic feedback was rendered by the hand-grounded haptic device. Participants were wore ear protection to suppress the motor noise in order to avoid sound cues. After the experiments were completed, the participants rated the realism of haptic feedback and comfort/ease-of-use for all three devices with different hand-grounding locations on a scale of 1-7: 1 meaning 'not real' and 7 meaning 'real', or 1 for 'not comfortable' and 7 for 'comfortable.' The realism was with respect to the users' feeling as if they would be pressing against a very smooth real surface using their right-hand's index finger.

Table 6.1: Results of the two psychophysical experiments for stiffness discrimination. In Study A, the hand-grounded haptic device provided feedback along the axis of the finger with three different grounding locations. In Study B, the feedback direction was flexion extension movement of the index finger.

Grounding Location		Back of the Hand		Proximal Phalanx		Mid Phalanx	
	Subject No.	PSE (N/m)	JND (N/m)	PSE (N/m)	JND (N/m)	PSE (N/m)	JND (N/m)
Study A	1	154.42	57.15	150.74	47.35	120.34	41.32
	2	111.17	9.86	107.58	17.44	103.37	6.2
	3	139.75	48.5	129.95	34.27	81.3	7.32
	4	87.56	6.07	92.95	5.72	102.27	20.24
	5	98.62	32.37	85.2	6.79	114.85	19.04
	6	113.23	13.08	104.68	25.28	100.74	20.1
	7	99.6	13.21	108.99	7.97	94.68	9.48
	8	118.75	46.88	128	31.13	109.11	38.95
	9	115.5	20.23	103.4	10.16	105.51	19.72
	10	114.64	12.93	103.46	12.15	116.09	19
	11	85.87	7.32	108.22	12.65	117.25	17.41
	12	92.94	6.66	114.14	22.17	91.54	15.65
	Mean	111.004	22.855	111.442	19.423	104.754	19.536
	Std. Dev.	19.581	17.677	16.843	12.404	11.178	10.411
Study B	1	96.06	0.17	101.2	12.26	103.8	13.75
	2	92.71	13.51	104.59	13.02	92.79	8.64
	3	125.72	40.06	94.9	28.36	121.88	45.98
	4	104.87	6.41	98.32	14.36	87.34	6.75
	5	115.52	41.74	114.25	40.84	102.2	20
	6	122.16	33.52	90.2	16.44	119.91	16.88
	7	121.54	20.98	116.83	36.64	125.8	64.77
	8	105.76	10.69	108.89	11.67	104.6	26.4
	9	98.85	25.9	100	16.83	117.3	25.28
	10	99.45	41.48	95.07	22.3	104.98	24.18
	11	138.96	41.62	127	30.4	122.64	24.03
	12	113.34	38.78	95.35	45.78	120.79	60.43
	Mean	111.245	26.238	103.883	24.075	110.336	28.091
	Std. Dev.	13.426	14.761	10.435	11.520	12.181	18.222

Method

We conducted a *two-alternative forced-choice* experiment following the *method of constant stimuli* [100]. Subjects were asked to freely explore and press against the two virtual surfaces shown on the virtual environment display and state which surface felt stiffer. In each trial, one surface presented a reference stiffness value while the other presented a comparison stiffness value. The reference stiffness value was selected to be 100.0 N/m. The reference value was included as one comparison value, and the other comparison values were then chosen to be equally spaced: 10, 28, 46, 64, 82, 100, 118, 136, 154, 172, and 190 N/m.

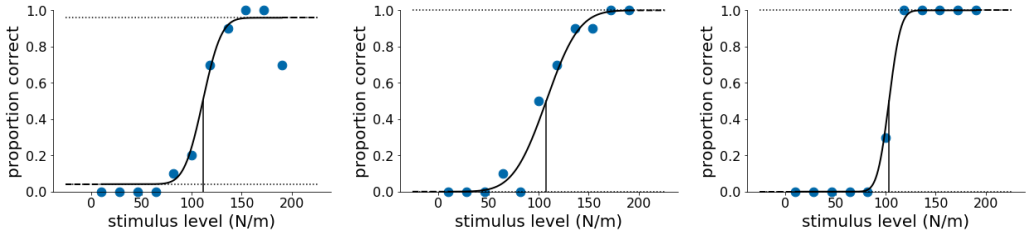

(i) Back of the hand (ii) Proximal Phalanx (iii) Middle Phalanx

Figure 6-8: Example psychophysical data and psychometric function fits for a representative subject in Study A, with grounding locations: (i) back of the hand, (ii) proximal phalanx, and (iii) middle phalanx of the index finger. Each data point represents the 'yes' proportion of the user responses over 10 trials. The user identified the difference between the reference and comparison stimulus values correctly 90 % of the time for grounding location (i), 94 % of the time for location (ii), and 98 % of the times for location (iii).

Each of the eleven comparison values was presented ten times in random order for each of the three hand-grounded haptic devices over the course of one study. Each participant completed a total of 110 trials for each grounding mode (330 trials for the entire study). The participants used the kinesthetic feedback from the hand-grounded device to explore the virtual surfaces until a decision was made; they recorded their responses by pressing designated keyboard keys, corresponding to which virtual surface they thought felt stiffer. Subject responses and force/torque data were recorded after every trial. There was no time limit for each trial, and participants were asked to make their best guess if the decision seemed too difficult. Subjects were given an optional two-minute break after every fifty-five trials, and a ten-minute break after the completion of each grounding mode.

6.4.2 Study B: Feedback in the Flexion-Extension Direction

In study B, the kinesthetic feedback was rendered along the flexion extension movement direction of the index finger. A total of 14 subjects (9 males and 5 females) participated, and the study was approved by the Stanford University Institutional Review Board. The procedure was the same as in Study A. However, in Study B the virtual surfaces were presented lying in the horizontal plane (Fig. 6-7(b)) to make the haptic feedback intuitive for the user.

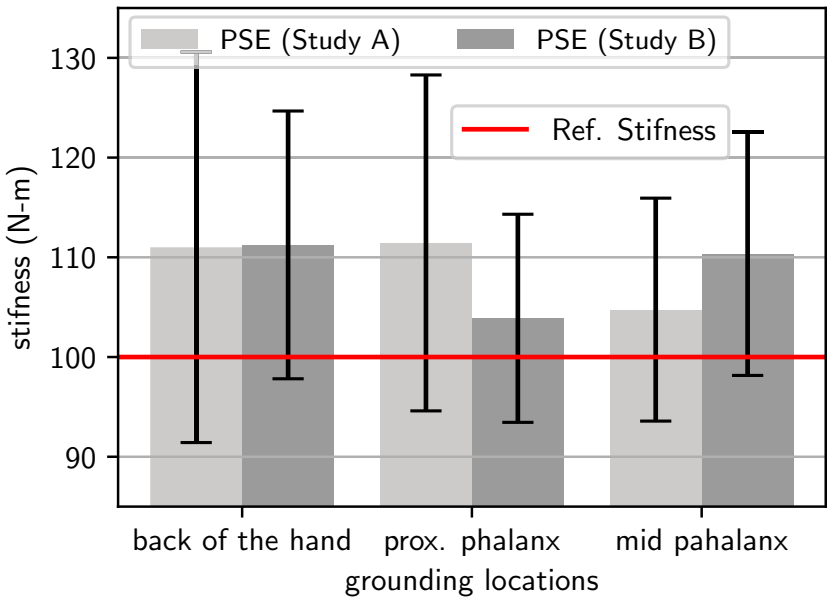

Figure 6-9: Point of Subjective Equality (PSE) for both feedback DoFs (Study A and B) against each of the three considered hand-grounding locations. Error bars indicate the standard deviation.

6.5 Results & Discussion

For both user studies, we determined the number of times each participant responded that the comparison value of stiffness was greater than the reference stiffness value. A psychometric function was then fit for each participant's response data to plot a psychometric curve, using the python-psignifit 4 library (https://github.com/wichmann-lab/python-psignifit). Data from twenty-four out of the twenty-seven subjects fit sufficiently to psychometric functions and the mean JNDs and PSEs for both experiments were determined. Example plots for a representative subject are shown in Fig. 6-8. Three relevant values: the PSE, the stimulus value corresponding to a proportion of 0.25 (J_{25}), and the stimulus value corresponding to a proportion of 0.75 (J_{75}) were determined. The JND is defined as the mean of the differences between the PSE and the two J values J_{25} and J_{75}:

$$JND = \frac{(PSE - J_{25}) + (J_{75} - PSE)}{2}. \tag{6.9}$$

The PSE and JND results of the psychophysical experiments for both studies are sum-

marized in Table 1. Because these studies use a single reference force, the Weber Fractions (WFs) are simply the JNDs scaled by the reference value. Therefore, we do not report WF separately.

6.5.1 Study A

In Study A, the best average PSE (closer to the reference value) for stiffness perception among all three grounding locations is found for the middle phalanx location of the index finger (104.75 N/m), shown in Fig. 6-9. This indicates that the grounding location closer to the fingertip helps users to perceive the stiffness more accurately. This is also supported by the user ratings for the realism of kinesthetic feedback, as shown in Fig. 6-11. The smallest average JND was found for grounding at proximal phalanx (19.42 N/m), which is closely followed by average JND values for grounding location at the proximal phalanx (19.54 N/m). Like the PSE, the average JND showed largest value for back of the hand grounding location (see Fig. 6-10). This indicates that the proximal and middle phalanx are preferable locations, in the given order, to have a more realistic and accurate feedback perception. However, the user ratings for the comfort and ease-of-use indicate that the back of the hand is a more desirable grounding location.

6.5.2 Study B

In Study B, the best average PSE (closer to the reference value) for stiffness perception among all three grounding locations is found in the grounding at the proximal phalanx of the index finger (103.88 N/m), shown in Fig. 6-9. This grounding location also results in the smallest average JND value (24.07 N/m) among all three grounding locations. The user ratings for kinesthetic feedback realism and the comfort/ease of use, as show in Fig. 6-11, also rate this location as the best to impart most realistic and comfortable haptic experience. The second best location in terms of average JND value is the back of the hand. This holds for the feedback realism ratings as well. The grounding location with least realistic feedback ratings and largest average JND (28.09 N/m) was the proximal phalanx location.

If we compare the average JND values across both studies, the values for feedback along the finger-axis (Study A) are significantly smaller than that of the feedback along flexion-extension direction (study B). This indicates that the haptic device was able to provide better haptic feedback in case of Study A, i.e. along the axis of the index-finger. The

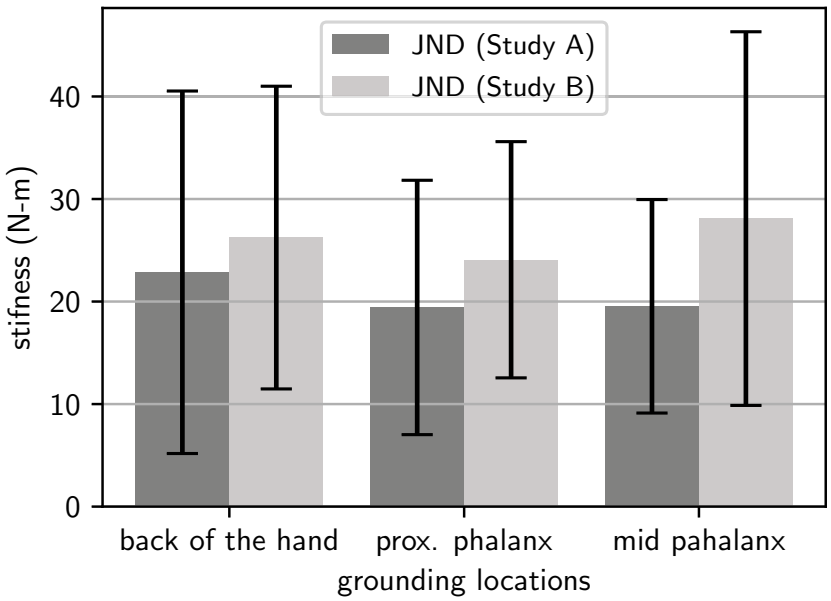

Figure 6-10: Just Noticeable Differences (JNDs) for both feedback DoFs (Study A and B) against each considered hand-grounding locations. Error bars indicate the standard deviation.

reason for this probably relates to the simpler nature of this feedback direction where the finger configuration remains unchanged during all modes. However, the realism and comfort ratings show a distinct pattern; realism is higher for Study B (kinesthetic feedback along flexion-extension) when the grounding locations are the back of the hand and proximal phalanx. The realism in case of Study A is higher than that of the B when grounding location is middle phalanx. This again depends on the different nature of the second feedback DoF, where the finger configuration has to change in order to render a torque at the finer joints. The use of the Phantom Omni for tracking may introduce some passive forces that introduce variance in the study. Despite this, we observed significant performance differences among the studied grounding locations.

On the other hand, the comfort/ease-of-use ratings are higher for Study A than B, when the grounding locations are the back of the hand and the middle phalanx, respectively. The feedback in flexion-extension movement (Study B) has shown higher comfort ratings than for the finger-axis direction (Study A) when grounding is set as the proximal phalanx region. The highest comfort rating among all grounding locations across both studies is given to the proximal phalanx, and that is for the feedback along the flexion-extension

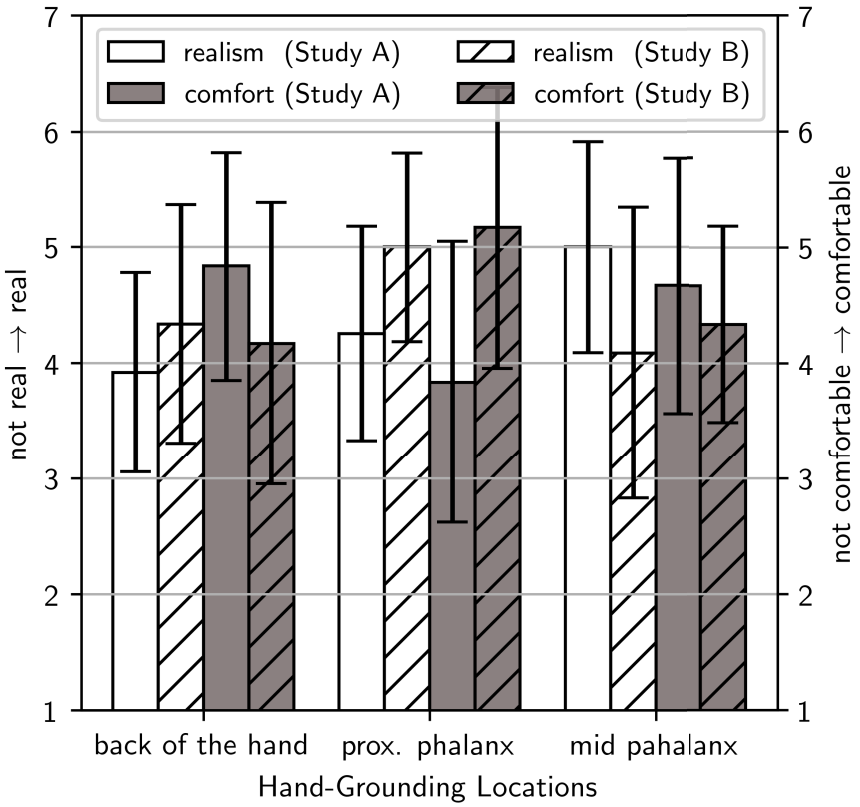

Figure 6-11: Mean user ratings for the realism of feedback and comfort/ease-of-use against each of the three hand-grounding locations. Error bars indicate standard deviations.

movement. Similarly, the highest comfort rating is given to the same grounding location, i.e., proximal phalanx, across both studies, and that too is for the feedback along flexion-extension direction.

6.6 Summary

A novel hand-grounded kinesthetic feedback device was created for studying the effect of different grounding locations on the user's haptic experience. The device can provide kinesthetic feedback along the user's index finger, and in its flexion-extension movement direction. Two psychophysical experiments – one for each feedback DoF – were conducted to evaluate the user's haptic performance and experience. It is shown that the choice of grounding-location in wearable haptic devices has significant impact over the user haptic perception of stiffness. The realism of the haptic feedback increases, while the comfort level

decrease, as the grounding location moves closer to the fingertip. The relationship between the grounding-location and user haptic perception is similar in both feedback directions. If the design objective is to achieve maximum comfort, feedback realism, and best haptic perception in both DoFs simultaneously, it is recommended to have grounding at the proximal phalanx region of the finger.

These findings about the choice and impact of different hand-grounding locations give important insights for designing next-generation wearable kinesthetic devices, and to have better performance in a wide range of applications, such as virtual reality and robot teleoperation.

THIS PAGE INTENTIONALLY LEFT BLANK

Chapter 7

Surgical Robot Design & Teleoperation Scheme

In the foregoing chapters, we have proposed multi-DoF RCM designs that offer superior kinematic and operational performance. We have also presented designs of a wearable and hand-grounded kinesthetic haptic device. In this chapter, we will present the design of surgical manipulator based on the proposed RCM mechanisms. We will describe a teleoperation scheme to achieve safer haptic feedback in surgical robotic systems.

7.1 CAD Design

7.1.1 Manipulator Design

A CAD design based on the RCM design presented in Chap. 5 is shown in Fig. 7-1. A surgical tool is attached to the distal end of the surgical manipulator. Base of the robot carries pitch and yaw DoFs drive mechanisms. Tool drive has actuators to operate the surgical tool tip DoFs. The manipulator can achieve all the basic DoFs required at the incision (tool-entry) point.

Fig. 7-2 shows size of the proposed surgical manipulator.

7.1.2 Approach of the Surgical Tool

The surgical tool, shown in Fig. 7-3b, has been designed after studying two approaches as shown below. In addition to previous requirements, surgical instrument needs to be;

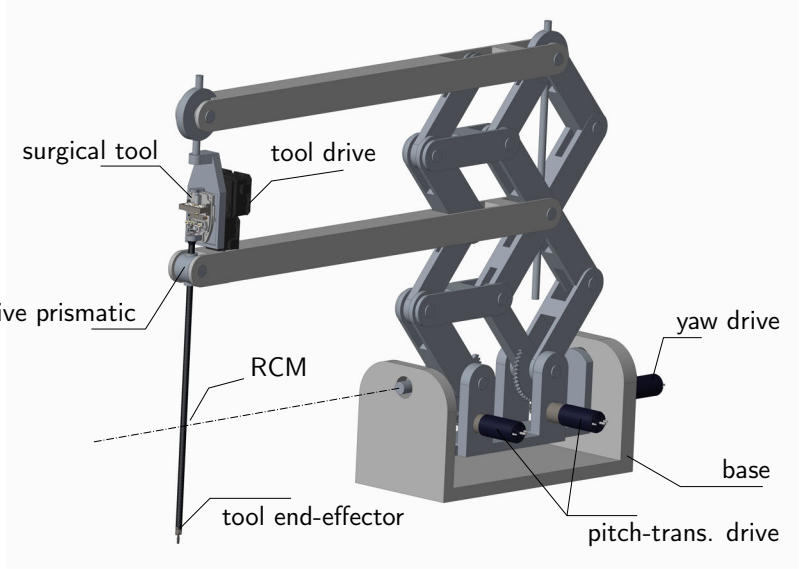

Figure 7-1: CAD Design: Based on the multi-DoF RCM presented (Chap. 5), the manipulator has a surgical tool to accomplish the desired surgical tasks.

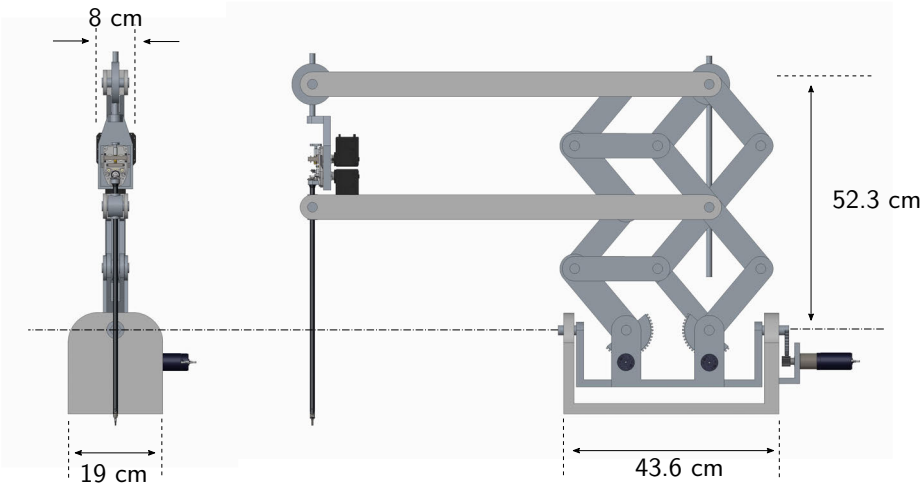

Figure 7-2: CAD design of the surgical manipulator showing size. The figure on left shows front view and lateral space covered by the robot. The right side figure shows height of the manipulator and length of its base.

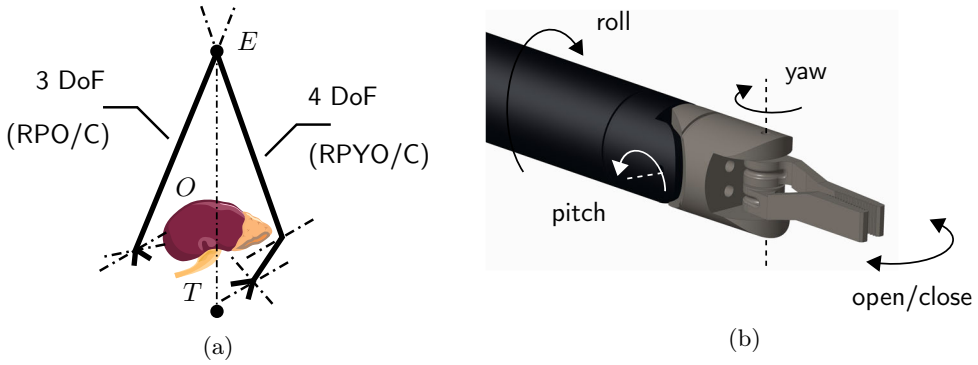

Figure 7-3: The proposed surgical tool design: (a) shows potential tool approaches inside the patient body. 4-DoF tool with Roll, Pitch, Yaw and Open/close (RPYO/C) capability offers better approach to the target organ (T) even from behind an obstacle (O). (b) The surgical tool DoFs.

1. Tool tube Dia: 5-13 mm (2.5 -5 mm for children)

2. 4 DoFs (at least) for dexterous tool manipulation

A 4-DoFs tool design is considered to approach any target even from behind an obstacle. The tube diameter is selected as 10 mm. Fig. 7-3 shows potential tool approaches inside the patient body. The 4-DoF tool with Roll, Pitch, Yaw and Open/Close (RPYO/C) capability offers better approach to the target organ (T) even from behind an obstacle (O). Fig. 7-3b denotes the surgical tool DoFs based on the RPYO/C approach.

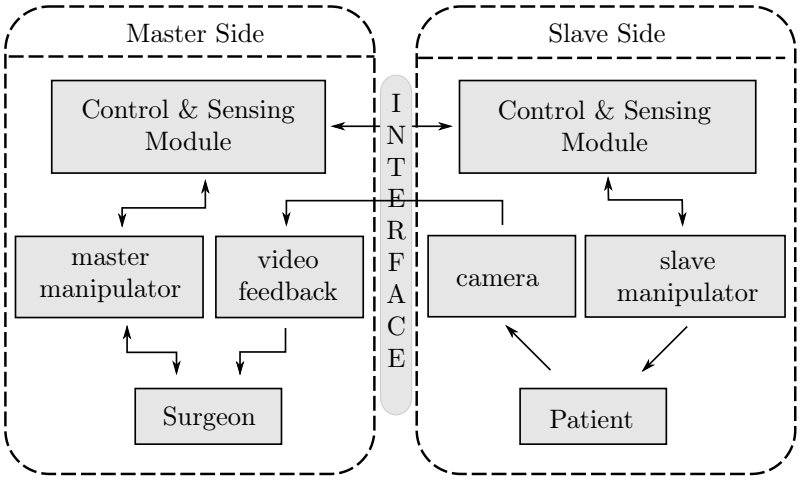

Figure 7-4: Layout of a surgical teleoperation system.

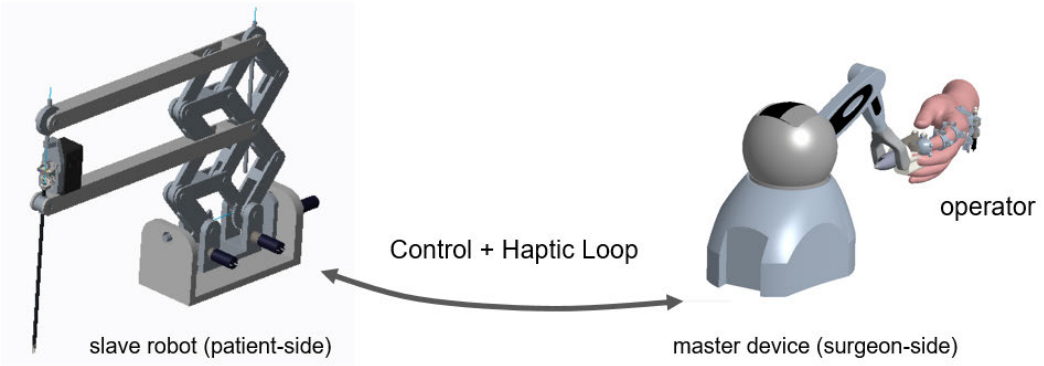

Figure 7-5: Layout of a typical surgical teleoperation system using haptic feedback. Such an approach suffers instability issues due to modeling errors which are unavoidable.

7.2 Master-Slave Teleoperation Scheme

7.2.1 Problems with the Master-Slave Teleopration Systems

In surgical teleoperation, typically a master device is used by operator (surgeon) to control the motion of the surgical manipulator (slave) on the patient side. A typical master slave teleoperation layout is shown in Fig. 7-4. The surgeon controls the slave manipulator (slave side) using the master manipulator device and video feedback showing the tip of the surgical tool inside the patient body. Such a system does not consider haptic feedback, and, therefore, is well known to have limited performance and user experience [76].

To increase the user performance haptic feedback is introduced between the master and slave side. A typical approach using such a scheme is shown in Fig. 7-5. Such an approach suffers instability issues due to modeling errors which are unavoidable. Consequently, there exists no practical system that can offer haptic feedback to increase the surgical performance.

7.2.2 Proposed Teleoperation System

We propose to avoid the intrinsic stability issue by separating the control and haptic loops using a wearable hand-grounded haptic device. A separation between the control loop (between master slave devices) and haptic loop (between wearable haptic device and slave manipulator) circumvents the issue of intrinsic instability.

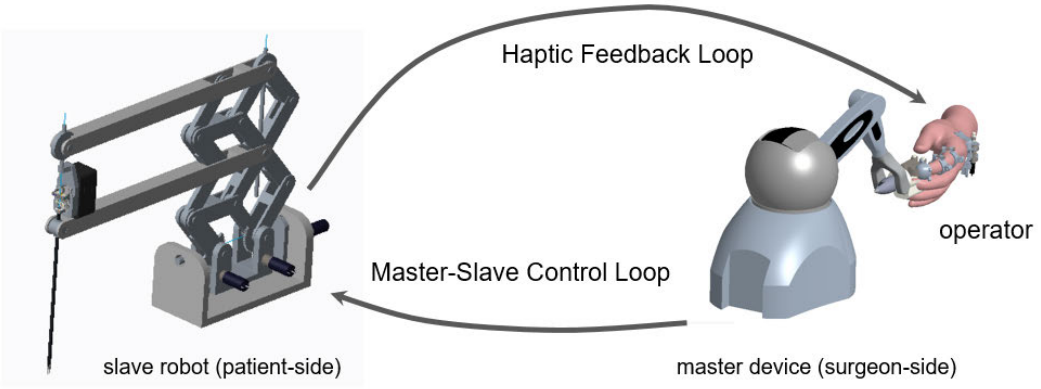

Figure 7-6: Proposed teleoperation system: A separation between the control loop (between master slave devices) and haptic loop (between wearable haptic device and slave manipulator) circumvents the issue of intrinsic instability.

7.3 Summary

In this chapter, the deisgn of multi-Dof slave manipulator equipped with a surgical tool is presented. Additionally, we propose a master-slave teleoperation system to use the hand-grounded kinesthetic device and the proposed robotic manipulator to achieve superior surgical performance and user experience. Contrary to the existing approaches employed in majority of the surgical systems where the control and haptic loops are implemented on same master device, we have proposed a separation of both loops by making use of wearable haptic device (to provide haptic feedback) and a master manipulator device (to track user-hand position and movement). Using this separation between the control and haptic loop, we intend to circumvent the intrinsic instability issues present in the current surgical systems.

Finally, a plan to experimentally evaluate the above proposed teleoperation scheme in order to analyze the user haptic experience and surgical performance is discussed.

THIS PAGE INTENTIONALLY LEFT BLANK

Chapter 8

Conclusion

To solve the critical problems related to the kinematic and operational performance of the current robotic technology, this research has proposed three new RCM based robotic manipulator designs. The proposed manipulator designs offer superior kinematic performance and have shown to satisfy the key surgical requirements, such as, remote center of motion and surgical workspace. A detailed kinematic analysis and design optimization has been carried out to accomplish the desired surgical tasks with enhanced kinematic performance and smallest possible size of the robot.

To solve the problem of providing a proper tool-entry angle in order to reduce the post-operative pain, the realized manipulator's capabilities have been experimentally evaluated. It is shown that the proposed design can accomplish all the required surgical tasks, such as, pick and place, grasping, and object manipulation, while being able to maintain a proper tool-entry to the patient body.

To address the problem of limited DoFs and dependence on *external means*, such as, cable-pulleys or actuators at distal end, two novel multi-DoF RCM designs have been proposed. The proposed designs can achieve the two most important DoFs required for surgery through their mechanism design. They do not require any *external means* to achieve tool translation DoF, and, therefore, offer superior kinematic and operational performance than the existing 1-DoF planar surgical robots. For improved compatibility with the surgical environment, an RCM mechanism design is presented that offers high kinematic performance but with significantly smaller footprint. To ensure maximum kinematic performance inside the required surgical workspace, we have carried out design optimization to determine the smallest possible size of the manipulator mechanism. Compact distal-end and smaller foot-

print make the proposed designs ideal for applications requiring multiple manipulators to operate in close proximity, such as Robot-assisted Minimally Invasive Surgery (RMIS).

To improve the overall surgical performance and operator's experience, design of three hand-grounded kinesthetic haptic devices is proposed. The proposed haptic devices are designed to be wearable in order to make them compatible with the surgical needs and, more importantly, they provide a reliable kinesthetic feedback to the user's fingertip to gain intuitive surgical experience. We have investigated three different ground locations on the user hand; (i) back of the hand, (ii) proximal phalanx, (iii) and middle phalanx of the index finger, respectively, to study the potential of using hand-grounded kinesthetic feedback in robotic surgery. Due to lack of any existing research to evaluate the effects of different hand-grounding locations on user haptic performance and experience, we conducted two user studies to show that the hand-grounded kinesthetic feedback can be efficiently applied to perform certain tasks, such as surgical exploration and stiffness discrimination. It is further concluded that the choice of grounding-locations has profound impact on the user haptic performance and experience. These findings provide important insights about the use of hand-grounded haptic feedback and the impact of grounding location on the user haptic experience.

To offer practical (safe) and functional haptic feedback, a master-slave teleoperation approach has been proposed. It is argued that the proposed master slave approach using the hand-grounded kinesthetic device and the proposed robotic manipulators can yield superior surgical performance and user experience. Contrary to the existing approaches employed in majority of the surgical systems where the control and haptic loops are implemented on same master device, the proposed approach emphasizes a separation of both loops by making use of wearable haptic device (to provide haptic feedback) and a master manipulator device (to track user-hand position and movement). Using this approach, the problem of instability in the control loop can be circumvented.

Contribution of this research on the aspects of manipulator design and hand-grounded kinesthetic haptics, and the subsequent findings as summarized above, are expected to play an important role to take the current surgical technology a step further where more featureful surgical robots with fully-functional haptic feedback may be realized.

8.1 Future Problems

This research has introduced a seemingly interesting solution to apply functional haptic feedback in a potentially safer way during the robotic surgery. In the future, there is a need to experimentally evaluate the above proposed teleoperation scheme in order to analyze the user haptic experience and surgical performance. We plan to interface the realized wearable haptic device with one of the surgical manipulator prototypes and perform experiments to evaluate the usefulness and safety of the envisaged master-slave system.

Considering the important role played by a master manipulator device to enhance the *useability* of a surgical robotic system, we plan to design and develop a new master manipulator device to be used in tandem with the hand-grounded wearable haptic device. It seems important to consider the evaluation of master-slave surgical system from the perspective of human-machine *useability* and ascertain the usefulness of the proposed devices and overall surgical system.

Another important aspect which needs deeper attention in the future is related to safety evaluation. Given the safety-critical applications of the proposed surgical manipulators and haptic devices, it is of prime importance to ensure the desired function with complete safety at all times. For this purpose, one good strategy would be to establish a industry-university collaboration where the people from industry with relevant experience in standardization and safety evaluation can help make the surgical systems safe and reliable to use in clinical settings.

Furthermore, the focus of this thesis has remained to solve the critical performance issues related to kinematic design of the existing surgical robots. In the future, we plan to realize a surgical manipulator based on the multi-DoF RCM design and optimize the dynamic performance of the surgical system.

THIS PAGE INTENTIONALLY LEFT BLANK

Appendix A

Proof: Conditions of Collinearity

In *alignment mechanism* (Fig. 4-5), let us define $\vec{r_1}$ and $\vec{r_2}$ as the position vectors of points A_2 and A_3 with respect to O_2 and their closed-loop equations can be written as,

$$r_1 = l_i u_i + l_{5i} w_{5i}, \quad r_2 = k_i l_i u_i + l_{6i} w_{6i}, \tag{A.1}$$

where $i = 5, 6$ $(0 < k < 1)$ and u_i, w_{5i}, w_{6i} are the respective direction vectors. The Cartesian position of A_2 and A_3 in XY-plane can be expressed as,

$$r_1 = [x_{A2} \quad y_{A2}]^T, \tag{A.2}$$

$$r_2 = [x_{A3} \quad y_{A3}]^T, \tag{A.3}$$

and,

$$u_i = [\cos\theta_{5i} \quad \sin\theta_{5i}]^T, \quad w_{5i} = [\cos\theta_{5i} \quad \sin\theta_{5i}]^T,$$
$$w_{6i} = [\cos\theta_{6i} \quad \sin\theta_{6i}]^T.$$

If we assume $\vec{r_1}$ and $\vec{r_2}$ as collinear vectors then their relationship can be expressed as $\vec{r_1} = \lambda \vec{r_2}$, where λ is a scalar multiple with value greater than one. Above relation can also be written as,

$$\begin{bmatrix} x_{A2} \\ y_{A2} \end{bmatrix} = \lambda \begin{bmatrix} x_{A3} \\ y_{A3} \end{bmatrix}. \tag{A.4}$$

If $x_{A2} = \lambda x_{A3}$ and $\lambda = y_{A2}/y_{A3}$, (A.4) can be expressed in terms of the ratios of the

Cartesian coordinates of A_2 and A_3.

$$x_{A2} : y_{A2} = x_{A3} : y_{A3}. \tag{A.5}$$

Equation (A.5) represents the necessary and sufficient condition of collinearity for $\vec{r_1}$ and $\vec{r_2}$. In order to find the above ratios, we rearrange and take norm of (A.1).

$$r_1^T r_1 + l_i^2 - 2l_i r_1^T u_i = l_{5i}^2, \tag{A.6}$$

$$r_2^T r_2 + (k_i l_i)^2 - 2k_i l_i r_2^T u_i = l_{6i}^2, \tag{A.7}$$

where $i = 5, 6$. Substituting expressions for r_1, r_2, u_i, w_{5i} and w_{6i} in above pair of equations,

$$\begin{aligned} 2l_i \cos\theta_i x_{A2} + 2l_i \sin\theta_i y_{A2} & \\ +(l_{5i}^2 - l_i^2 - x_{A2}^2 - y_{A2}^2) = 0, & \qquad \text{(A.8)} \\ 2k_i l_i \cos\theta_i x_{A3} + 2k_i l_i \sin\theta_i y_{A3} & \\ +(l_{6i}^2 - k_i^2 l_i^2 - x_{A3}^2 - y_{A3}^2) = 0. & \qquad \text{(A.9)} \end{aligned}$$

Eq. (A.8) represents two equations as $i = 5, 6$. Same is the case with (A.9). Solving both equations individually for $i = 5, 6$ results in,

$$\begin{aligned} 2(l_5 \cos\theta_5 - l_6 \cos\theta_6) x_{A2} + 2(l_5 \sin\theta_5 - l_6 \sin\theta_6) y_{A2} & \\ + (l_6^2 - l_5^2 + l_{55}^2 - l_{56}^2) = 0, & \qquad \text{(A.10)} \\ 2(k_5 l_5 \cos\theta_5 - k_6 l_6 \cos\theta_6) x_{A3} + 2(k_5 l_5 \sin\theta_5 - k_6 l_6 \sin\theta_6) y_{A3} & \\ + (l_{65}^2 - l_{66}^2 + k_6^2 l_6^2 - k_5^2 l_5^2) = 0. & \qquad \text{(A.11)} \end{aligned}$$

Eq. (A.10) and (A.11) represent the position of point A_2 and A_3 in terms of related link lengths and joint angles. Using both equations, the ratios of respective coordinates can be expressed as,

$$\frac{x_{A2}}{y_{A2}} = \frac{l_5^2 - l_6^2 + l_{56}^2 - l_{55}^2 - 2(l_5 \sin\theta_5 - l_6 \sin\theta_6)y_{A2}}{2(l_5 \cos\theta_5 - l_6 \cos\theta_6)y_{A2}}, \tag{A.12}$$

$$\frac{x_{A3}}{y_{A3}} = \frac{k_5^2 l_5^2 - k_6^2 l_6^2 + l_{66}^2 - l_{65}^2 - 2(k_5 l_5 \sin\theta_5 - k_6 l_6 \sin\theta_6)y_{A3}}{2(k_5 l_5 \cos\theta_5 - k_6 l_6 \cos\theta_6)y_{A3}}. \tag{A.13}$$

From (A.12) and (A.13), the conditions for which (A.5) holds true can be written as,

$$l_5^2 - l_6^2 = l_{55}^2 - l_{56}^2, \tag{A.14}$$

$$k_5^2 l_5^2 - k_6^2 l_6^2 = l_{65}^2 - l_{66}^2, \tag{A.15}$$

$$\frac{l_5 \sin\theta_5 - l_6 \sin\theta_6}{l_5 \cos\theta_5 - l_6 \cos\theta_6} = \frac{k_5 l_5 \sin\theta_5 - k_6 l_6 \sin\theta_6}{k_5 l_5 \cos\theta_5 - k_6 l_6 \cos\theta_6}. \tag{A.16}$$

If we suppose $l_5 \sin\theta_5 = a$, $l_6 \sin\theta_6 = b$, $l_5 \cos\theta_5 = c$, and $l_6 \cos\theta_6 = d$, the condition to satisfy (A.16) can be calculated from,

$$\frac{a-b}{c-d} = \frac{k_5 a - k_6 b}{k_5 c - k_6 d}, \tag{A.17}$$

which is $k_5 = k_6$. Considering

$$k_5 = k_6 = k, \tag{A.18}$$

and using (A.15) and (A.14), we can express,

$$k^2(l_{55}^2 - l_{56}^2) = l_{65}^2 - l_{66}^2. \tag{A.19}$$

Therefore, (A.18) and (A.19) represent a pair of sufficient conditions to make point A_2 and A_3 collinear independent of the pose of the mechanism. A similar conclusion for a slightly different mechanism form is presented in [39].

THIS PAGE INTENTIONALLY LEFT BLANK

Bibliography

[1] S. Nisar and O. Hasan, "Telesurgical robotics," *Encyclopedia of Information Science and Technology*, pp. 5482–5490, 2015.

[2] N. J. Soper, L. M. Brunt, and K. Kerbl, "Laparoscopic general surgery," *New England Journal of Medicine*, vol. 330, no. 6, pp. 409–419, 1994.

[3] A. Cuschieri, F. Dubois, J. Mouiel, P. Mouret, H. Becker, G. Buess, M. Trede, and H. Troidl, "The european experience with laparoscopic cholecystectomy," *The American journal of surgery*, vol. 161, no. 3, pp. 385–387, 1991.

[4] A. E. Park and T. H. Lee, "Evolution of minimally invasive surgery and its impact on surgical residency training," in *Minimally Invasive Surgical Oncology*. Springer, 2011, pp. 11–22.

[5] G. S. Guthart and J. K. Salisbury, "The intuitive/sup tm/telesurgery system: overview and application," in *Robotics and Automation, 2000. Proceedings. ICRA'00. IEEE International Conference on*, vol. 1. IEEE, 2000, pp. 618–621.

[6] A. J. Madhani and J. K. Salisbury, "Force-reflecting surgical instrument and positioning mechanism for performing minimally invasive surgery with enhanced dexterity and sensitivity," Sept. 15 1998, uS Patent 5,807,377.

[7] T. Hassan, A. Hameed, S. Nisar, N. Kamal, and O. Hasan, "Al-zahrawi: A telesurgical robotic system for minimal invasive surgery," *Systems Journal, IEEE*, vol. PP, no. 99, pp. 1–11, 2014.

[8] M. Cenk Çavusoglu, W. Williams, F. Tendick, and S. Shankar Sastry, "Robotics for telesurgery: second generation berkeley/ucsf laparoscopic telesurgical workstation and looking towards the future applications," *Industrial Robot: An International Journal*, vol. 30, no. 1, pp. 22–29, 2003.

[9] R. de la Torre, J. S. Scott, T. A. Howell, G. D. Hermann, D. Shields, R. T. Chang, N. Holmgren, and D. Willis, "Method and device for use in minimally invasive placement of space-occupying intragastric devices," Apr. 25 2006, uS Patent 7,033,373.

[10] D. Shichman, "Trocar adapter seal and method of use," Apr. 14 1992, uS Patent 5,104,383.

[11] D. T. Green and W. P. Young, "Safety device for trocars and surgical instruments therefor," July 14 1992, uS Patent 5,129,885.

[12] J. A. Hawks, J. Kunowski, and S. R. Platt, "In vivo demonstration of surgical task assistance using miniature robots," *Biomedical Engineering, IEEE Transactions on*, vol. 59, no. 10, pp. 2866–2873, 2012.

[13] H. JC, G. X, L. SR, and et al, "Comparative effectiveness of minimally invasive vs open radical prostatectomy," *JAMA*, vol. 302, no. 14, pp. 1557–1564, 2009. [Online]. Available: +http://dx.doi.org/10.1001/jama.2009.1451

[14] R. Verhage, E. Hazebroek, J. Boone, and R. Van Hillegersberg, "Minimally invasive surgery compared to open procedures in esophagectomy for cancer: a systematic review of the literature," *Minerva chirurgica*, vol. 64, no. 2, pp. 135–146, April 2009. [Online]. Available: http://europepmc.org/abstract/MED/19365314

[15] C. H. Kuo and J. S. Dai, "Robotics for minimally invasive surgery: a historical review from the perspective of kinematics," in *International symposium on history of machines and mechanisms*. Springer Science & Business Media, 2009, pp. 337–354.

[16] T. E. Chao, M. Mandigo, J. Opoku-Anane, and R. Maine, "Systematic review of laparoscopic surgery in low-and middle-income countries: benefits, challenges, and strategies," *Surgical endoscopy*, vol. 30, no. 1, pp. 1–10, 2016.

[17] S. Nisar and O. Hasan, "Telesurgical robotics and a kinematic perspective," in *Encyclopedia of Information Science and Technology, Fourth Edition*. IGI Global, 2018, pp. 6882–6893.

[18] J. C. Hu, X. Gu, S. R. Lipsitz, M. J. Barry, A. V. D'Amico, A. C. Weinberg, and N. L. Keating, "Comparative effectiveness of minimally invasive vs open radical prostatectomy," *The Journal of the American Medical Association*, vol. 302, no. 14, pp. 1557–1564, 2009.

[19] W. R. Peters and T. L. Bartels, "Minimally invasive colectomy: are the potential benefits realized?" *Diseases of the colon & rectum*, vol. 36, no. 8, pp. 751–756, 1993.

[20] R. Tinelli, P. Litta, Y. Meir, D. Surico, L. Leo, A. Fusco, S. Angioni, and E. Cicinelli, "Advantages of laparoscopy versus laparotomy in extremely obese women (bmi $>$ 35) with early-stage endometrial cancer: a multicenter study," *Anticancer research*, vol. 34, no. 5, pp. 2497–2502, 2014.

[21] J. H. Peters, G. Gibbons, J. Innes, K. Nichols, S. Roby, E. Ellison, *et al.*, "Complications of laparoscopic cholecystectomy." *Surgery*, vol. 110, no. 4, pp. 769–77, 1991.

[22] K. K. Yau, W. T. Siu, C. N. Tang, G. P. C. Yang, and M. K. W. Li, "Laparoscopic versus open appendectomy for complicated appendicitis," *Journal of the American College of Surgeons*, vol. 205, no. 1, pp. 60–65, 2007.

[23] B. Bagan, N. Patel, H. Deutsch, J. Harrop, A. Sharan, A. Vaccaro, and J. Ratliff, "Perioperative complications of minimally invasive surgery (MIS): comparison of MIS and open interbody fusion techniques." *Surgical Technology International*, vol. 17, pp. 281–286, 2008.

[24] C. Peng, W. Yue, S. Poh, W. Yeo, and S. Tan, "Clinical and radiological outcomes of minimally invasive versus open transforaminal lumbar interbody fusion." *Spine*, vol. 34, no. 13, p. 1385, 2009.

[25] S. Sauerland, T. Jaschinski, and E. A. Neugebauer, "Laparoscopic versus open surgery for suspected appendicitis," *Cochrane Database of Systematic Reviews*, vol. 10, pp. 1–140, 2010.

[26] H.-L. Wang, F. Lü, J.-Y. Jiang, X. Ma, X.-L. Xia, and L.-X. Wang, "Minimally invasive lumbar interbody fusion via mast quadrant retractor versus open surgery: a prospective randomized clinical trial." *Chinese Medical Journal*, vol. 124, no. 23, pp. 3868–3874, 2011.

[27] A. Park, G. Lee, F. J. Seagull, N. Meenaghan, and D. Dexter, "Patients benefit while surgeons suffer: an impending epidemic," *Journal of the American College of Surgeons*, vol. 210, no. 3, pp. 306–313, 2010.

[28] M. Van Det, W. Meijerink, C. Hoff, E. Totte, and J. Pierie, "Optimal ergonomics for laparoscopic surgery in minimally invasive surgery suites: a review and guidelines," *Surgical Endoscopy*, vol. 23, no. 6, pp. 1279–1285, 2009.

[29] M. Wentink, P. Breedveld, D. Meijer, and H. Stassen, "Endoscopic camera rotation: a conceptual solution to improve hand-eye coordination in minimally-invasive surgery," *Minimally Invasive Therapy & Allied Technologies*, vol. 9, no. 2, pp. 125–131, 2000.

[30] R. Berguer, W. Smith, and Y. Chung, "Performing laparoscopic surgery is significantly more stressful for the surgeon than open surgery," *Surgical endoscopy*, vol. 15, no. 10, pp. 1204–1207, 2001.

[31] V. Vitiello, S. Lee, T. P. Cundy, and G. Z. Yang, "Emerging robotic platforms for minimally invasive surgery," *Biomedical Engineering, IEEE Reviews in*, vol. 6, pp. 111–126, 2013.

[32] C. Basdogan, S. De, J. Kim, M. Muniyandi, H. Kim, and M. Srinivasan, "Haptics in minimally invasive surgical simulation and training," *Computer Graphics and Applications, IEEE*, vol. 24, no. 2, pp. 56–64, March 2004.

[33] J. Dankelman, "Surgical robots and other training tools in minimally invasive surgery," in *Systems, Man and Cybernetics, 2004 IEEE International Conference on*, vol. 3, Oct 2004, pp. 2459–2464.

[34] R. Berguer, W. Smith, and Y. Chung, "Performing laparoscopic surgery is significantly more stressful for the surgeon than open surgery," *Surgical endoscopy*, vol. 15, no. 10, pp. 1204–1207, 2001.

[35] K. J. Rebello, "Applications of mems in surgery," *Proceedings of the IEEE*, vol. 92, no. 1, pp. 43–55, 2004.

[36] G. Dakin and M. Gagner, "Comparison of laparoscopic skills performance between standard instruments and two surgical robotic systems," *Surgical Endoscopy And Other Interventional Techniques*, vol. 17, no. 4, pp. 574–579, 2003.

[37] R. Devengenzo, T. Solomon, and T. Cooper, "Cable tensioning in a robotic surgical system," June 9 2015, US Patent 9,050,119. [Online]. Available: http://www.google.com/patents/US9050119

[38] L. van den Bedem, "Realization of a demonstrator slave for robotic minimally invasive surgery," Ph.D. dissertation, Department of Mechanical Engineering, 2010.

[39] J. Li, G. Zhang, Y. Xing, H. Liu, and S. Wang, "A class of 2-degree-of-freedom planar remote center-of-motion mechanisms based on virtual parallelograms," *Journal of Mechanisms and Robotics*, vol. 6, no. 3, pp. 031 014(1–7), 2014.

[40] A. Gijbels, E. B. Vander Poorten, P. Stalmans, H. Van Brussel, and D. Reynaerts, "Design of a teleoperated robotic system for retinal surgery," in *IEEE International Conference on Robotics and Automation (ICRA)*. IEEE, 2014, pp. 2357–2363.

[41] S. Nisar, T. Endo, and F. Matsuno, "Design and kinematic optimization of a two degrees-of-freedom planar remote center of motion mechanism for minimally invasive surgery manipulators," *Journal of Mechanisms and Robotics*, vol. 9, no. 3, p. 031013, 2017.

[42] C.-H. Kuo and S.-J. Lai, "Design of a novel statically balanced mechanism for laparoscope holders with decoupled positioning and orientating manipulation," *Journal of Mechanisms and Robotics*, vol. 8, no. 1, p. 015001, 2016.

[43] K. Kong, J. Li, H. Zhang, J. Li, and S. Wang, "Kinematic design of a generalized double parallelogram based remote center-of-motion mechanism for minimally invasive surgical robot," *Journal of Medical Devices*, vol. 10, no. 4, p. 041006, 2016.

[44] S. Nisar and O. Hasan, "State of the art and key design challenges of telesurgical robotics," in *Encyclopedia of Information Science and Technology, Fourth Edition*. IGI Global, 2018, pp. 6872–6881.

[45] G. Hamlin and A. Sanderson, "A novel concentric multilink spherical joint with parallel robotics applications," in *Robotics and Automation, 1994. Proceedings., 1994 IEEE International Conference on*, May 1994, pp. 1267–1272 vol.2.

[46] R. Taylor, J. Funda, B. Eldridge, S. Gomory, K. Gruben, D. LaRose, M. Talamini, L. Kavoussi, and J. Anderson, "A telerobotic assistant for laparoscopic surgery," *Engineering in Medicine and Biology Magazine, IEEE*, vol. 14, no. 3, pp. 279–288, May 1995.

[47] R. Taylor, J. Funda, D. Grossman, J. Karidis, and D. LaRose, "Remote center-of-motion robot for surgery," Mar. 14 1995, US Patent 5,397,323. [Online]. Available: http://www.google.com/patents/US5397323

[48] J. Rosen, J. D. Brown, L. Chang, M. N. Sinanan, and B. Hannaford, "Generalized approach for modeling minimally invasive surgery as a stochastic process using a discrete markov model," *Biomedical Engineering, IEEE Transactions on*, vol. 53, no. 3, pp. 399–413, 2006.

[49] M. Lum, J. Rosen, M. Sinanan, and B. Hannaford, "Optimization of a spherical mechanism for a minimally invasive surgical robot: theoretical and experimental approaches," *Biomedical Engineering, IEEE Transactions on*, vol. 53, no. 7, pp. 1440–1445, July 2006.

[50] A. Gijbels, N. Wouters, P. Stalmans, H. Van Brussel, D. Reynaerts, and E. V. Poorten, "Design and realisation of a novel robotic manipulator for retinal surgery," in *Intelligent Robots and Systems (IROS), 2013 IEEE/RSJ International Conference on*. IEEE, 2013, pp. 3598–3603.

[51] G. Zong, X. Pei, J. Yu, and S. Bi, "Classification and type synthesis of 1-dof remote center of motion mechanisms," *Mechanism and Machine Theory*, vol. 43, no. 12, pp. 1585–1595, 2008.

[52] B. Hannaford, J. Rosen, D. W. Friedman, H. King, P. Roan, L. Cheng, D. Glozman, J. Ma, S. N. Kosari, and L. White, "Raven-ii: an open platform for surgical robotics

research," *Biomedical Engineering, IEEE Transactions on*, vol. 60, no. 4, pp. 954–959, 2013.

[53] G. T. Sung and I. S. Gill, "Robotic laparoscopic surgery: a comparison of the da vinci and zeus systems," *Urology*, vol. 58, no. 6, pp. 893–898, 2001.

[54] S. Aksungur, "Remote center of motion (rcm) mechanisms for surgical operations," *International Journal of Applied Mathematics, Electronics and Computers*, vol. 3, no. 2, pp. 119–126, 2015.

[55] J. Rosen, J. Brown, L. Chang, M. Barreca, M. Sinanan, and B. Hannaford, "The bluedragon - a system for measuring the kinematics and dynamics of minimally invasive surgical tools in-vivo," in *Robotics and Automation, 2002. Proceedings. ICRA '02. IEEE International Conference on*, vol. 2, 2002, pp. 1876–1881.

[56] I. Alkatout, L. Mettler, N. Maass, G.-K. Noé, and M. Elessawy, "Abdominal anatomy in the context of port placement and trocars," *Journal of the Turkish German Gynecological Association*, vol. 16, no. 4, p. 241, 2015.

[57] J. Joris, E. Thiry, P. Paris, J. Weerts, and M. Lamy, "Pain after laparoscopic cholecystectomy: characteristics and effect of intraperitoneal bupivacaine," *Anesthesia & Analgesia*, vol. 81, no. 2, pp. 379–384, 1995.

[58] C. Freschi, V. Ferrari, F. Melfi, M. Ferrari, F. Mosca, and A. Cuschieri, "Technical review of the da vinci surgical telemanipulator," *The International Journal of Medical Robotics and Computer Assisted Surgery*, vol. 9, no. 4, pp. 396–406, 2013.

[59] J. Denavit and R. S. Hartenberg, "A kinematic notation for lower-pair mechanisms based on matrices." *Trans. of the ASME. Journal of Applied Mechanics*, vol. 22, pp. 215–221, 1955. [Online]. Available: http://ci.nii.ac.jp/naid/10008019314/en/

[60] T. Yoshikawa, "Manipulability of robotic mechanisms," *The international journal of Robotics Research*, vol. 4, no. 2, pp. 3–9, 1985.

[61] A. Tobergte, R. Konietschke, and G. Hirzinger, "Planning and control of a teleoperation system for research in minimally invasive robotic surgery," in *Robotics and Automation, 2009. ICRA'09. IEEE International Conference on.* IEEE, 2009, pp. 4225–4232.

[62] W. Townsend and J. Salisbury, "The efficiency limit of belt and cable drives," *ASME Journal of Mechanisms, Transmissions, and Automation in Design*, vol. 110, no. 3, pp. 303–307, 1988.

[63] J. Li, G. Zhang, A. Müller, and S. Wang, "A family of remote center of motion mechanisms based on intersecting motion planes," *Journal of Mechanical Design*, vol. 135, no. 9, p. 091009, 2013.

[64] R. H. Taylor, A. Menciassi, G. Fichtinger, P. Fiorini, and P. Dario, "Medical robotics and computer-integrated surgery," in *Springer Handbook of Robotics.* Springer, 2016, pp. 1657–1684.

[65] H. Iseki, Y. Muragaki, R. Nakamura, N. Ozawa, H. Taniguchi, T. Hori, and K. Takakura, "Intelligent operating theater using intraoperative open-mri," *Magnetic Resonance in Medical Sciences*, vol. 4, no. 3, pp. 129–136, 2005.

[66] A. Casals, J. Amat, and E. Laporte, "Automatic guidance of an assistant robot in laparoscopic surgery," in *IEEE International Conference on Robotics and Automation (ICRA)*, vol. 1. IEEE, 1996, pp. 895–900.

[67] P. C. Giulianotti, A. Coratti, M. Angelini, F. Sbrana, S. Cecconi, T. Balestracci, and G. Caravaglios, "Robotics in general surgery: personal experience in a large community hospital," *Archives of Surgery*, vol. 138, no. 7, pp. 777–784, 2003.

[68] S. K. Saha, *Introduction to robotics*. Tata McGraw-Hill Education, 2014.

[69] H. Z. Tan, M. A. Srinivasan, B. Eberman, and B. Cheng, "Human factors for the design of force-reflecting haptic interfaces," *Dynamic Systems and Control*, vol. 55, no. 1, pp. 353–359, 1994.

[70] J. Perret and P. Vercruysse, "Advantages of mechanical backdrivability for medical applications of force control," in *Computer/Robot Assisted Surgery (CRAS), 2014 Conference on*, 2014, pp. 84–86.

[71] W. T. Townsend, "The effect of transmission design on force-controlled manipulator performance," Ph.D. dissertation, Massachusetts Institute of Technology, 1988.

[72] B. Hannaford and A. M. Okamura, "Haptics," in *Springer Handbook of Robotics*. Springer, 2016, pp. 1063–1084.

[73] B. Siciliano and O. Khatib, *Springer Handbook of Robotics*. Springer, 2016.

[74] C. Pacchierotti, S. Sinclair, M. Solazzi, A. Frisoli, V. Hayward, and D. Prattichizzo, "Wearable haptic systems for the fingertip and the hand: Taxonomy, review, and perspectives," *IEEE Transactions on Haptics*, vol. 10, no. 4, pp. 580–600, 2017.

[75] J. M. Suchoski, A. Barron, C. Wu, Z. F. Quek, S. Keller, and A. M. Okamura, "Comparison of kinesthetic and skin deformation feedback for mass rendering," in *IEEE International Conference on Robotics and Automation*, 2016, pp. 4030–4035.

[76] A. M. Okamura, "Haptic feedback in robot-assisted minimally invasive surgery," *Current Opinion in Urology*, vol. 19, no. 1, p. 102, 2009.

[77] G. C. Burdea, "Keynote address: haptics feedback for virtual reality," in *Proceedings of International Workshop on Virtual Prototyping*, 1999, pp. 87–96.

[78] S. Jadhav, V. Kannanda, B. Kang, M. T. Tolley, and J. P. Schulze, "Soft robotic glove for kinesthetic haptic feedback in virtual reality environments," *Electronic Imaging*, vol. 2017, no. 3, pp. 19–24, 2017.

[79] M. Fontana, A. Dettori, F. Salsedo, and M. Bergamasco, "Mechanical design of a novel hand exoskeleton for accurate force displaying," in *IEEE International Conference on Robotics and Automation*, 2009, pp. 1704–1709.

[80] S. L. Springer and N. J. Ferrier, "Design and control of a force-reflecting haptic interface for teleoperational grasping," *Journal of Mechanical Design*, vol. 124, no. 2, pp. 277–283, 2002.

[81] D. Leonardis, M. Barsotti, C. Loconsole, M. Solazzi, M. Troncossi, C. Mazzotti, V. P. Castelli, C. Procopio, G. Lamola, C. Chisari, *et al.*, "An emg-controlled robotic hand exoskeleton for bilateral rehabilitation," *IEEE Transactions on Haptics*, vol. 8, no. 2, pp. 140–151, 2015.

[82] C. J. Nycz, T. Bützer, O. Lambercy, J. Arata, G. S. Fischer, and R. Gassert, "Design and characterization of a lightweight and fully portable remote actuation system for use with a hand exoskeleton," *IEEE Robotics and Automation Letters*, vol. 1, no. 2, pp. 976–983, 2016.

[83] B. Allotta, R. Conti, L. Governi, E. Meli, A. Ridolfi, and Y. Volpe, "Development and experimental testing of a portable hand exoskeleton," in *IEEE/RSJ International Conference on Intelligent Robots and Systems*, 2015, pp. 5339–5344.

[84] Z. MA and P. Ben-Tzvi, "RML Glove—An exoskeleton glove mechanism with haptics feedback," *IEEE/ASME Transactions on Mechatronics*, vol. 20, no. 2, pp. 641–652, 2015.

[85] H. Kim, M. Kim, and W. Lee, "Hapthimble: A wearable haptic device towards usable virtual touch screen," in *Proc. CHI Conference on Human Factors in Computing Systems*. ACM, 2016, pp. 3694–3705.

[86] Y. Fu, Q. Zhang, F. Zhang, and Z. Gan, "Design and development of a hand rehabilitation robot for patient-cooperative therapy following stroke," in *IEEE International Conference on Mechatronics and Automation*, 2011, pp. 112–117.

[87] O. Lambercy, D. Schröder, S. Zwicker, and R. Gassert, "Design of a thumb exoskeleton for hand rehabilitation," in *Proc. 7th International Convention on Rehabilitation Engineering and Assistive Technology*, ser. i-CREATe '13. Kaki Bukit TechPark II,, Singapore: Singapore Therapeutic, Assistive & Rehabilitative Technologies (START) Centre, 2013, pp. 41:1–41:4. [Online]. Available: http://dl.acm.org/citation.cfm?id=2567429.2567477

[88] P. Stergiopoulos, P. Fuchs, and C. Laurgeau, "Design of a 2-finger hand skeleton for VR grasping simulation," in *Eurohaptics*, 2003, pp. 80–93.

[89] M. J. Lelieveld, T. Maeno, and T. Tomiyama, "Design and development of two concepts for a 4 DOF portable haptic interface with active and passive multi-point force feedback for the index finger," in *Proc. International Design Engineering Technical Conferences and Computers and Information in Engineering Conference*. ASME, 2006, pp. 547–556.

[90] M. Cempini, M. Cortese, and N. Vitiello, "A powered finger–thumb wearable hand exoskeleton with self-aligning joint axes," *IEEE/ASME Transactions on Mechatronics*, vol. 20, no. 2, pp. 705–716, 2015.

[91] P. Agarwal, J. Fox, Y. Yun, M. K. O'Malley, and A. D. Deshpande, "An index finger exoskeleton with series elastic actuation for rehabilitation: Design, control and performance characterization," *The International Journal of Robotics Research*, vol. 34, no. 14, pp. 1747–1772, 2015.

[92] M. Aiple and A. Schiele, "Pushing the limits of the CyberGrasp™ for haptic rendering," in *IEEE International Conference on Robotics and Automation*, 2013, pp. 3541–3546.

[93] Y. Tanaka, H. Yamauchi, and K. Amemiya, "Wearable haptic display for immersive virtual environment," in *Proc. International Symposium on Fluid Power*, no. 5-2. The Japan Fluid Power System Society, 2002, pp. 309–314.

[94] P. Polygerinos, Z. Wang, K. C. Galloway, R. J. Wood, and C. J. Walsh, "Soft robotic glove for combined assistance and at-home rehabilitation," *Robotics and Autonomous Systems*, vol. 73, pp. 135–143, 2015.

[95] G. Stetten, B. Wu, R. Klatzky, J. Galeotti, M. Siegel, R. Lee, F. Mah, A. Eller, J. Schuman, and R. Hollis, "Hand-held force magnifier for surgical instruments," *Information Processing in Computer-Assisted Interventions*, pp. 90–100, 2011.

[96] M. Bouzit, G. Burdea, G. Popescu, and R. Boian, "The Rutgers Master II-new design force-feedback glove," *IEEE/ASME Transactions on Mechatronics*, vol. 7, no. 2, pp. 256–263, 2002.

[97] I. Choi, E. Ofek, H. Benko, M. Sinclair, and C. Holz, "Claw: A multifunctional handheld haptic controller for grasping, touching, and triggering in virtual reality," in *Proc. CHI Conference on Human Factors in Computing Systems*, 2018, pp. 654:1–654:13.

[98] I. Choi, E. W. Hawkes, D. L. Christensen, C. J. Ploch, and S. Follmer, "Wolverine: A wearable haptic interface for grasping in virtual reality," in *IEEE/RSJ International Conference on Intelligent Robots and Systems*, 2016, pp. 986–993.

[99] R. M. Pierce, E. A. Fedalei, and K. J. Kuchenbecker, "A wearable device for controlling a robot gripper with fingertip contact, pressure, vibrotactile, and grip force feedback," in *IEEE Haptics Symposium*, 2014, pp. 19–25.

[100] G. Gescheider, *Psychophysics: method, theory, and application*, 2nd ed. L. Erlbaum Associates, 1985.

[101] D. M. F. Conti, F. Barbagli and C. Sewell, "CHAI 3D - an open-source library for the rapid development of haptic scenes," in *IEEE World Haptics*, 2005, pp. 21–29.

[102] C. B. Zilles and J. K. Salisbury, "A constraint-based god-object method for haptic display," in *IEEE/RSJ International Conference on Intelligent Robots and Systems*, vol. 3, 1995, pp. 146–151 vol.3.

List of Publications

Publications Related to the Dissertation

[1] S. Nisar, M. O. Martinez, T. Endo, F. Matsuno and A. M. Okamura "Effects of Different Hand-Grounding Locations on Haptic Performance with a Wearable Kinesthetic Haptic Device", *IEEE Robotics and Automation Letters (RA-L)*, Vol. 4(2), pp. 351-358, (2019). https://doi.org/10.1109/LRA.2018.2890198

[2] S. Nisar, M. O. Martinez,, T. Endo, F. Matsuno and A. M. Okamura "Effects of Different Hand-Grounding Locations on User Performance with a Wearable Kinesthetic Haptic Device", *IEEE International Conference on Robotics and Automation (ICRA'19)*, (2019). (accepted)

[3] S. Nisar, A. Hameed, N. Kamal, O. Hasan and F. Matsuno, "Design and Realization of a Planar Robotic Manipulator for Minimally Invasive Surgery with Replaceable Surgical Tool", *IEEE/ASME Transactions on Mechatronics*, (2018). (1st revision completed)

[4] S. Nisar, T. Endo, F. Matsuno, "Design and Optimization of a 2-Degree-of-Freedom Planar Remote Center of Motion Mechanism for Surgical Manipulators with Smaller Footprint", *Journal of Mechanism and Machine Theory*, (2018). https://doi.org/10.1016/j.mechmachtheory.2018.07.020

[5] S. Nisar, T. Endo, A. M. Okamura and F. Matsuno, "Design of Novel 2-Degree-of-Freedom Planar Remote Center of Motion Mechanism for Surgical Manipulators with Smaller Footprint", *the 62nd Annual Conference of the Institute of Systems, Control and Information Engineers (SCI'18)*, Kyoto, (2018). (**Best Presentation Award**)

[6] S. Nisar, T. Endo, F. Matsuno and A. M. Okamura, "Design of a Wearable Kinesthetic Device to Study the Effects of Different Hand-Grounding Locations on User Performance", *IEEE Haptic Symposium 2018*, San Francisco, (2018). [WIP]

[7] S. Nisar, T. Endo, F. Matsuno, "Design and Kinematic Optimization of a 2 Degrees-of-Freedom Planar Remote Center of Motion Mechanism for Minimally Invasive Surgery Manipulators", *Journal of Mechanism and Robotics, Transactions of ASME,* 9(3), pp. 031013 1-9, (2017).

[8] T. Hassan, A. Hameed, S. Nisar, N. Kamal and O. Hasan, "Al-Zahrawi: A Telesurgical Robotic System for Minimal Invasive Surgery," in IEEE Systems Journal, vol. 10, no. 3, pp. 1035-1045, (2016). doi: 10.1109/JSYST.2014.2331146

[9] S. Nisar, T. Endo, F. Matsuno, "A Backdrivable 2 Degrees-of-Freedom Planar Remote Center of Motion Mechanism for Minimally Invasive Surgery Manipulators", *In Proceedings of the 6th Joint Workshop on New Technologies for Computer/Robot Assisted Surgery (CRAS),* Pisa, (2016).